Design and Fabrication of a Thin Film Micromachined Accelerometer

by

Mitchell J. Novack

Submitted to the Department of Mechanical Engineering
in partial fulfillment of the requirements for the degree of

Master of Science in Mechanical Engineering

at the

MASSACHUSETTS INSTITUTE OF TECHNOLOGY

September 1992

Author .....
Department of Mechanical Engineering
September 1, 1992

Certified by .....
Martin A. Schmidt
Associate Professor, Electrical Engineering and Computer Science
Thesis Supervisor

Read by .....
Patrick Leehy
Professor, Mechanical Engineering and Ocean Engineering
Thesis Reader

Accepted by .....
Ain Sonin
Chairman, Departmental Committee on Graduate Students

Design and Fabrication of a Thin Film Micromachined Accelerometer

by

Mitchell J. Novack

Submitted to the Department of Mechanical Engineering
on September 1, 1992, in partial fulfillment of the
requirements for the degree of
Master of Science in Mechanical Engineering

Abstract

This thesis reports on the mechanical design of a micromachined acceleration sensor (accelerometer), and on the prototype fabrication and testing of the sensor. The intended applications include crash detection in automobiles for airbag deployment, and sensing of automobile chassis motion to allow active control of the suspension system. Fabrication of these sensors by micromachining has the advantage of very low manufacturing cost, which is a requirement for the automotive market.

The accelerometer design consists of an inertial proof mass suspended by four tethers. The tethers support the proof mass, but allow it to translate along the sensitive axis of the accelerometer. Thus, for acceleration inputs along the sensitive axis, the proof mass displaces some measurable distance. The input acceleration is directly proportional to this displacement, which we measure by the change in capacitance between the proof mass and a stationary electrode plate.

The micromachining process uses plasma etching to form the proof mass and the tethers in a thin membrane of silicon, supported by oxide, on a standard silicon wafer ('handle wafer'). The thin membrane having been formed by high temperature wafer bonding and etch back to a boron etch stop. This process could be adapted to allow for integration of electronics on the same wafer with the accelerometer.

A mechanical design is shown that solves a number of the problems associated with thin film processing. One of these is the excessive gas damping caused by the small air gap between the proof mass and the handle wafer. This is solved by adding perforations to the proof mass, and we show that this is so effective that even a critically damped dynamic response can be achieved. Sensitivity to mounting stresses and temperature effects is another mechanical issue studied. The design shown here reduces this sensitivity by a factor of 1000 compared to that of more conventional designs. Yet another issue is the nonlinearity of the sensor's response, and we show how this can be reduced to practically zero.

The fabrication sequence for the prototype accelerometers is discussed in detail, and photographs of completed devices are shown. By applying a DC voltage between the proof mass and the handle wafer of completed sensors, we were able to use elec-

trostatic force to simulate input accelerations. The electrostatic force pulls the proof mass towards the handle wafer, and we measure the change in capacitance between the proof mass and the handle wafer. This data shows that the proof mass is free to move and that we can measure this change in position of the proof mass.

We also mounted the sensors on an electrodynamic shaker and tested them with input vibrations up to 40 g's at 43 Hz. The test data shows that the accelerometers track the frequency of the input vibration, and the output increases with increasing input acceleration.

Thesis Supervisor: Martin A. Schmidt
Title: Associate Professor, Electrical Engineering and Computer Science

Acknowledgments

I wish to thank Professor Martin Schmidt and the members of his research group, for making my time at MIT both a fulfilling learning experience, and a happy memory. I appreciate the expertise of Dr. Schmidt, Vince McNeil, and Michael Huff in the field of micromachining, and I thank them for patiently sharing their knowledge with me. I enjoyed our group's enthusiasm over technology, creative ideas, computers, number crunching, and all the things that make engineering fun. For that part of it, I thank the entire group, namely, Errol Arkilic, Chris Bang, Ted Bloomstein, Charles Hsu, John Gilbert, Michael Huff, Vince McNeil, Lalitha Parameswaran, Javad Shajii, and Pat Varley.

The Microsystems Technology Laboratory is an impressive collection of processing equipment, test equipment, and computer facilities; all being used by hundreds of students with many different needs. I want to thank the conscientious staff of engineers and technicians who keep the lab running for the benefit of the students. I appreciate the training and the advice that I received from them. Also, I thank the MEMCAD group for maintenance of the mechanical simulation software and computers that were so useful in my research.

This research was funded by Delco Electronics. I thank them for their support and for their assistance in providing boron-doped wafers to me, and for their advice on wafer bonding.

My employer, Sundstrand Data Control, deserves special thanks. They have provided financial support, and kept my job open, while I have pursued this graduate degree. In particular, I thank Brian Norling for making that happen. He has always been a source of encouragement and inspiration for my professional development.

I thank my parents for their continued support and encouragement throughout this time. Also, my mother-in-law was an enormous help to my family in easing the arrival of our newborn baby.

I could never give enough thanks to my wife, Lauren, for the support she has given me. Leaving her own job, leaving her own family and friends, taking care of

two babies at home while I was at school; all of these sacrifices she made without any hesitation. Whenever I worked late or on weekends, she relieved my guilt and anxiety with her standard response of 'do whatever you need to graduate'. I admire the strength and patience she has shown throughout this experience.

Contents

List of Figures

List of Tables

Chapter 1

Introduction

1.1 Motivation - accelerometer markets

A completely new, and potentially enormous market for accelerometers is just now developing. It requires something much different from accelerometers previously produced. The market is for automotive accelerometers, where the demand for high volume and low cost cannot be met by any existing products. These new sensors will be made in the same manner as integrated circuits, that is hundreds (or thousands) at a time on batch fabricated silicon wafers. As these cheap sensors are being rapidly developed for automobiles, we are also looking closely at accelerometers for traditional applications and deciding whether those could be made less expensive, and maybe more accurate, by the application of silicon technology. And finally, we anticipate the opening of new markets, as solid state accelerometers become available and familiar to equipment manufacturers.

The first use of accelerometers in cars will be for the detection of a collision, with subsequent activation of the airbags. The accuracy requirement for this application is about 5%, at a price of under $10 [1]. Existing accelerometers cannot achieve this price goal, and their performance far exceeds what is required for automobiles. We can classify these existing accelerometers into three grades: instrument grade , inertial grade, and strategic grade. A rough comparison of price and performance illustrates the unique requirements of the automobile industry:

	accuracy	price
automotive grade	5%	$10
instrument grade	1%	$500
inertial grade	.05%	$1000
strategic grade	.001%	$100,000

The new development path for accelerometers is clear; it has already been blazed by pressure sensors during the last decade. Low cost pressure sensors are used in virtually every new car to monitor manifold absolute pressure (MAP). About 20 million of these MAP sensors are produced annually, at $10 each (excluding packaging and electronics). The key to success of this product is silicon micromachining. By making the devices extremely small, we fabricate hundreds at a time on a batch fabricated wafer. We use silicon because the facilities and technologies are already available from the integrated circuits industry. Large manufacturers of semiconductor devices (eg. Motorola, Honeywell) are the leaders in high volume, low cost production, and as such, these are the manufacturers we look to for mass production of sensors.

It is interesting that the next automotive use for accelerometers will demand better accuracy than those used for crash control. These accelerometers will monitor chassis motion, and provide feedback into the suspension system controls to help make for a smoother ride. These accelerometers will require 3% accuracy. Still another use is for automobile navigation systems. The accuracy for these sensors would have to be close to that of existing inertial grade accelerometers used for aircraft navigation and missile guidance. Therefore, the automotive industry is going to push for higher accuracy, beyond the 5% required for airbag deployment. It is safe to assume that the price will still stay low even for these higher accuracy sensors; they have to be inexpensive to compete in the automobile industry. So, how will this effect the traditional, higher performance, accelerometer markets?

The effect should be one of considerable cost savings for users of accelerometers outside of the automotive industry. If a high performance accelerometer design can be fabricated by silicon micromachining, then ideally we could do the fabrication

on a high volume wafer processing line much cheaper than by traditional machining methods. The literature indicates that a number of organizations are developing high-performance microaccelerometers [18, 19, 25, 29] . If this works, then the price of all accelerometers will come down. The *if* is important, because we are assuming that high performance designs can be fabricated on high volume wafer processing lines that would be designed primarily for low accuracy sensors. Also, we have totally ignored the importance of packaging on the performance and on the final price.

The other effect of the the mass produced, solid state accelerometers, will be the opening of new markets. Both the low cost and the small size of micromachined sensors create new applications. We saw this happen with pressure sensors, where the biomedical industry used the automotive MAP to make disposable blood pressure monitors, which quickly became a $100 million product. But the primary motivation at this time, is the automotive market. This is the most immediate, and the largest potential user of solid state accelerometers.

1.2 Research and Development in Micromachined Accelerometers

Roylance and Angell [2], in 1979, reported the first silicon micromachined accelerometer. This sensor was unique in that the proof mass, supporting tethers, and surrounding frame, were etched as an integral sensor in silicon. Their detection method was by diffused piezoresistors.

We get a feel for the current status of research and development in this field by reviewing the recently published literature. Figure 1-1 summarizes *some* of these publications from the last four years. This review is not exhaustive, but it does represent the technologies and design variations that are being pursued, and also some of the names of organizations that are doing the work.

Some observations regarding the data in Figure 1-1:

Research Organizations. In addition to the sheer number, we also notice the diversity among organizations pursuing this research. This list includes integrated circuit

Research Organization	Literature Reference	Detection Method	Electronics Design	Mechanism Design	Fabrication Technology
Analog Devices	1992 Symposium on VLSI Circuits [4]	Differential capacitive	Integrated BiMOS, electrostatic closed loop, self test.	Translating mass, four-tether support, in-plane sensing.	Polysilicon, 1 layer, 2um, integrated BiMOS
Motorola	1992 Hilton Head [5]	Differential capacitive	External, switched capacitor, open loop.	Pendulous mass, two-tether support coplanar with mass, out-of -plane sense.	Polysilicon, 3 layers.
Lucas NovaSensor	1988, 1992 Hilton Head [6,7]	Piezoresistive	Internal bridge, thermal self-test.	Pendulous mass, 2-tether support/sense, self-test tether, over-range protection	Bulk-etched mass, wafer-bonded & thinned tethers.
IC Sensors	1990 Hilton Head [8] 1989 MEMS [9] 1989 Transducers [10] 1988 Hilton Head [11]	Piezoresistive	Internal bridge, partial electrostatic self-test.	Translating mass, 4-tether support/sense, out-of-plane sense.	Bulk-etched mass.
Endevco Corp.	1991 Transducers [12] Oct. 1991 Sensors [13]	Piezoresistive	Internal bridge.	Pendulous mass, one-tether support plus two-tether sense, in-plane sensing.	Bulk-etched mass, <110> silicon, si/si/si stack bonded with solder glass.
Hitachi	1991,1989 Transducers [14,15] 1991 Sensor Symp[16]	Differential capacitive	ASIC, switched capacitor, pulse width modulated closed loop.	Pendulous mass, off-center tether, out-of-plane sense.	Bulk-etched mass, anodic bond of glass/si/glass stack.
Silicon Designs	1991 Transducers [17]	Differential capacitive	ASIC or integrated CMOS, switched capacitor.	Dual pendulous mass, torsional tether support.	Electroformed metal mass, CMOS compatibility
Centre Suisse d' Electronique et de Microtechnique	1989 Transducers [18]	Differential capacitive	ASIC, switched capacitor.	Pendulous mass, two-tether support coplanar with mass, out-of -plane sense.	Two-sided bulk etch of mass, electro-chemical tether etch.
Triton technologies and IC Sensors	1990 Hilton Head [19]	Electrostatic field sensing.	External, sigma-delta mod. closed loop.	Translating mass, 4 tethers on top & 4 on bottom.	Bulk-etched & wafer-bonded mass, composite tethers, 27 photo steps.
ESAT-MICAS Div.	1991 Transducers [20]	Differential capacitive	ASIC, switched capacitor. Unique contacts.	Translating mass, 4 tethers on top & 4 on bottom.	Bulk-etched & wafer-bonded mass, e-chem stop on epi.
Messerchmitt-Bolkow-Blohm	1989 Transducers [21]	Differential capacitive	ASIC, switched capacitor.	Translating mass, 4 tethers on top & 4 on bottom.	Bulk-etched from both sides, etch-stop on tethers.
Draper Laboratories	Transducers 1991 [22]	Resonant beam, 2 double-ended tuning forks.	Two hybrid circuit oscillators.	Translating mass, in-plane sensing.	Etched (by Statek) in piezoelectric quartz.
Draper Laboratories	1989 Transducers [23]	Differential capacitive	External, electrostatic closed loop.	Dual pendulous mass, torsional tether support, out-of-plane sensing.	Surface machined, boron-doped tethers & mass, sacrificial epi, metal-gate FET comp.
NEC	1989 Transducers [24]	Piezoresistive	Internal bridge	Translating mass, four-tether supports, attached to central post.	Bulk-etched mass, 4-electrode E-chem. etch stop on tethers, <110> Si
STC Technology,LTD	1989 Sensors & Actuators [25]	Resonant beam, piezoresistive drive and sense.	External	Pendulous mass, tethers on one side, resonator on other, out-of-plane sense.	Bulk-etched mass.
General Motors Research, and UC Berkeley	1989 Transducers [26]	Resonant beams	External	Translating mass, tethers on one side, resonators on other, 2 in-plane sense axes.	Bulk-etched mass, boron-doped poly tethers and resonators.
UC Berkeley	1992 Hilton Head [27]	Capacitive	Integrated CMOS, sigma-delta modulated electrostatic closed loop.	Translating mass, four-tether support, folded tether design.	Polysilicon, 2 layers, structures formed after CMOS.
Tohoku University	1991 Sensor Symp. [28]	Differential capacitive	External capacitance meter.	Translating mass, 4 tethers on top & 4 on bottom.	Bulk-etched mass, CVD silicon-oxynitride tethers.

Figure 1-1: A summary of some recently published research on micromachined accelerometers.

manufacturers (Motorola), automakers (General Motors), traditional accelerometer manufacturers (Endevco), and very small startup companies (Silicon Designs).

Detection Method. Differential capacitive sensing, using parallel plate capacitors, seems to be the predominant detection method. There are a number of good reasons for this. First, it does not suffer from extreme temperature sensitivity as does piezoresistive detection, which is typically -.2% change in sensitivity per $^{\circ}C$ change in temperature. Second, it is easy to include electrostatic self test and closed-loop rebalance. The self test capability is particularly important for the automotive market, where safety is a primary issue.

A disadvantage of capacitive sensing is the requirement for more complex electronics, and the need to control stray capacitances. Piezoresistive detection, on the other hand, is very simple. Usually, the sensor is designed as a four leg Wheatstone bridge, and the user provides power, and voltage readout, either with or without additional amplification.

Electronics Design. Four of the listed designs are attempting to integrate electronics and accelerometer on the same chip (Analog Devices, UC Berkeley, Silicon Designs, and Draper Laboratories). This has a potential cost advantage, in that integration reduces the total number of components, eliminates interconnects between sensor and electronics, and simplifies the final package. Reliability should be much better also, since wirebonds are eliminated between sensor and electronics. The cost and reliability advantages will be very important for the automotive market.

Mechanism Design. Of the ten translating mass designs listed, only one, the UC Berkeley design, uses the pinwheel tether configuration that we discuss in this thesis. Linearity, temperature sensitivity, and stability, can all be improved by the pinwheel tether support, without any change to the fabrication process.

Two designs are using a dual pendulous design with torsional support. The advantage of this configuration is that it achieves differential capacitive detection with a surface machining process.

Fabrication Technology. Five of the designs are surface machined, and include the four with integrated electronics. The more common surface machining method

is to form the proof mass and tethers in polysilicon over a sacrificial oxide layer. However, Draper Laboratory is using a heavily doped boron layer for the structures, over an epitaxial sacrificial layer. Still another, Silicon Designs, is using nickel with an undisclosed sacrificial layer.

The bulk etched designs all use anisotropic etching through the bulk of the wafer, and either boron doped etch stops or electrochemical etch stops, to form the thin tether support structures. Wafer bonding is used by NovaSensor to achieve integral overrange protection, and wafer bonding is used in the Triton and ESAT designs to get 4-tether support on both sides of the proof mass.

Only 4 of the 18 listed, are in production, and can be bought as standard products. The remaining are in various stages of development.

1.3 Thesis Overview

This thesis studies mechanical design issues relevant to the performance all thin film microaccelerometers. By thin film, we mean that the accelerometer is formed in a relatively thin layer, say less than 10 um, on one side only of a silicon wafer. The significant point being that integrated circuit technology consists entirely of thin film processes, so that integration of sensors and circuits can only be accomplished if the sensors also rely only on thin film processes.

Throughout this research, we have had a specific design concept and associated fabrication process in mind. We have applied our theoretical research to the development and fabrication of this design, shown in Figure 1-2 along with the fabrication sequence. The proof mass and the four tethers are plasma etched in a 5 um thick silicon layer. The plasma etch leaves the proof mass suspended over the handle wafer by the tethers, with a 1 to 2 um gap between the two. The accelerometer's sensitive axis is perpendicular to the wafer surface. We use the proof mass and the handle wafer as electrodes for capacitive detection of the proof mass motion.

The 5 um membrane is formed by wafer bonding and etch back to a boron etch stop. In this thesis, we fabricate the devices directly in the heavily doped boron etch

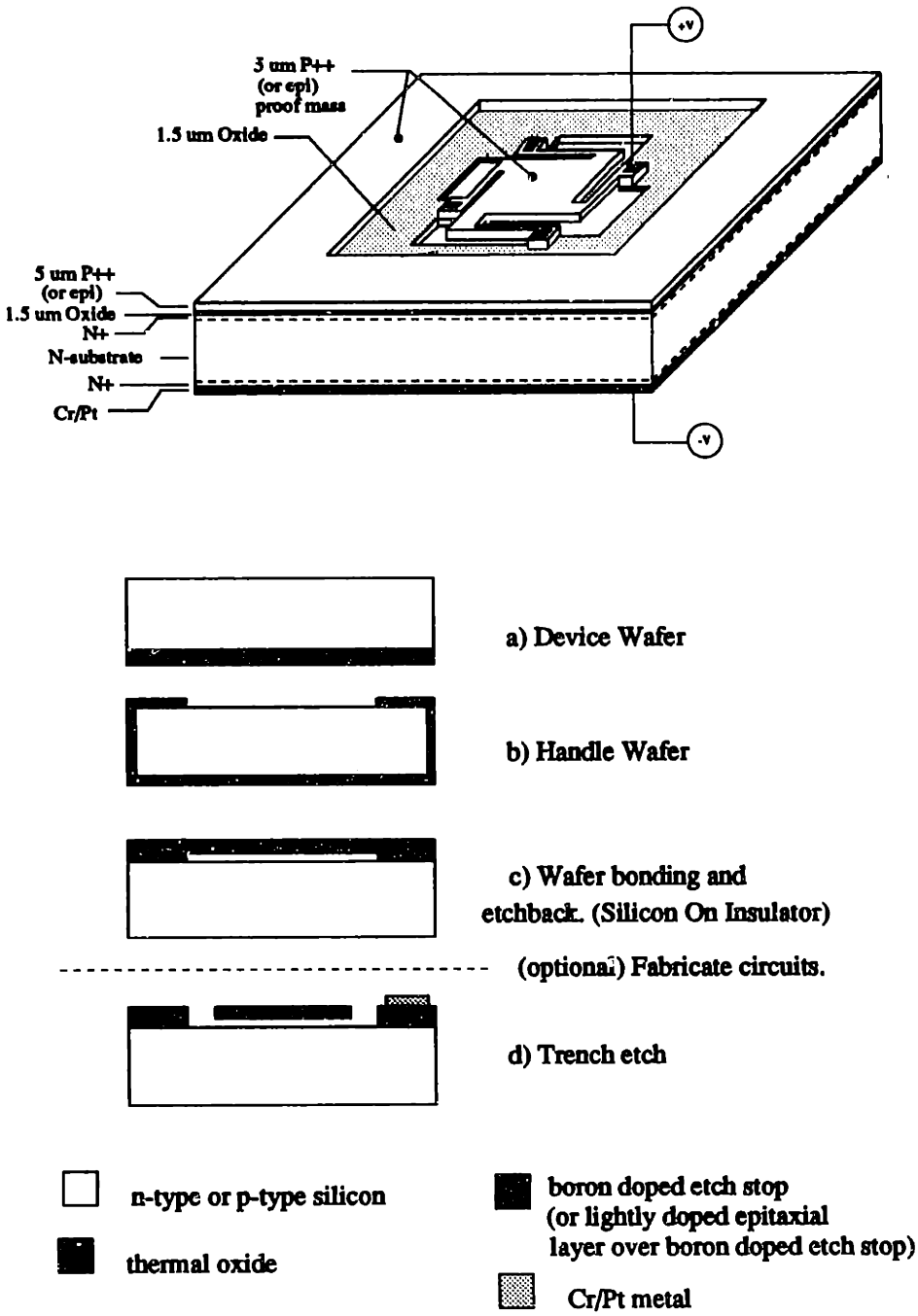

Figure 1-2: Concept for prototype accelerometers (top), and method of fabrication (bottom)

stop, but we could have used an epitaxial layer instead, which is more desirable for integrated circuits. After forming the 5 um membrane, the wafer could be introduced into a standard IC processing line to add integrated circuits, after which we would do the final trench etch to form the accelerometers. In the concluding chapter, we present a design where we have made the accelerometer as small as possible to take advantage of integrated circuitry.

With this overall picture in mind, we will now review this thesis in more detail. In Chapter 2 we address the design of the tether supports and the proof mass. Whether the sensor is to be operated in open-loop or closed-loop mode, affects the design of the tethers. For open-loop designs, which is what we are interested in, the tether stiffness (spring constant) along the sensitive direction determines the sensitivity and the dynamic bandwidth of the sensor. This leads to a key design constraint. That is, the useful dynamic bandwidth of the sensor is inversely proportional to the square root of the sensitivity (Equation 2.8).

If we wanted to use this sensor in closed-loop operation, then we would take a different approach to the tether design. The dynamic bandwidth constraint no longer applies to the tethers, because now the closed-loop electronics support the proof mass. Therefore, we are free to make the tethers as compliant as possible in the sensitive direction. The bottom line is better isolation of the sensor from external instabilities, such as packaging stresses and thermal stresses. This is in addition to the improved linearity that we get with closed-loop operation.

Section 2.4 presents the three sensor configurations that we considered in this research (Figure 2-2). We found that the second two designs, where the tethers are oriented in a pinwheel fashion around the proof mass ('pinwheel design'), offer enormous advantages over the design in which the tethers are all parallel to one other ('straight design'). The pinwheel designs typically offer 1000 time better attenuation of packaging stresses and thermally induced stresses compared to the straight design (Section 2.7). The advantage with respect to linearity is even greater. We show a pinwheel design that has only .005% full scale nonlinearity. This is compared to 20% full scale nonlinearity for the straight tether design (Section 2.6). In addition to these

performance advantages, the pinwheel designs are also more compact, and therefore cheaper to produce (more sensors per wafer) than the straight tether designs.

Squeeze film damping is addressed in Chapter 3. Excess damping can be a serious problem with thin film accelerometers, because the thin film proof mass has a very large surface area relative to its thickness, and the gap between the proof mass and the handle wafer is small. As a result, the dynamic bandwidth of a typical design is reduced from 2000 Hz to less than 1 Hz (Figure 3-2). We were able to solve the problem and achieve a critically damped dynamic response, by perforating the proof mass. The design of such a perforated mass is difficult, because closed form equations for the damping force on a perforated plate do not exist. We used finite element analysis to solve the problem, and Section 3.4 describes an especially efficient way to use the finite element analysis to arrive at a critically damped design. Figure 3-8 shows our perforated proof mass modified for maximum bandwidth. We realize in looking at this modification, that due to the extent of perforations on the plate, the proof mass has grown to a fairly large dimension, 800x800 um. This is driven by the need to maintain a minimum value on the sense capacitance, 1.5 pF in this case, so that the output capacitance is large relative to stray capacitances. This minimum capacitance requirement would be reduced, thereby reducing the size of the proof mass, if the electronics were integrated on the same chip with the sensor so that stray capacitances are reduced. A reasonable minimum capacitance, when using integrated electronics, is about 0.2 pF. Using this value, we calculate the the total sensor dimension would be only 200 um x 200 um.

In Chapter 4 Prototype Fabrication, we verify the feasibility of both the design and the fabrication process. We describe a process sequence in detail, and show SEM photographs of the completed structures (Section 4.4). Finally, in Chapter 5 we describe various tests for measuring accelerometer performance. The first tests measure static capacitance output and capacitance versus bias voltage, C-V. The C-V test simulates applied accelerations because the electrostatic force of the bias voltage actually pulls the proof mass in toward the handle wafer. Our C-V measurements on completed devices show that they are sensitive to bias voltage,

and it is clear that the proof mass pulls in to the handle wafer. For dynamic testing, we have constructed a system with a 100 lb_f shaker and Bruel & Kjaer reference accelerometer. The accelerometers have shown magnitude and frequency sensitivity on this test stand.

Chapter 2

Mechanical Design

2.1 Overview

All acceleration sensors have the basic mechanical components shown schematically in Figure 2-1. The proof mass is constrained by springs, but when the sensor is accelerated, the proof mass displaces by some finite amount and this displacement is transduced to an electrical output that is our measure of the acceleration.

The specific accelerometers that we have studied are shown in Figure 2-2. In all three designs, the proof mass is a square plate, and the springs are the four tethers supporting the proof mass. The proof mass is suspended over the bottom wafer, and moves relative to the bottom wafer when accelerated. This produces a change in capacitance between the proof mass (one electrode) and the bottom wafer (the other electrode) that is a measure of the applied acceleration.

The three tether configurations have different mechanical behavior that affect the sensor performance. We discuss these differences in Section 2.4. Then, in Section 2.5, we present the detailed design equations and the finite element analysis for each of the three designs.

Two important performance parameters, linearity and strain attenuation, are studied in Sections 2.6 and 2.7.

Our design analysis assumes that the sensors will be operated in open-loop mode. We do not use electrostatic force to restore the position of the proof mass under

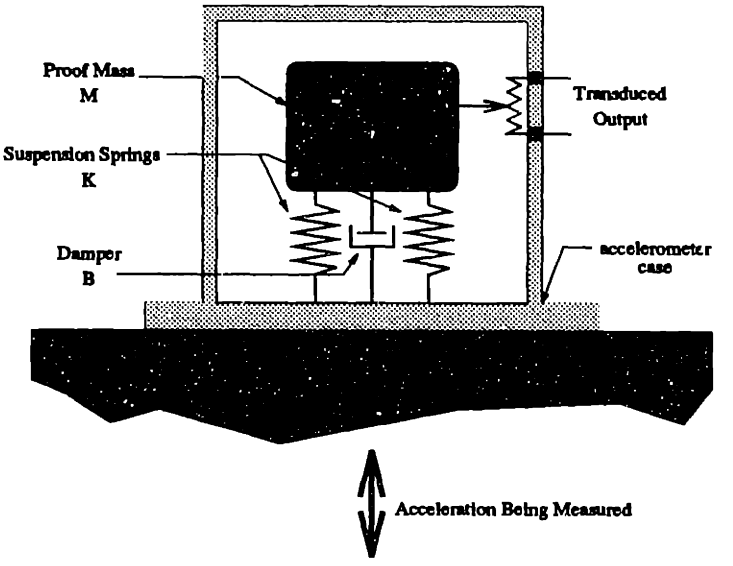

Figure 2-1: Generic accelerometer.

applied accelerations. This decision affects the tether design, as we discuss in Section 2.2, and it leads to the fundamental tradeoff between sensitivity and dynamic range given in Secion 2.3.

Appendix A should be referenced for a discussion of the appropriate elastic constants to use for silicon.

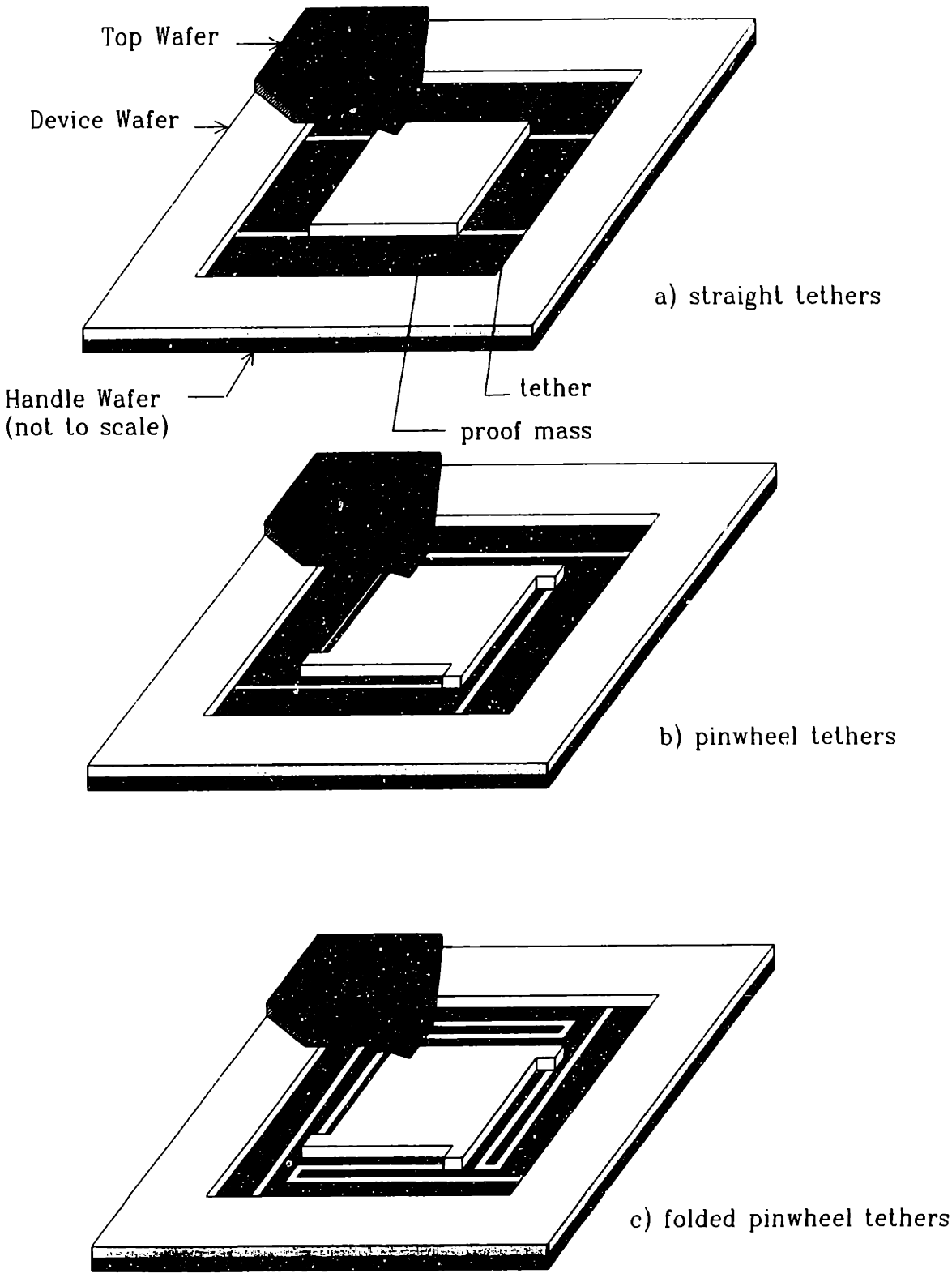

Figure 2-2: Three accelerometer designs studied.

2.2 Open-Loop, Closed-Loop Accelerometers

This distinction between accelerometer designs is important in its effect on the mechanical design of the sensor. Both closed-loop and open-loop designs are represented schematically by Figure 2-1, showing a mass-spring-damper system, where the displacement of the mass relative to the case is proportional to the applied acceleration. In a closed-loop accelerometer, the restoring force is provided substantially by an electrical spring, either electrostatic or magnetic, instead of a mechanical spring. Also, in a closed-loop design there is a feedback path from the output of the system, through some signal processing elements, and back to the electrical springs. In theory, the mechanical spring behaves in the same manner, except that the feedback is inherent; the force is always proportional to the output (displacement), and the feedback gain is the spring constant K. The important point for this discussion is that closed-loop designs use electrical springs and open-loop designs use mechanical springs.

This is a simple difference between the two, but it affects the design and ultimate performance of the instrument. The spring K, whether it is electrical or mechanical, is a load path between the proof mass and the instrument case. Any external forces other than acceleration that would show up as errors on the output of the sensor, must act through the spring. For example, the process of mounting a sensor will cause output errors, because the screws, epoxy, or whatever is used for mounting, will deform the package and stress the proof mass. These deformations are transmitted through the mechanical spring to the proof mass, where the resulting forces are indistinguishable from acceleration. As another example, temperature is an external influence that might effect the electrical gain of a closed-loop accelerometer. Again, any drift in electrical gain is indistinguishable from an acceleration signal at the sensor's output.

For open-loop operation, the restoring force is purely through the support tethers. These tethers must be stiff enough to put the resonant frequency of the sensor well above the operating bandwidth, yet softer is better with respect to output sensitivity and error rejection. In contrast, support tethers for an accelerometer operating in closed-loop mode should be soft along the input axis since a very stiff restoring force

is provided by the electrical springs.

2.3 Accelerometer Scaling - sensitivity vs. dynamic range

A fundamental design tradeoff exists between the static sensitivity and the dynamic range. We define the sensitivity, S,

$$S \equiv \frac{\delta}{a} \tag{2.1}$$

as the proof mass displacement, δ, for a given input acceleration, a. For frequencies much less than the fundamental resonant frequency, S is approximately equal to the static displacement of the proof mass, δ_{st}, in one $1g$ (gravity) of acceleration,

$$S \approx \frac{\delta_{st}}{g} \tag{2.2}$$

We also know that δ_{st} is a function of the proof mass, M, and the spring constant of the tethers, K,

$$\delta_{st} = \frac{Mg}{K} \tag{2.3}$$

Combining these gives,

$$S = \frac{M}{K} \tag{2.4}$$

The dynamic range is limited by the resonant frequency, f, of the spring-mass system (ignoring damping for now):

$$\omega = \sqrt{\frac{K}{M}} \tag{2.5}$$

$$f = \frac{1}{2\pi}\omega \tag{2.6}$$

Combining Equations 2.5 and 2.4 gives the relationship between the sensitivity

and the undamped dynamic bandwidth,

$$S\omega^2 = 1 \tag{2.7}$$

This tradeoff can also be written as,

$$f = \sqrt{\frac{1}{4\delta_{st}}} \tag{2.8}$$

δ_{st} = static displacement, in meters, for 1g input acceleration

f = fundamental resonance, in Hertz

Sensitivity improves as we design for larger δ per input acceleration. Even if δ is amplified after being transduced to an electrical output, the sensitivity is still limited by the primary output of the accelerometer, which is displacement. On the other hand, for maximum bandwidth, we want the resonant frequency to be high, and so δ must be kept small.

The following example illustrates this design tradeoff. Say we want to measure vibrations out to 1000 Hz. The useful bandwidth for a critically damped accelerometer is about half of the resonant frequency, so we design for a 2000 Hz input axis resonance:

$$\begin{aligned} f &= 2000 \text{ Hz} \\ \delta_{st} &= \tfrac{1}{4f^2} \\ &= .06 \text{ uM per g of input} \end{aligned}$$

This is the static displacements per g that the transducer has available to convert to electrical output. To carry it one step further, let's assume that we want 1ug resolution. Then we must resolve .06 uM/g divided by one million, which is .06 picometers!

2.4 Tether Designs

We look for the following properties in a good tether support system. It should constrain the proof mass to one degree of freedom, that degree of freedom being the

sensitive axis of the accelerometer. In this way, the accelerometer senses acceleration along one axis only, and the output represents both magnitude and direction of acceleration along that axis. The proof mass has a total of six degrees of freedom, so while the tethers must be compliant along the sensitive axis, they must also constrain the proof mass along the remaining five degrees of freedom.

The kinematic response of the tethers should be as linear as possible. That is, the displacement of the proof mass must be linear with respect to the input acceleration. Pendulous designs, for example, are not linear, because accelerations rotate the pendulum, thereby changing the orientation of the sensitive axis. Thus the output is nonlinear with respect to input acceleration.

The tethers should isolate the proof mass from external stresses and strains that might introduce acceleration errors into the sensor. Since the tethers are the mechanical support between the proof mass and instrument case, they have the potential of transmitting external forces to the proof mass. We want the tethers to support the proof mass, but maintain stability of the proof mass down to picometer dimensions.

We have evaluated three tether configurations in this research. They are shown in Figure 2-2. The first of these, which we will refer to as the 'straight tether design', is found frequently in the microsensor literature [4, 8]. It is not particularly good because of its poor strain attenuation, nonlinear response, poor support along the hinge axis, and excessive use of die space.

The second configuration in Figure 2-2, the 'pinwheel design', has better linearity, and less sensitivity to external strains than does the straight design. The pinwheel tethers can bend in-plane and rotate with the proof mass to accommodate external strains. This will be shown in section 2.7, where we find that strain attenuation by the pinwheel design is about 1000 times better than that of the straight tether design. Also, in Section 2.6 we show that the linearity is two to three orders of magnitude better than the straight tether design. Still another advantage of the pinwheel design is that because the tethers run along the length of the proof mass, they can be made quite long without consuming excessive die space. This is important, because if we want to make a very sensitive accelerometer, then the tethers must be very long and

thin.

The 'folded pinwheel' design (Figure 2-2) is similar in performance to the pinwheel design, but goes even further in allowing the design of effectively very long tethers, without using a lot of die space. We can design sensitive accelerometers, using folded tethers, where the tethers are the same thickness as the proof mass. What this means is that the entire accelerometer structure, tethers and proof mass, can be fabricated in a single thin film layer, which is the process we describe in Chapter 4.

2.5 Tether Design Equations and Finite Element Analysis

Our goal is to choose tether dimensions to achieve a given sensitivity, strength, and dynamic range. We want to understand the stiffness of the tethers, the mechanical stresses, and the dynamic resonances for input accelerations along any axis of the sensor. Appendix B contains the equations required for this analysis. These equations give the proof mass deflections and the maximum tether stresses, for 1g accelerations along either the input, pendulous, or hinge axes. Also, the equations give the fundamental resonant frequencies of the accelerometer. The stress and deflection equations assume quasi-static load conditions. That is they assume operation below the fundamental resonant frequency.

In the subsections that follow, the analytical equations in Appendix B are verified with finite element analysis (FEA), and the results are shown in Tables 2.1 through 2.3. This verification is reassuring, because derivation of the equations requires tedious algebra that is prone to error, particularly when we do not know beforehand whether some forces or deflections are zero. This is where the finite element analysis is useful. We check our analytical solutions against the computer solution of the finite element prototype model. This guarantees the correctness of the equations because the finite element solution is essentially exact, within the limits of analytical mechanics.

Development of the analytical equations follows basic beam theory, requiring the

simultaneous solution of the static force and moment balance equations, and the integrated beam equations shown below:

$$\sum F = Ma \tag{2.9}$$

$$\sum m = 0 \tag{2.10}$$

$$\theta(x) = \frac{1}{EI} \int m(x) \cdot \delta x \tag{2.11}$$

$$y(x) = \int \theta(x) \cdot \delta x \tag{2.12}$$

F	=	force
M	=	proof mass
m	=	bending moment
$\theta(x)$	=	beam rotation as a function of distance along beam
m(x)	=	bending moment as a function of distance along beam
y(x)	=	beam displacement as a function of distance along beam
E	=	modulus of elasticity
I	=	bending moment of inertia

Solution of Equations 2.9 through 2.12 gives the displacements, forces, and moments along the tethers. After solving for the displacements, we then calculate the resonant frequencies by equation 2.8.

It might seem that the rotational resonance about either the hinge or about the pendulous axes could be lower than the translational resonance along the input axis. But we can prove that the rotational resonances are about $\sqrt{3}$ times higher than the resonance along the input axis. Using the notation in Figure 2-3, the proof is as follows.

The rotational resonant frequency about either of the cross axes is:

$$f_\theta = \frac{1}{2\pi}\sqrt{\frac{K_\theta}{J}} \tag{2.13}$$

and the resonant frequency along the input axis is:

$$f = \frac{1}{2\pi}\sqrt{\frac{K}{M}} \tag{2.14}$$

f_θ = resonant frequency about either the pendulous or hinge axis

K_θ = rotational stiffness about either the pendulous or hinge axis

J = mass moment of inertia about either the pendulous or hinge axis

f = resonant frequency along the input axis

K = translational stiffness along the input axis

M = proof mass

So the ratio of the two frequencies is:

$$\frac{f_\theta}{f} = \sqrt{\frac{K_\theta}{K}\frac{M}{J}} \tag{2.15}$$

We can write K_θ in terms of K because for rotation about the cross axes the predominant deflection of the tethers is the same s-bending deflection as we get along the input axis. Therefore, the rotational stiffness can be written (with reasonable accuracy) as $K_\theta = \frac{KL^2}{2}$. The rotational mass moment of inertia about a principal axis, for a rectangular block of dimension LxLxT, is, $J = \frac{M}{12}(L^2 + L^2 + T^2)$. For our devices, $T^2 \ll L^2$, and so $J = \frac{ML^2}{6}$. Making these substitutions into equation 2.15 we get:

$$\frac{f_\theta}{f} = \sqrt{3} \tag{2.16}$$

Therefore, the two rotational resonances are always about $\sqrt{3}$ higher than the input axis resonance. Finite element analysis verifies this conclusion.

The stress calculations take into consideration bending stresses, shear stresses, and direct axial stresses; but only significant components are retained. For example, shear stress is not included when calculating the input axis stresses, because the bending stress is orders of magnitude larger.

We used Patran [30] to construct the finite element models and for results post-processing; and Abaqus [31] for the solver. Each of these packages in themselves

performed quite well. Mesh generation is fast and robust in Patran, and the display and post processing options are quite complete. Similarly, Abaqus proved to be accurate and reliable. The element and solution options are numerous and well documented, and Abaqus has extensive capability for nonlinear material and load analysis. Integration of the two packages, however, was a problem. Some Abaqus options are either not supported by Patran, or the method of specifying the option through Patran is not immediately obvious. In other words, there is an additional level of learning involved. In addition to finite element theory, the user must learn two software packages instead of one, plus learn how the interface works between the two. This is not ideal, particularly since so many good integrated packages are available.

The finite element models were constructed with 4-node plate elements for the tethers and for the proof mass. These are the proper elements to use because bending is the predominant deformation mode, as opposed to solid deformation. Beam elements also model the tethers extremely well, but with beam elements it is more difficult to accurately model the torsion; we have to explicitly calculate and input the torsion coefficients, whereas this is automatically taken care of by the plate model. Also, with beam elements, the deformations and stresses are not easy to graphically display when we get to the post-processing phase, because the elements themselves are only lines. So the plates are easier, and more visual than the beam elements. Of course solid continuum elements could have been used instead of plate elements, but then many more elements would have been required to model the bending properties of the tethers, and the models would get far too large (>5000 elements) to easily manage.

2.5.1 Straight Tethers

Figure 2-3 gives dimensions for the straight tether design and defines the axes. Table 2.1 compares the analytic to the FEA results, and we see that the analytic equations are quite accurate. Note that the frequencies, f, are the lowest undamped natural resonances, which are the translational resonance along the input axis, and the rotational resonances about the pendulous axis and about the hinge axis.

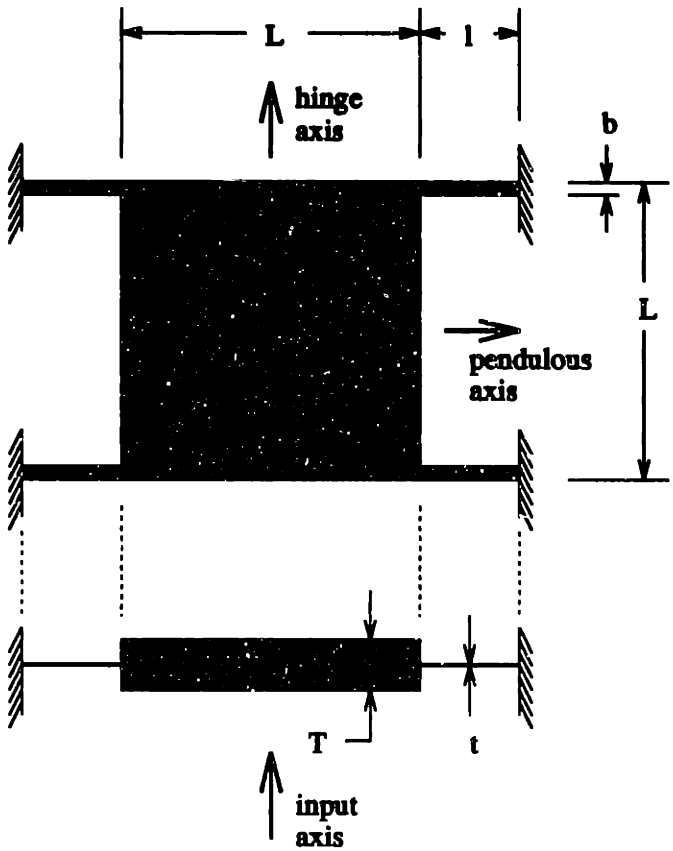

Figure 2-3: Straight tether design.

Axis	δ (uM/g)	σ (MPa/g)	f (Hz)
Input Axis:			
FEA	0.0760	0.976	1808
Analytic	0.0767	1.036	1800
Pendulous Axis:			
FEA	2.76e-6	2.07e-3	3140
Analytic	2.66e-6	2.03e-3	3118
Hinge Axis:			
FEA	8.37e-4	.080	4043
Analytic	7.67e-4	.104	—

Table 2.1: Comparison of the analytical to FEA results for a straight tether design: l =170um, b =10um, t =1um, L =600um, T =10um

For the accelerometer designs of interest here, the primary design constraint turns out to be the desired sensitivity along the input axis. Each tether bends in an 's-bending shape', with zero slope at the endpoints. The stiffness in this mode is $Eb(\frac{t}{l})^3$. In general, we make the thickness as small as the manufacturing process allows, then adjust the length and width to get the desired stiffness.

The cross axis stiffnesses are reasonably good - at least 100 times higher than the stiffness along the input axis. Of course, the stiffness along the hinge direction is not as high as that along the pendulous axis, which is one of the drawbacks of this design. After determining the thickness and length of the tethers to achieve the desired sensitivity, we can adjust the width to get the required cross axis stiffness, without significantly effecting the sensitivity.

With respect to stresses, these are highest for accelerations along the input axis, but they are all still low when compared to the breaking stress of silicon, which is between 100 and 1000 MPa [32]. For the best protection against shock environments, the proof mass should be constrained by top and bottom plates to prevent breaking.

The analytical equations assume that the neutral axes of the tethers are coplanar with that of the proof mass, just as shown in Figure 2-3. For some designs this may not be true. However, we have made calculations that take into account offset tethers, and found the effect to be negligible. For example, for the geometry given in

Axis	δ (uM/g)	σ (MPa/g)	f (Hz)
Input Axis:			
FEA	0.305	1.50	888
Analytic	0.307	1.64	899
Pend/Hinge Axis:			
FEA	9.18e-6	4.13e-3	1256
Analytic	8.42e-6	4.51e-3	1557

Table 2.2: Comparison of the analytical to FEA results for a pinwheel tether design: l =270um, b =10um, t =1um, L =750um, T =10um, and the proof mass is perforated by a 9x9 grid of 50x50um square holes.

Table 2.1, by moving the tethers 5 um offcenter, the only effect was to add another resonance at about 300 KHz.

2.5.2 Pinwheel Tethers

Figure 2-4 gives the dimensions for the pinwheel tether design, and Table 2.2 compares the finite element results to the analytical results. Also, Figure 2-5 shows the FEA model used for verification of the analytical equations. The first deflection plot in Figure 2-5 is for 1g input acceleration, and the second is for a 1g cross axis input. In this example, the design includes perforations in the proof mass to reduce gas damping effects, but even with these perforations, the closed form equations from Appendix B are still quite accurate. The biggest error is in the calculation of the resonance about the pendulous or hinge axis. This error results from the approximation of a uniform density proof mass in the derivation of equation 2.16, which is no longer valid because of the perforations.

The design equations for the input axis are exactly the same as the straight tether equations. In a linear analysis, the tethers deform in the same s-bending shape with zero slope at the ends. We see in section 2.6 , however, that when the nonlinearity associated with stretching of the tethers is accounted for, the pinwheel tether design has a much more linear response than does the straight tether design.

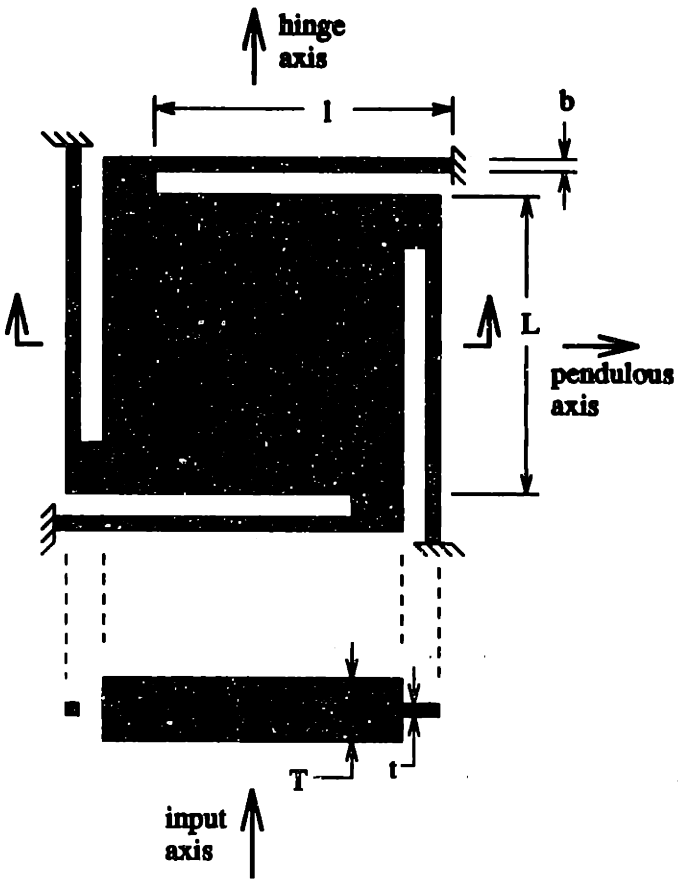

Figure 2-4: Pinwheel tether design.

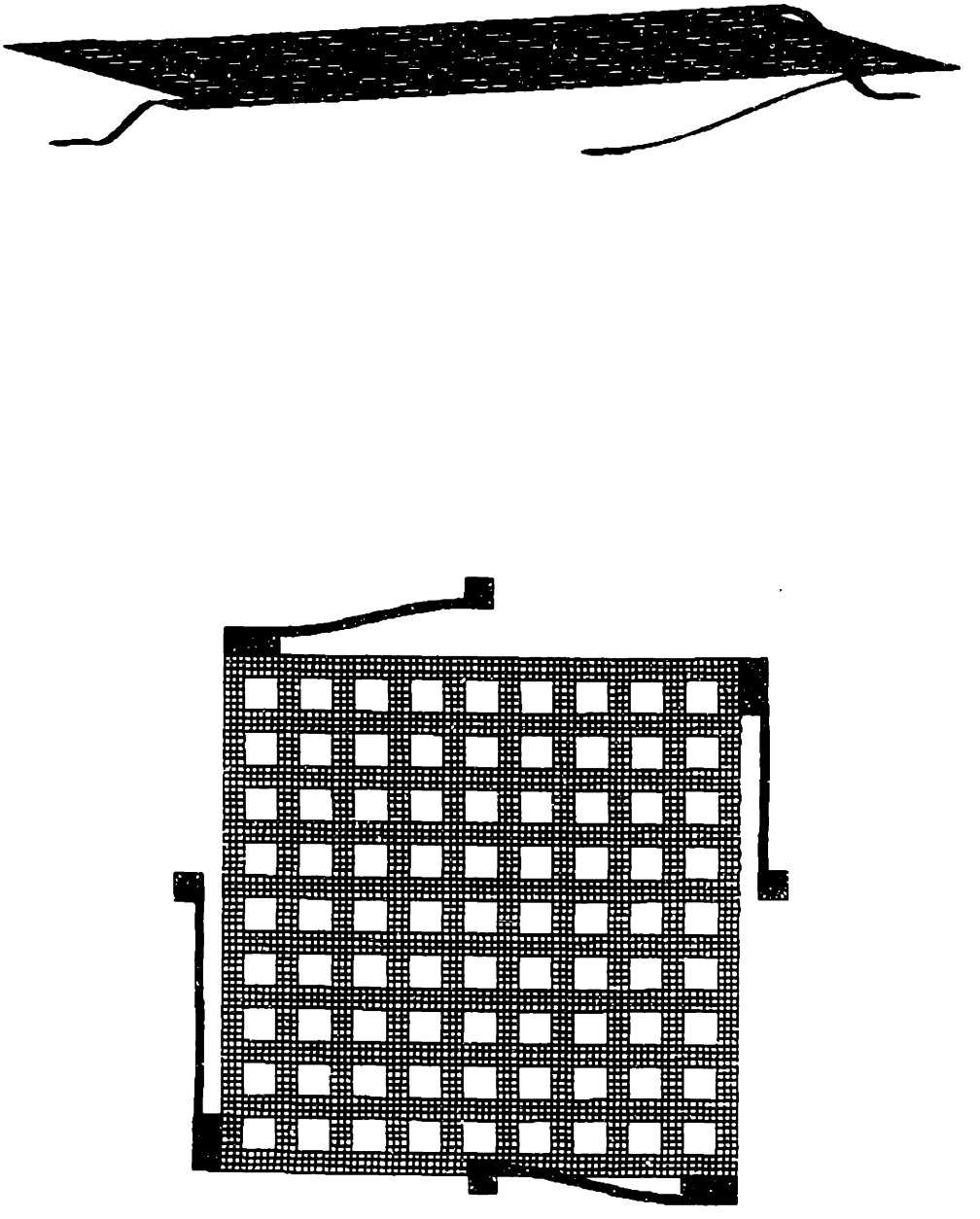

Figure 2-5: Finite element model of a pinwheel design: a) deflection plot for 1g input acceleration, and b) deflection plot for 1g cross axis acceleration.

Axis	δ (uM/g)	σ (MPa/g)	f (Hz)
Input Axis:			
FEA	0.0627	0.729	1956
Analytic	0.0701	0.729	1883
Pend/Hinge Axis:			
FEA	3.82e-4	.0364	3022
Analytic	3.66e-4	.0414	3261

Table 2.3: Comparison of the analytical to FEA results for a folded pinwheel tether design: l =105um, b =10um, t =1um, s=50um, w=10um, L =750um, T =10um, and the proof mass is perforated by a 9x9 grid of 50x50um square holes.

2.5.3 Folded Pinwheel Tethers

The analysis is considerably more complex for the folded pinwheel. Figure 2-6 gives the dimensions for the problem. As with the preceding two designs, the analytical results are compared to an FEA model. The FEA model is shown in Figure 2-7, and the results comparison is made in Table 2.3.

For the input axis deflection we have to include torsion as well as bending, in all three segments of each tether. When the length of the connecting segment s is small, then the folded tether acts much like two s-bending tethers acting in series. But when s gets longer, we get more torsional deflection from each of the main tethers, plus significant bending of the connecting tether.

A notable characteristic of this tether configuration, and one that is not immediately obvious, is that the three translational degrees of freedom are decoupled, just as they were with the straight and the pinwheel designs. Knowledge of this, which came by study of the FEA results, made the development of the closed form equations much easier.

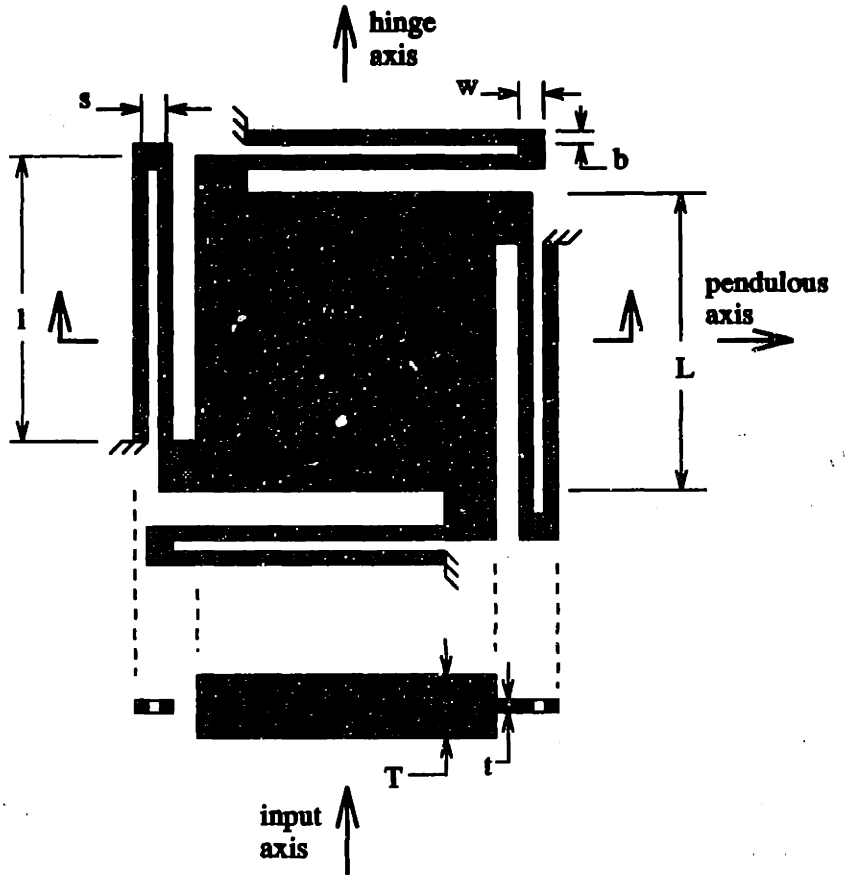

Figure 2-6: Folded pinwheel design

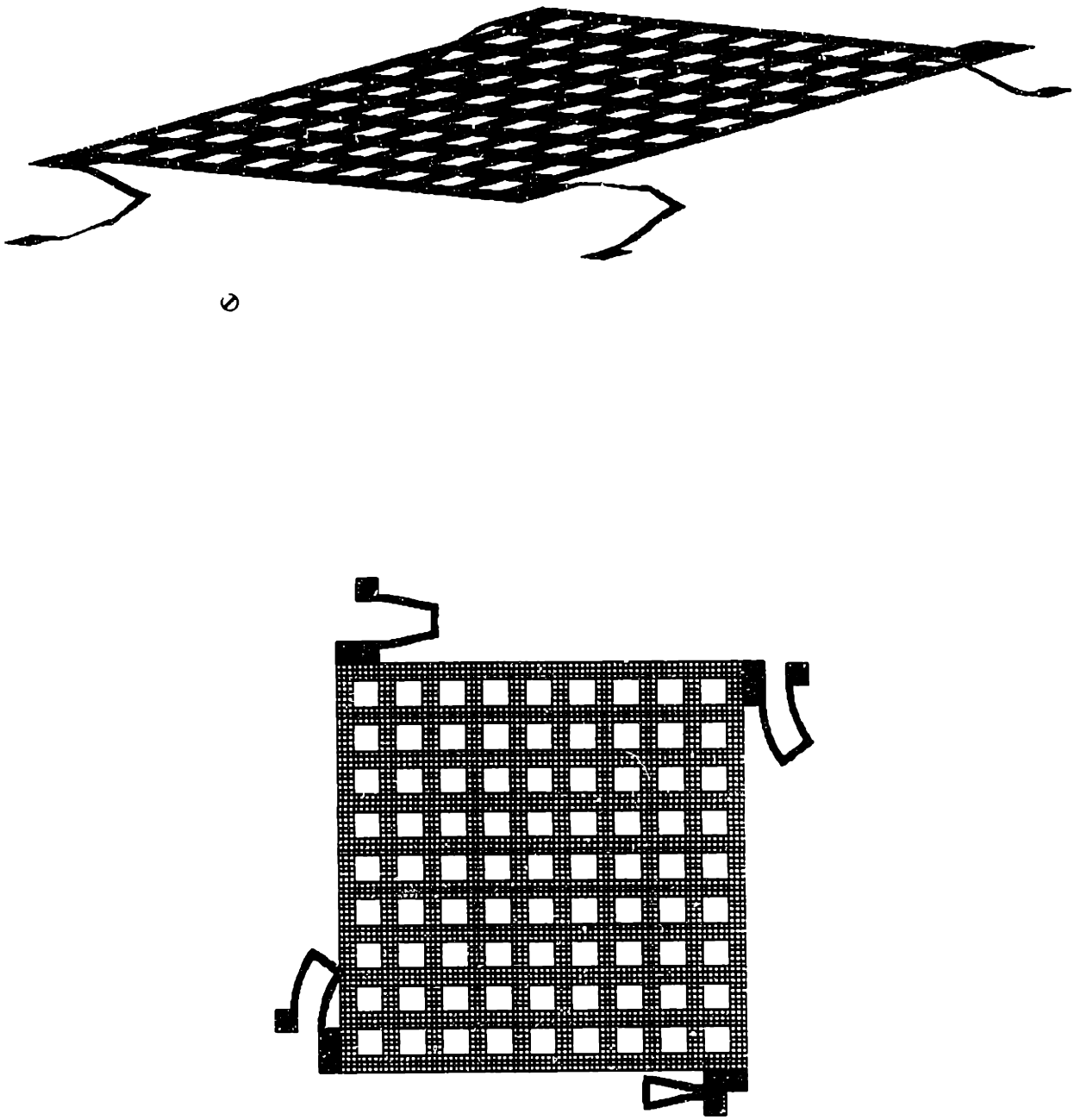

Figure 2-7: Finite element model of a folded pinwheel design: a) deflection plot for 1g input acceleration, and b) deflection plot for 1g cross axis acceleration.

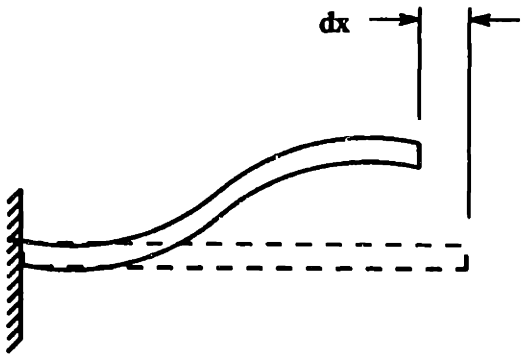

Figure 2-8: Nonlinear shortening effect in a bending tether.

2.6 Linearity

An accelerometer's output should be linear with respect to the input acceleration. Otherwise, external linearization circuits or a nonlinear calibration equation is required to use the instrument. Even more serious, in dynamic environments, nonlinearities cause vibration rectification, which is a DC offset in the time-averaged AC output. In this section, the impact of one known source of nonlinearity is investigated. This is the shortening of the tethers as they bend in response to input accelerations. As shown in Figure 2-8, s-bending of a tether in the y-direction, also results in shortening δx along the x-direction. If the tether is not free to displace in the x-direction, then an axial load develops in the tether, and this load in turn increases the bending stiffness of the tether.

What is the effect of tether shortening for the three designs in Figure 2-2? The effect is most serious with the straight tether design because essentially it does not accommodate δx at all. Because of this, large axial loads develop and the tether stiffness changes dramatically. The two pinwheel designs can rotate to allow shortening, and so the axial loads and the nonlinearity are much smaller, although not zero. We could completely eliminate the shortening problem by using the proof mass and tether configuration shown in Figure 2-9. This is a slight modification to the

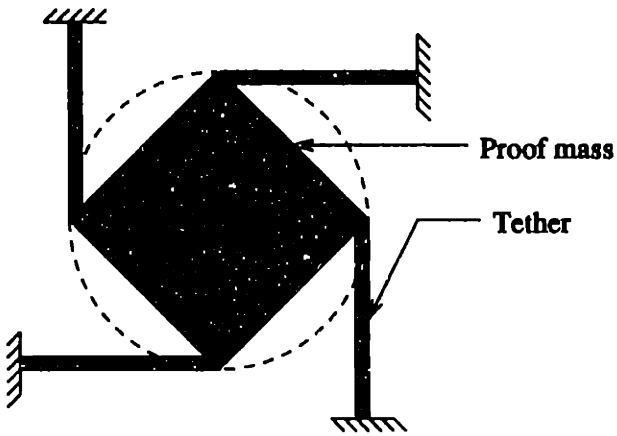

Figure 2-9: A tether configuration with zero nonlinearity.

pinwheel design, where now the tethers are tangent to the circle that inscribes the points where the tethers attach to the proof mass.

Analytical formulation of the shortening problem is easy for the straight tether configuration, and we can even solve it with a hand calculator by iterating on the nonlinear equations. The procedure for this is given in Appendix C. For the two pinwheel designs, the problem formulation is much more difficult because the tether end condition is neither fixed nor free. It is not completely fixed against shortening as it is with the straight tether design, yet it is not completely free to shorten as the design is in Figure 2-9. Since the end conditions depend upon the specific tether configuration, an analytical model would have to include flexible end conditions.

Even for the straight tether design the analytical formulation does not yield a closed form solution. Instead, we have to iterate numerically to the solution. So, the approach taken here is to use simple finite element models (< 200 elements), and to let the FEA program do the iteration for us. Before doing this, we first checked that the method in Appendix C gives the exact same result as the ABAQUS nonlinear FEA solution. Then we used the FEA to calculate the nonlinearity for each of the three tether configurations. The models and the results are summarized in Figure

2-10.

We see in Figure 2-10 that the nonlinearity for the pinwheel design is only ±.05%, compared to ±20% deviation from linearity for the straight tether design. Also shown is the extremely low nonlinearity that can be achieved with the design shown in Figure 2-9.

The three designs in Figure 2-10 all have the same sensitivity: about 1um deflection for 20g input. The proof masses are 500x500x10um; and the tethers are each 150x5x1um. The finite element models used one hundred 4-node plate elements for the proof mass, and four 3-node beam elements for each tether. Each model was first run to determine the linear responses, using the STATIC,LINEAR option in ABAQUS. Then, four more runs (5g,10g,15g,20g loads) using the STATIC,NLGEOM (nonlinear geometry) option were made to determine the nonlinear response. The plotted nonlinearity is then:

$$\%nonlinearity = 100 \cdot \frac{\delta_{linear} - \delta_{nonlinear}}{\delta_{linear}} \tag{2.17}$$

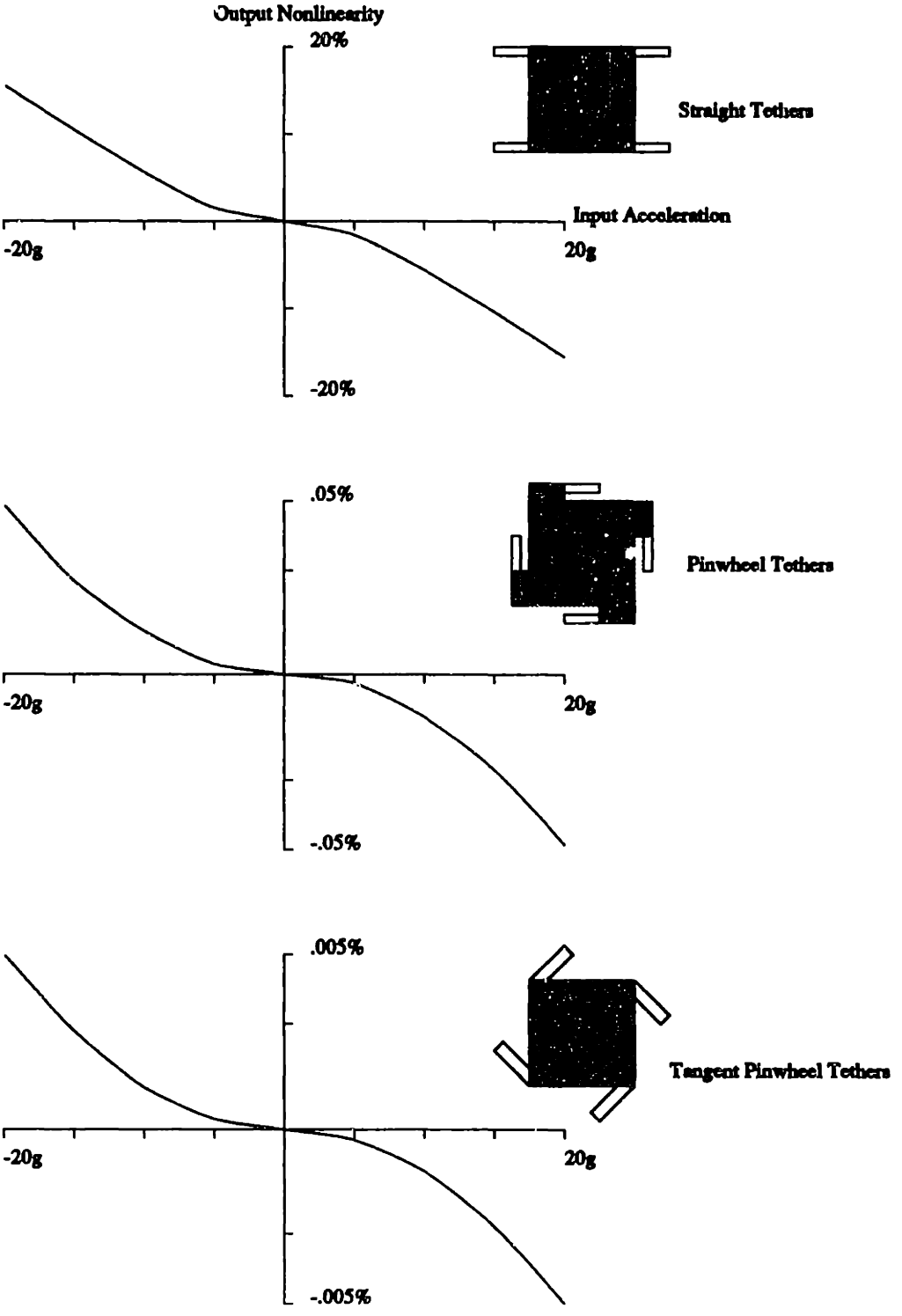

Figure 2-10: Nonlinearity in the response of three different tether configurations vs. input acceleration. All three configurations have the same linear sensitivity: .05um displacement per g of input acceleration. Thus a $\pm$ 20g input corresponds to a displacement of one tether thickness.

2.7 Strain Attenuation

External stresses and strains are a real, and undesirable, part of any sensor's operating environment. For instance, consider the effect of thermal strains. If the sensor material is silicon, with thermal coefficient of expansion 2.6 ppm/$°C$; and the sensor is mounted to an alumina IC package, with thermal coefficient of expansion 5.6 ppm/$°C$; then the strain imparted to the sensor will be on the order of (5.6 - 2.6) = 3 ppm/$°C$. Therefore, a 10 $°C$ change in temperature would deform a 2mm sensor by .06 um. This causes large acceleration errors when the tethers transmit these strains as forces onto the proof mass.

As another example, consider residual strains in the accelerometer material. Some planar processes used in silicon micromachining leave significant residual stress in the film. Boron doping to form etch stops results in 30 Mpa tensile stress [33]. Polysilicon films are typically compressive as deposited, but may become tensile when annealed [34]. The tether configuration must allow these stresses to relieve themselves, or the stresses will change the scale factor of the senor, and may even buckle or fracture the tethers in the extreme case.

Analytical evaluation of the errors requires some assumption about the external strain acting on the sensor. The assumption used here is that the strain is a uniform expansion (or contraction) of the surface upon which the sensor is bonded. We could simulate this experimentally by mounting the sensor to a rigid surface in a stress free manner, and then raising the temperature of the surface without changing the temperature of the sensor.

Figure 2-11 shows this external strain acting on the straight tether design. There is no attenuation of the strain; all of it is carried through the tethers as an axial force, given by:

$$P = \frac{btE}{l} \cdot \delta \tag{2.18}$$

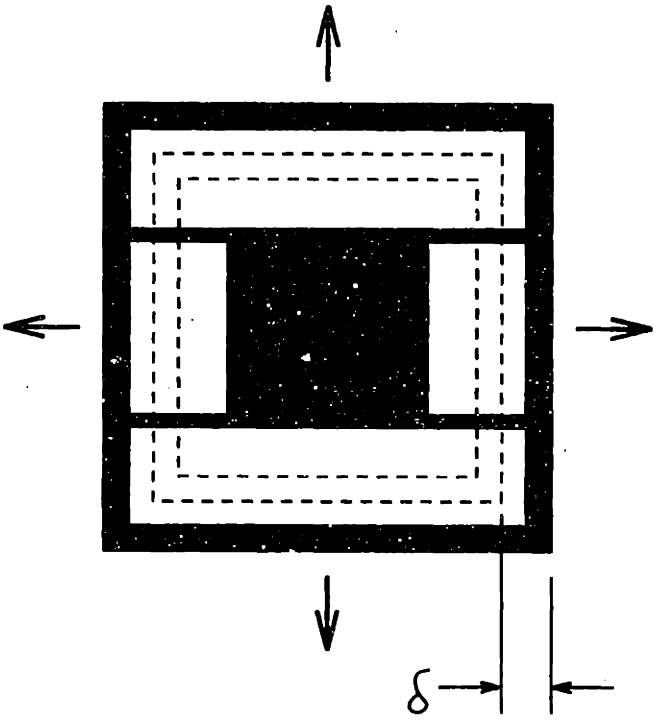

Figure 2-11: Strain on straight tether design.

P = axial force in the tether

b = tether width

t = tether thickness

E = modulus of elasticity

l = tether length

δ = displacement caused by external strain

The axial force P in turn changes the sensitivity of the accelerometer because of the stress stiffening effect. Stress stiffening is the change in bending stiffness of a beam due to axial loading of the beam. This change in bending stiffness is [35],

$$\delta K = \frac{(1.2)P}{l} \tag{2.19}$$

The stiffness K of each tether is:

$$K = Eb(\frac{t}{l})^3 \tag{2.20}$$

Therefore, the relative error, ϵ, caused by an external strain displacement δ on the sensitivity of a straight tether design is:

$$\epsilon = (1.2)\frac{l}{t^2}\delta \tag{2.21}$$

As an example, let,

b = 5um

t = 1um

l = 150um

then we calculate, using Equation 2.21, that an instability of only $\delta = 2.8$ $\mathring{A}$ results in a 5% change in the sensitivity. Again, using the example of mounting a 2 mm silicon die to an alumina package, we can calculate the change in temperature, ΔT that would generate a δ of 2.8 $\mathring{A}$,

$$\Delta T = \frac{2.8\mathring{A}}{(3ppm/^\circ C)2mm}$$
$$= .047^\circ C$$

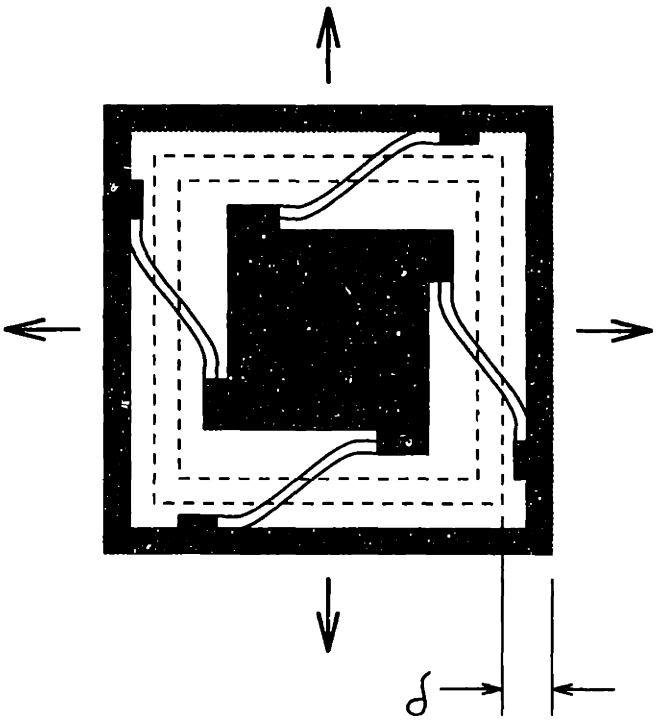

Figure 2-12: Strain on pinwheel design

Now consider the effect of the same instability imposed on the pinwheel design. As shown in Figure 2-12, the tethers bend in the plane of the proof mass to accommodate δ. The resulting axial force P depends upon the length of the tether l, and the ratio of the tether length to the proof mass length, $\frac{l}{L}$. Using the notation shown in Figure 2-4, δ creates an axial force in the tethers given by:

$$P = -2Et\left(\frac{b}{l}\right)^3 \frac{(1-\frac{l}{L})^2}{\sqrt{4(\frac{l}{L})^2 - 4\frac{l}{L} + 2}} \cdot \delta \tag{2.22}$$

When we plot the last quotient in equation 2.22 as a function of $\frac{l}{L}$, we find that within the range of $0 < \frac{l}{L} < 2$, the maximum value of the quotient is 0.7. Therefore, using 0.7 as a limit on the quotient, we can simplify equation 2.22 to

$$P = -2Et\left(\frac{b}{l}\right)^3 (0.7) \cdot \delta \tag{2.23}$$

This creates an error in the sensitivity of

$$\epsilon = (1.7)\left(\frac{b}{t}\right)^2 \frac{\delta}{l} \tag{2.24}$$

Repeating the example calculation used for the straight tether design:

$$\begin{aligned} b &= 5\text{um} \\ t &= 1\text{um} \\ l &= 150\text{um} \end{aligned}$$

then we calculate that it takes an instability of δ=.25 um to cause 5% change in the sensitivity of a pinwheel type accelerometer, which is about a 1000 times better attenuation of strain by the pinwheel design as compared to the straight tether design.

Chapter 3

Dynamic Response and Squeeze Film Damping

3.1 Overview

In dynamic environments, the gas between the proof mass and the electrode plates substantially influences the accelerometer's dynamic response. Damping forces are generated as the gas squeezes in and out between the plates; the so called squeeze film damping effect. The damping forces in thin film accelerometers tend to be extremely high, leading to sluggish dynamic response. Capacitive sensing designs are particularly bothered by damping because of the large electrode surfaces and small gap that are required to get good sensing capacitance.

This chapter explains how to calculate, and how to control the squeeze film damping. First, in Section 3.2, we calculate the damping coefficient and the dynamic response for a typical design. It turns out for the example, which has a 2000 Hz undamped resonance, that damping limits the useful bandwidth to only 1 Hz. Given this poor dynamic response, we chose to perforate the proof mass in order to reduce the damping. Section 3.3 explains why we picked this option over several others. The perforations are compatible with thin film processing and add very little to the manufacturing cost. Section 3.4 shows how to design a perforated proof mass, using finite element analysis in a particularly efficient manner. Section 3.5 shows the design

after modification to achieve critical damping.

3.2 Dynamic Response

We use the mechanical model in Figure 2-1 to predict the accelerometer's dynamic response. M is the proof mass, K is the tether stiffness, and B is the gas damping coefficient. The acceleration input is periodic in time, $a_i = A_i sin(\omega t)$. A quasi-static balance of forces on the proof mass yields the equation for the sensor's output displacement, x_o.

$$\ddot{x_o} + \frac{B}{M}\dot{x_o} + \frac{K}{M}x_o = a_i \tag{3.1}$$

$$\begin{aligned}
x_o &= \text{proof mass displacement} \\
&= X_o sin(\omega t + \phi) \\
X_o &= \text{maximum displacement} \\
\omega &= \text{frequency} \\
t &= \text{time} \\
\phi &= \text{phase lag relative to input} \\
a_i &= \text{input acceleration} \\
&= A_i sin(\omega t) \\
A_i &= \text{maximum input acceleration} \\
M &= \text{proof mass} \\
B &= \text{gas damping coefficient} \\
K &= \text{tether stiffness}
\end{aligned}$$

This is a second order, ordinary differential equation. The solution gives the amplitude response, $M(\omega)$, and the phase response, $\phi(\omega)$ as a function of frequency [36].

$$M(\omega) = \frac{K}{M}\left|\frac{X_o}{A_i}\right| = \frac{1}{\sqrt{\left[1 - \left(\frac{\omega}{\omega_n}\right)^2\right]^2 + \left(2\zeta\frac{\omega}{\omega_n}\right)^2}} \tag{3.2}$$

$$\phi(\omega) = -arctan\left[\frac{2\zeta(\omega/\omega_n)}{1-(\omega^2/\omega_n^2)}\right] \tag{3.3}$$

$$\begin{aligned} \omega_n &= \text{undamped resonant frequency} \\ &\equiv \sqrt{K/M} \\ \zeta &= \text{damping ratio} \\ &\equiv \frac{B/M}{2\omega_n} \end{aligned}$$

For values of the damping ratio $\zeta < \frac{1}{\sqrt{2}}$, there is some peaking in the amplitude response, $M(\omega) > 1$. But for $\zeta \geq \frac{1}{\sqrt{2}}$, the amplitude response never exceeds unity. We achieve the widest dynamic range when $\zeta = \frac{1}{\sqrt{2}}$, which is called the critical damping ratio, ζ_{cr}. The phase response is actually better when the damping ratio is smaller than ζ_{cr}. For some applications, fast response of the accelerometer is more important than the amplitude information. In this case, we would want a damping ratio much less than critical.

As an example, let ω_n=2000 Hz, and consider three values for ζ: ζ= .1, .707, 2. Table 3.1 compares the amplitude and phase response at ω=1000 Hz for the three different damping ratios. The amplitude is closest to unity when $\zeta = \zeta_{cr}$, but we get better phase response with $\zeta < \zeta_{cr}$.

Now consider the response of one possible accelerometer design, as shown in Figure 3-1. This shows a proof mass supported by four tethers, and a lower electrode plate to provide the capacitive output. The 1 um gap is necessarily small to achieve good sensitivity, and for the same reason, the proof mass dimension, L=500 um, is relatively large. We can choose the tether dimensions to achieve any desired undamped resonance, ω_n, as explained in Section 2.3. Say that $\omega_n = 2000\ Hz$. All that is needed now to completely describe the dynamic response is the damping ratio, $\zeta = \frac{B/M}{2\omega_n}$. To calculate B, we use Equation D.36, which is repeated here.

$$B = 0.4217\ \mu\frac{L^4}{h^3} \tag{3.4}$$

	ζ=.1	$\zeta = \zeta_{cr}$	ζ=2
$M(\omega = 1000\ Hz)$	1.32	0.97	0.47
$\phi(\omega = 1000\ Hz)$	$-8°$	$-43°$	$-69°$

Table 3.1: Example of amplitude and phase response, at 1000 Hz, for three accelerometer designs with different damping ratios. The undamped resonance is 2000 Hz for all three.

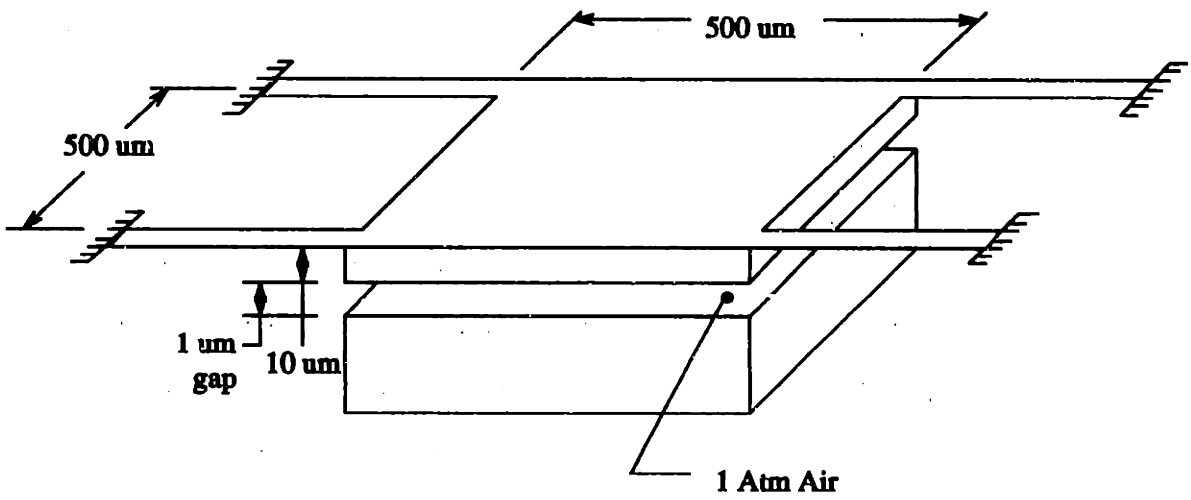

Figure 3-1: A possible μaccelerometer design, demonstrating extreme overdamping in the dynamic response.

$$
\begin{aligned}
B &= \text{damping coefficient} \\
\mu &= \text{viscosity of air} \\
&= 1.8 \cdot 10^{-5} \tfrac{n \cdot s}{m^2} \text{ for air at 1 atm, 20 } ^\circ C \\
L &= \text{proof mass side length} \\
h &= \text{gap dimension}
\end{aligned}
$$

Substituting the dimensions from Figure 3-1 into Equation 3.4,

$$
\begin{aligned}
B &= .4217 \left(1.8 \cdot 10^{-5} \tfrac{n \cdot s}{m^2}\right) \tfrac{(500 \cdot 10^{-6} m)^4}{(1 \cdot 10^{-6} m)^3} \\
&= .4744 \tfrac{n \cdot s}{m}
\end{aligned}
$$

And the proof mass M is calculated as,

$$
\begin{aligned}
M &= (10um)(500um)(500um)(2.3 \cdot 10^{-15} \tfrac{kg}{um^3}) \\
&= 5.75 \cdot 10^{-9} kg
\end{aligned}
$$

And the damping ratio is given by,

$$
\begin{aligned}
\zeta &= \tfrac{B/M}{2\omega_n} \\
&= \tfrac{\left(.4744 \tfrac{n \cdot s}{m}\right) / \left(5.75 \cdot 10^{-9} kg\right)}{2(2\pi \cdot 2000 Hz)} \\
&= 3282
\end{aligned}
$$

With this value for ζ, and ω_n=2000 Hz, we plot the amplitude response as the solid line in Figure 3-2. This indicates a useful dynamic range from 0 Hz to 1 Hz. The dashed line is the dynamic response if the sensor were critically damped, showing a much larger dynamic range out to about 1000 Hz.

These calculations indicate that a significant change must be made to the basic design in Figure 3-1. We would like to reduce the damping by about three orders of magnitude. In the next section we review the design options to achieve this reduction.

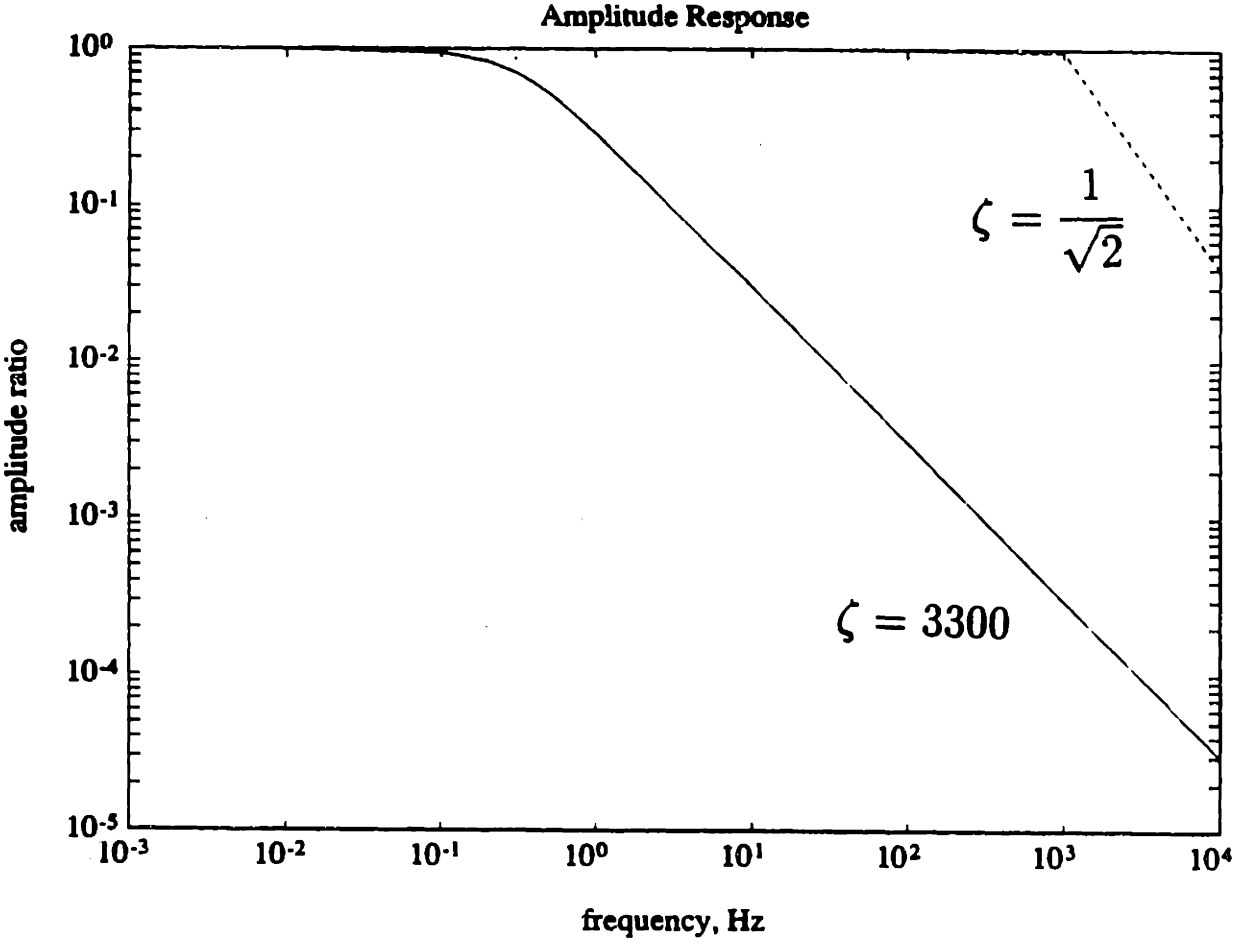

Figure 3-2: Amplitude response of the overdamped accelerometer of Figure 3-2 (solid line), compared to the response if it were critically damped (dashed line).

3.3 Options for Damping Reduction

A number of options exist to reduce the gas damping and thereby improve the dynamic response. In this section we present the advantages and disadvantages for some of these options, and explain why we chose to perforate the proof mass with pressure vent holes.

3.3.1 Vacuum Package

Packaging the sensor in vacuum is one way to reduce damping. An advantage here is simplicity. Either the 3-wafer stack could be bonded together in a vacuum, or the entire final assembly could be vacuum packaged. A disadvantage is controlling the process to achieve a particular damping ratio. Vacuum packaging will easily achieve a very low damping ratio, but to get critical damping exactly, requires precise control over the final pressure. Additionally, temperature and external pressure will effect the internal pressure and thus the sensor's dynamic response. And finally, we would expect vacuum packaging to substantially increase manufacturing costs.

3.3.2 Large Damping Gap, and/or Thick Proof Mass

The damping ratio decreases as we increase the gap dimension, or as we increase the proof mass thickness. However, the resulting sensor dimensions are incompatible with thin film processes. To see this, consider the capacitance and damping equations for a square plate. First, the capacitance is given by,

$$C = \epsilon \frac{L^2}{h} \tag{3.5}$$

C = capacitance

ϵ = permittivity

L = proof mass side length

h = gap dimension

For the damping ratio, from the definition of ζ in Equation 3.3,

$$\zeta \equiv \frac{B/M}{2\omega_n} \tag{3.6}$$

It is ζ that we want to reduce, but this is done by reducing B/M, since ω_n is fixed (Section 2.3). Therefore, write B/M, using Equation D.36 for B, and M is just the proof mass volume times the density,

$$\begin{aligned} \frac{B}{M} &= \frac{(.4217)\mu\frac{L^4}{h^3}}{dL^2T} \\ &= \frac{(.4217)\mu}{d}\frac{L^2}{Th^3} \end{aligned} \tag{3.7}$$

d = mass density

T = proof mass thickness

In Equations 3.5 and 3.7, we see that L has the same effect on the capacitance as it does on the damping ratio. Reducing L, quadratically reduces both the damping ratio and the capacitance. So if the capacitance is to stay fixed, we cannot use L to reduce the damping ratio. We can, however, use T, the proof mass thickness, to reduce the damping ratio without any lose in capacitance. This is helpful, but the dependence is only linear. The gap dimension, h, has the strongest effect on the damping ratio. However, as we increase the gap, we must also increase the plate area to compensate for the loss in capacitance.

To experiment with these dimensional changes, we will modify the design in Figure 3-1 to achieve critical damping. We keep the capacitance constant at $C = 1.5$ pF, but decrease the damping ratio from $\zeta = 3282$ to .707. We vary only the proof mass length and thickness, and the gap dimension. Some values are tabulated in Table 3.2. Notice that this table somewhat bounds the extreme values for the proof mass thickness and the gap dimension.

All three of the tabulated designs preclude the use of thin film processes. For example, the second design. The proof mass thickness is nearly the full wafer thickness,

gap dimension h (um)	proof mass length L(um)	proof mass thickness T (um)
1	500	46,421
10	1581	464
50	3536	19

Table 3.2: Alternative dimensions for Figure 3-2 to achieve critical damping. Capacitance is kept constant at 1.5 pF.

and the gap dimension of 10 um is quite large for thin films.

3.3.3 Perforated Proof Mass

Perforating the proof mass reduces damping pressure without sacrificing capacitance. To show this, we approximate a perforated proof mass as a collection of square damping surfaces acting independently of one another, as shown in Figure 3-3. Starting with Equations 3.5 and 3.7, and using the same notation, except that now L is the side length of each little square, and N is the total number of squares making up the proof mass, then,

$$C = N\epsilon\frac{L^2}{h} \tag{3.8}$$

$$\begin{aligned}\frac{B}{M} &= \frac{N(.4217)\mu\frac{L^4}{h^3}}{NdL^2T} \\ &= \frac{(.4217)\mu}{d}\frac{L^2}{Th^3}\end{aligned} \tag{3.9}$$

We see that B/M does not depend on the total number of damping surfaces, N. Instead, B/M, and therefore also the damping ratio ζ, is determined by the damping ratio of each individual square. If we can design an individual square with the right B/M ratio, then we simply combine enough of these together to form a proof mass with the desired capacitance. Essentially, this gives us another parameter, N, by which to set the capacitance without effecting the damping.

Again, we now try to modify the design in Figure 3-1 to achieve critical damping,

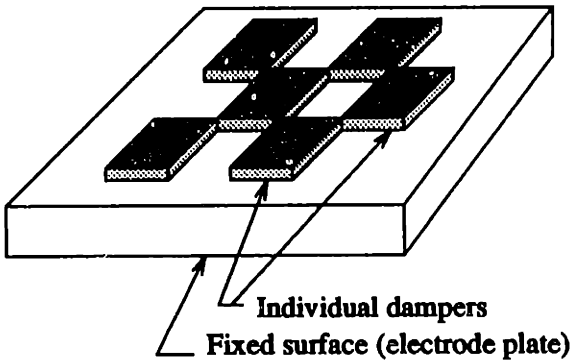

Figure 3-3: Approximation of a perforated proof mass as a collection of independent damping surfaces.

while keeping the capacitance constant at 1.5 pF. Table 3.3 indicates some reasonable designs with this approach. We can stay with thin film processes because the gap dimension is small, 1-2 um, and the proof mass remains thin, 10-20 um. The perforation patterns are reasonable, 7 to 30 um squares separated by the same size holes. The proof mass dimension has increased considerably. However, in these calculations we have assumed that the holes are the same size as the damping squares. A more compact design would use holes as small as possible to separate the damping surfaces. In summary, we want very small holes, closely spaced, to reduce the damping and still maintain a small die size. Of course, fabrication processes will determine the minimum hole size possible.

gap dimension h (um)	proof mass thickness T (um)	length of individual square L (um)	total number of squares N	total proof mass length $2\sqrt{N}L$ (um)
1.0	10	7	4642	954
1.5	10	13	2219	1225
2.0	10	21	1134	1414
1.0	20	10	2500	1000
1.5	20	19	1039	1225
2.0	20	30	556	1415

Table 3.3: Alternative dimensions for Figure 3-2 to achieve critical damping using a perforated proof mass. Capacitance is held constant at 1.5 pF.

3.4 Design of the Perforated Proof Mass by Finite Element Analysis

To design the perforated proof mass, we require some method to accurately calculate the damping. The simple model in Figure 3-3 is useful for feasibility studies, but not for detailed design calculations. Reynolds' equation still applies, Equation D.19. The difficulty is how to solve this equation on a perforated plate. The solution is difficult even for a solid square plate. For the perforated plate, we rely on finite element methods to find the damping coefficients.

3.4.1 FEA Procedure and Verification

Our finite element program, ABAQUS, does not have an element formulated specifically for gas damping. However, the 2-dimensional heat transfer elements can be used since they are based on Poisson's equation [35, 37]. The heat transfer elements solve the heat conduction equation for temperature, T.

$$\frac{\delta^2 T}{\delta x^2} + \frac{\delta^2 T}{\delta y^2} = Q \tag{3.10}$$

T = temperature

Q = heat source per unit volume

x, y = cartesian coordinates

This is analogous to Reynolds' equation for the squeeze film damping pressure, P, (Equation D.19),

$$\frac{\delta^2 P}{\delta x^2} + \frac{\delta^2 P}{\delta y^2} = \frac{-12\mu V}{h^3} \tag{3.11}$$

The following procedure was used with ABAQUS to find the damping ratio of a perforated proof mass:

1. Construct the finite element mesh of the plate. Use the ABAQUS element for 2-dimensional heat transfer, element type DC2D4. These are one degree of freedom per node elements, with temperature (or pressure in this case) as the unknown. Use elements of equal size to simplify step 6.

2. Apply the boundary conditions. Set the pressure to zero at all nodes around the plate edges, and at all nodes around the holes.

3. Specify the material properties. The only property of importance is the thermal conductivity. Set this equal to 1.

4. Apply the 'loads'. Enter the loads as if they were sources of heat generation per unit volume. On each element, enter $Q = (-12\mu V)/h^3$. The velocity term is arbitrary, since we divide it out in the calculation of the damping coefficient, $B = F/V$.

5. Run the analysis to solve for the pressure distribution.

6. Integrate the pressure over the plate area to get the damping force. Many FEA programs will do this for you, but ABAQUS will not. So, write the nodal pressures to an ASCII file, and use MatLab to sum the pressures. Multiply this summation by the area of each element (which is why we used equal-sized elements for the mesh construction) to get the force, F.

7. Calculate the damping coefficient, $B = F/V$

8. Calculate the damping ratio, $\zeta = B/M$, where M is the mass of the plate.

Figure 3-4 shows an FEA model that we used to verify this procedure. This is a square plate, 500x500 um. The mesh is 50x50 elements, so each element is 10 um square. The gap dimension is 1um, and the gas is air, with viscosity of $\mu = 1.8 \cdot 10^{-11} \frac{kg}{um \cdot sec}$. The appropriate velocity to use depends on the magnitude and frequency of the input vibration. For example, if the input vibration displaces the proof mass a maximum of .05 um at 2000 Hz, then the maximum velocity would be,

$$V = (.05um)(2000Hz) = 628um/s$$

We used 1000 um/s in this analysis. Therefore, we enter the source term as,

$$Q = \frac{-12\mu V}{h^3} = \frac{-12\left(1.8 \cdot 10^{-11} \frac{kg}{um \cdot sec}\right)\left(1000 \frac{um}{sec}\right)}{(1um)^3} = -.00216 \frac{kg}{um^3 \cdot sec^2}$$

Figure 3-4 shows the resulting pressure contours. The maximum pressure is 3.98 KPa at the center of the plate. Note that this maximum change in pressure is about 4% of ambient atmospheric pressure. Integration of the pressure over the area, using MatLab, gives,

$$F = 4.74 \cdot 10^{-4} N$$

and the damping coefficient is,

$$B = F/V = \frac{4.74 \cdot 10^{-4}\ N}{1 \cdot 10^{-3} \frac{m}{sec}} = .474 \frac{kg}{sec}$$

We want to compare this to the closed form solution, Equation 3.4,

$$B = (.4217)\frac{\mu L^4}{h^3} = (.4217)\frac{\left(1.8 \cdot 10^{-11} \frac{kg}{um \cdot sec}\right)(500\ um)^4}{(1\ um)^3} = .474 \frac{kg}{sec}$$

So the finite element analysis gives the exact same answer as the closed-form solution. With this reassurance, we now use the FEA to design a perforated proof

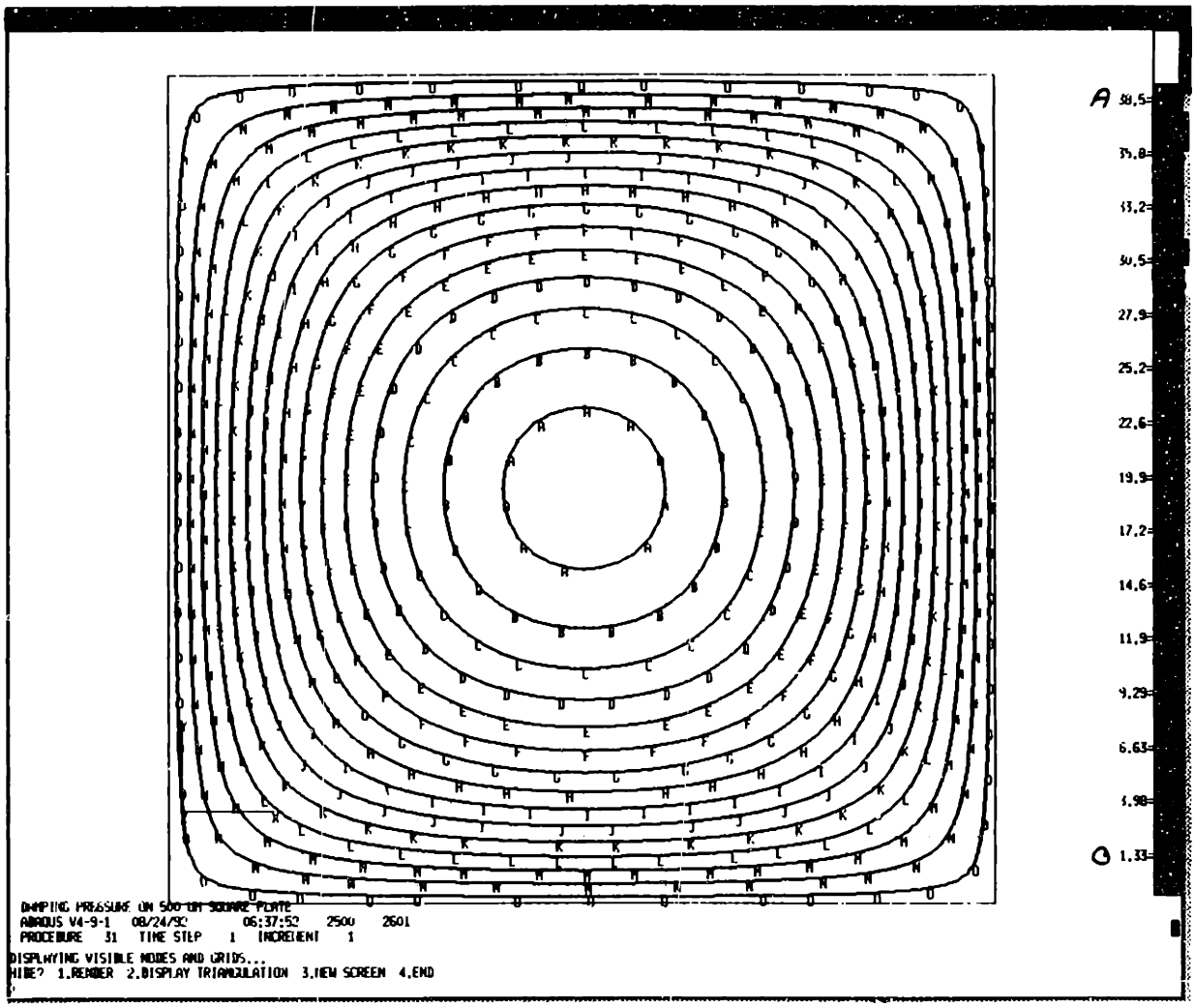

Figure 3-4: Damping pressure contours. The damping coefficient calculated from this finite element analysis agrees exactly with that from the closed-form analytical solution.

mass.

3.4.2 Using Symmetry to Simplify Models

We need a substantial number of perforations to achieve critical damping. For example, adding 9 holes to Figure 3-4 has the effect shown in Figure 3-5. The maximum damping pressure is lower, but only by about a factor of 10. We want to get a 1000 times reduction. Here lies a problem with the finite element analysis, because the models get quite difficult to build when they have, say, 100 holes. The number of elements goes up rapidly also; at least 10,000 elements would be needed for a 100-hole

proof mass.

But the solution has a strong repetitive pattern. The box in Figure 3-5 highlights this pattern. This repetition supports the assumption that we made in Figure 3-3, where we modeled the perforated proof mass as a collection of identical damping surfaces, acting independently of one another. We exploit this repetition to build much smaller FEA models. Figure 3-6 shows a perforated proof mass with 25 holes. Expanded next to this, is a single hole plus its surrounding web material. The proof mass consists of 25 of these 'cells'. The part that we model with finite elements is just one quarter of one cell, which is the area shown meshed in the figure.

The number of elements in the model decreases from many thousands, if a full model were used, to just a few hundred by taking advantage of the symmetry.

The boundary conditions change as indicated in Figure 3-6. Instead of being fixed to zero, the symmetrical boundaries are zero-flux boundaries. To achieve this with ABAQUS, simply do not specify any boundary condition at these nodes.

Recalling the analysis of Section 3.3.3, the damping ratio for the entire proof mass is equal to that of a single quadrant of one cell. So the design procedure is this: First, pick a minimum hole size. Most likely this will be determined by the process. With the hole size set, only the web thickness between holes needs to be determined. We build a model as shown at the top of Figure 3-7 and run it to find the damping ratio. Then we decrease the web thickness until the desired damping ratio is achieved. Finally, we adjust the total proof mass and the total capacitance, by 'connecting' together as many cells as necessary. This last step will not change the damping ratio.

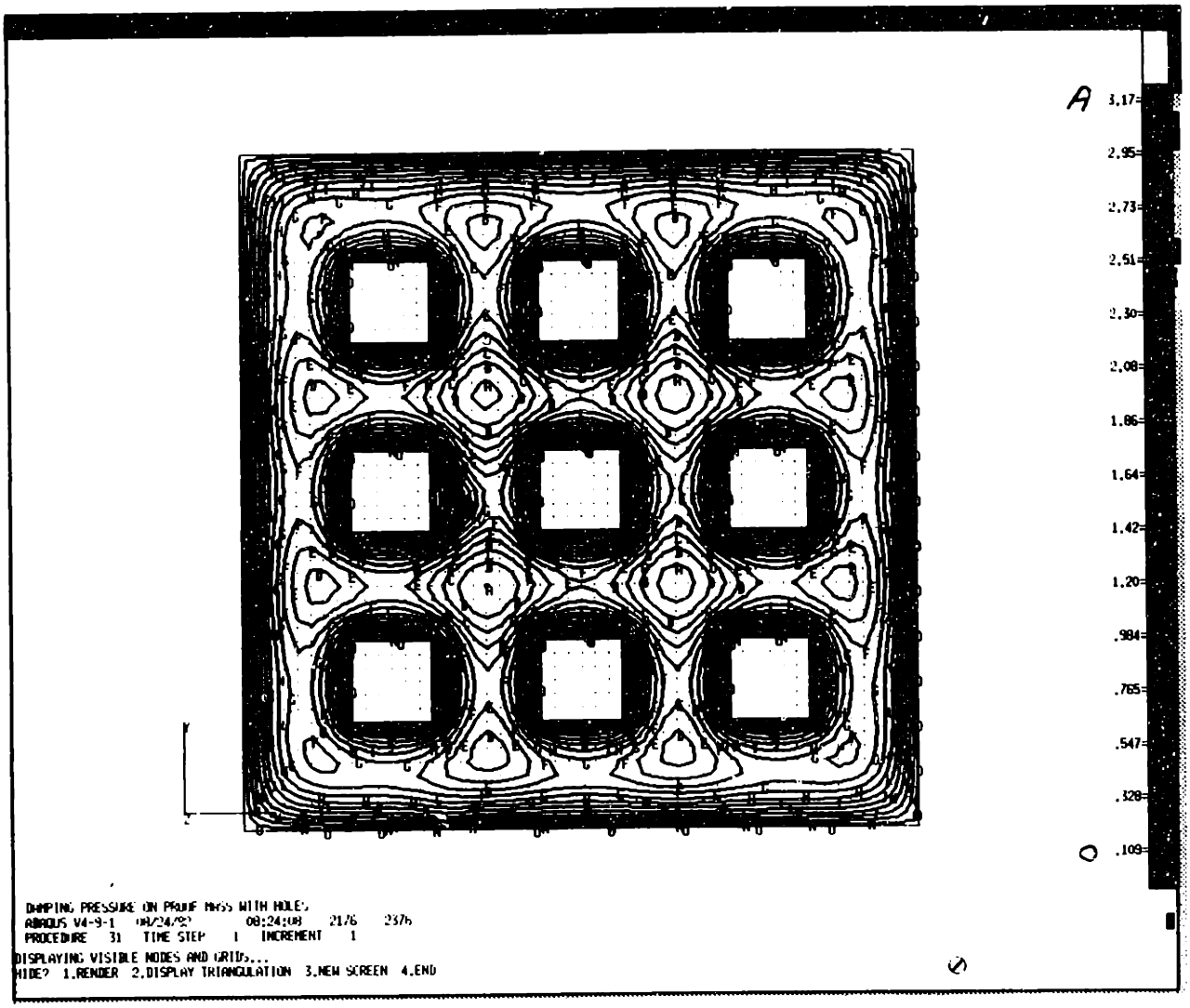

Figure 3-5: A small number of holes does not sufficiently reduce the damping. Also, note the repetitive pattern in the solution.

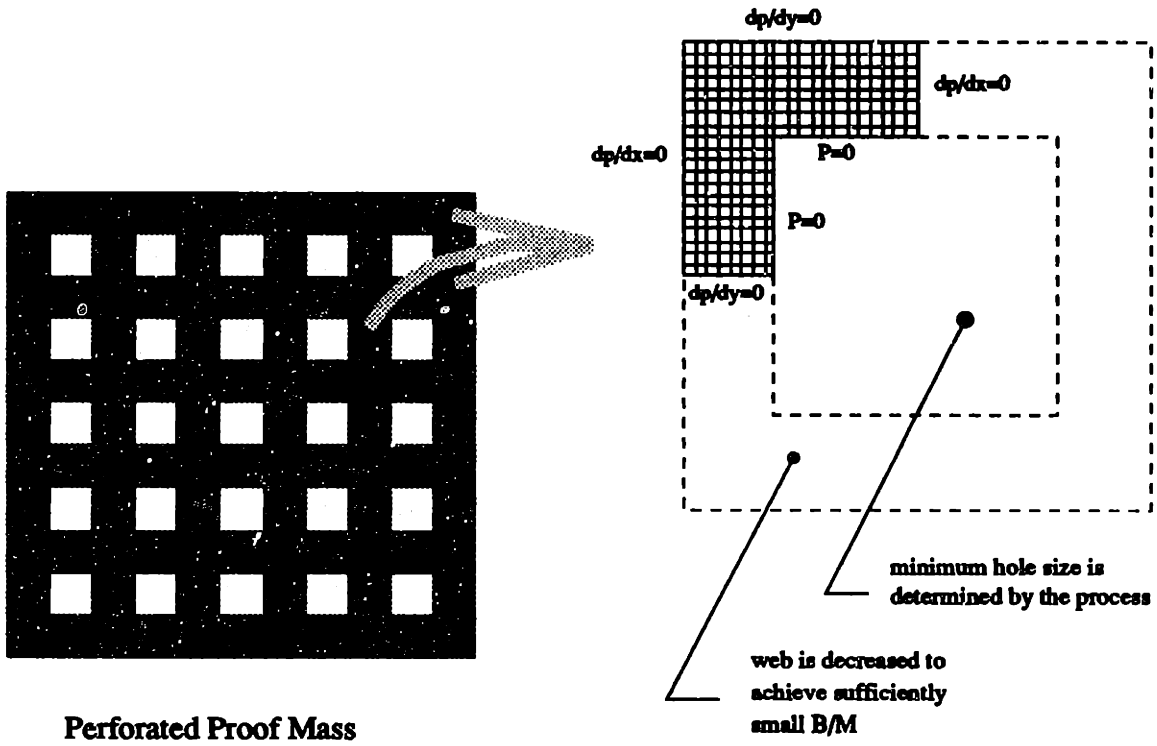

Figure 3-6: The entire perforated proof mass does not need to be modeled; only one quarter of one cell.

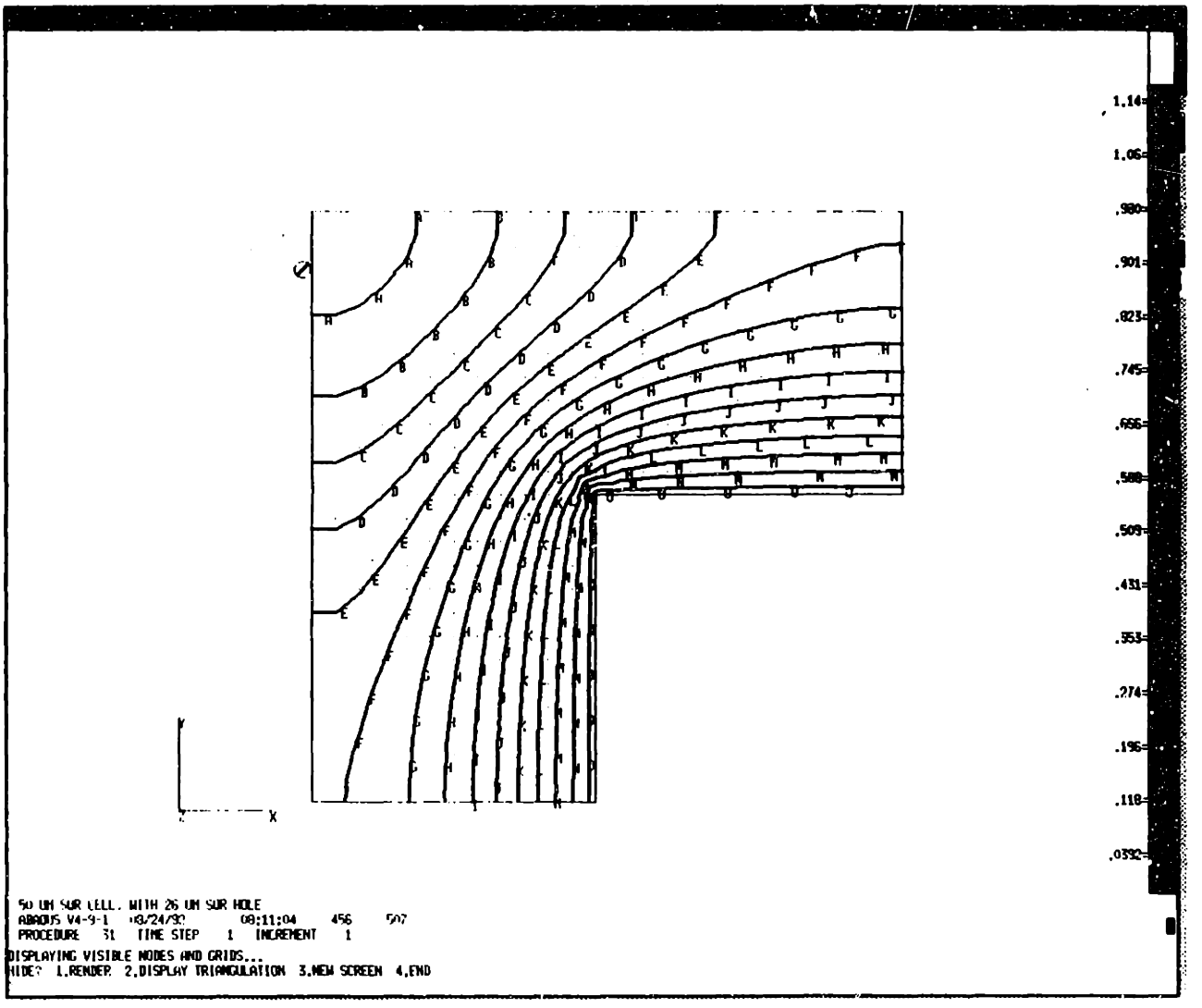

Figure 3-7: Damping pressure on a perforated proof mass. Only the symmetric portion is modeled.

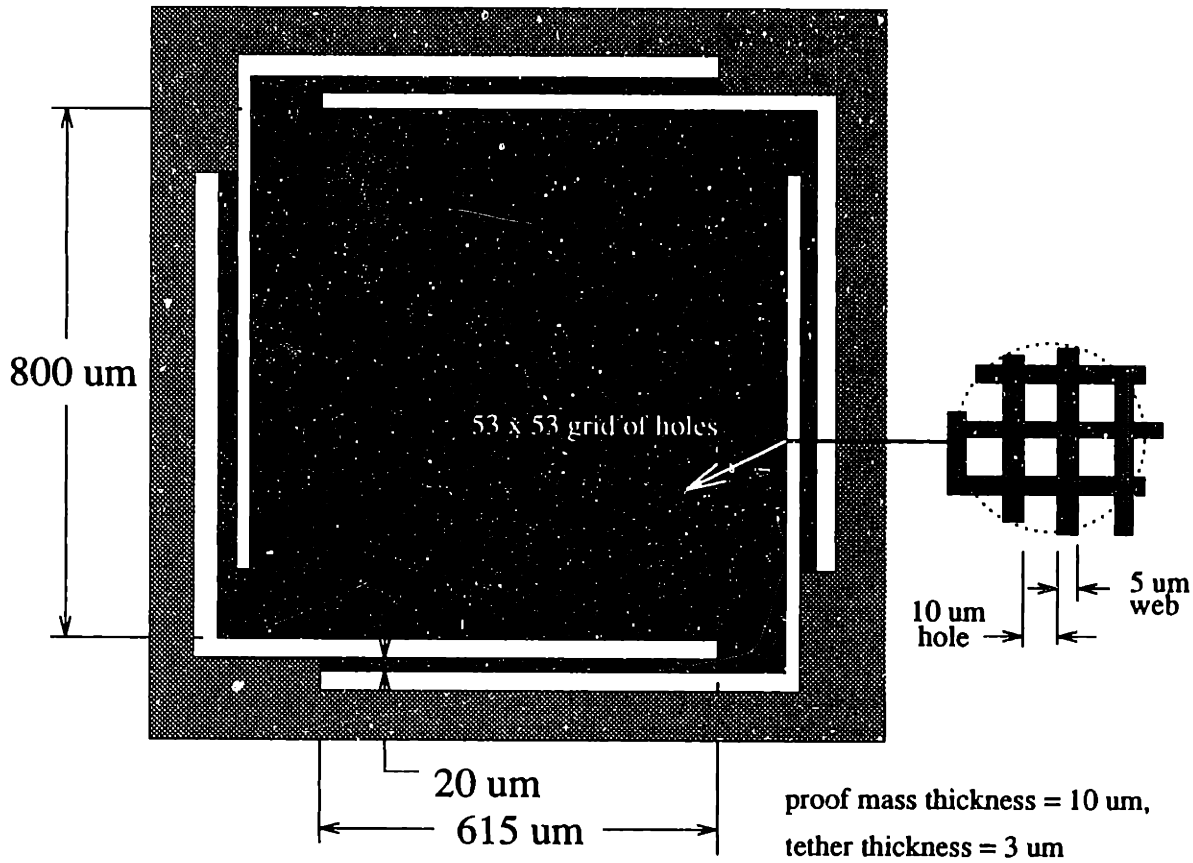

Figure 3-8: A citically damped accelerometer with perforated proof mass.

3.5 A Critically Damped Accelerometer with Perforated Proof Mass

By applying the above design procedure, we lowered the damping ratio of our initial design (Figure 3-1) from about 3282, down to the critical damping ratio, .707. This new design is shown in Figure 3-8. In this design, we used 10 um holes, separated by 5 um webs, and increased the gap dimension from 1 um to 1.5 um. The total proof mass and sense capacitance are the same as they were in Figure 3-1. This capacitance is at least 1.5 pF, and it may be even higher if we were to account for fringing. There are $(53) \cdot (53) = 2809$ perforations.

3.6 Validity of Reynold's Equation

Now that we have solved Reynold's equation, we can check whether the assumptions made in the derivation (Appendix D) were valid for our particular structure. This is especially important because of the unusual dimensions associated with microsensors.

From the contour plot in Figure 3-7, we find that the maximum pressure rise in the gap is ΔP = .419 KPa, or .419 % of the ambient atmospheric pressure in the sensor. This low value is consistent with our assumption of incompressable gas.

We also need to check that the Reynold's number and the Strouhal number are small, so that fluid inertia effects can be ignored. Reynold's number is given by Equation D.4,

$$Re = \frac{\rho V L}{\mu}$$

with the following values,

$$\begin{aligned} \rho &= 1.2 \cdot 10^{-18} \text{ kg}/um^3 \\ V &= 1000 \text{ um/sec} \\ L &= 1.5 \text{ um} \\ \mu &= 1.8 \cdot 10^{-11} \text{ kg/um/s} \end{aligned}$$

this gives,

$$Re = .0001$$

And for the Strouhal number, from Equation D.3,

$$Sr = \frac{VT}{L}$$

where T is the characteristic time. We obtained V by taking the maximum velocity assuming that the proof mass were vibrating at 2000 Hz with .05 um maximum displacement, so we will use 1/2000=.0005 s as the characteristic time. This gives,

$$Sr = .3$$

$$\frac{Re}{Sr} = .0003$$

Since both the $Re \ll 1$ and $Re/Sr \ll 1$, we are justified in ignoring inertia effects.

At small gap dimensions, the boundary condition for the gas velocity at the damping plate surfaces is no longer exactly zero. When the Knudsen number, which is the mean free path of the gas relative to the characteristic gap dimension, exceeds .01, we enter a fluid flow regime where the no-slip condition at solid interfaces is no longer valid. Our gap dimension is 1.5 um, therefore, the Knudsen number is,

$$Kn = \frac{.09}{1.5} = .06$$

Flows with Knudsen number between .01 and .1 can be modeled by the Navier-Stokes equations, but the no-slip condition at the plate surfaces must be replaced by a slip velocity proportional to the wall shear stress [38]. The results of such a model show a reduction in damping pressure due to the low Knudsen number. The effect can be considered as a reduction in the effective viscosity of the fluid due to slip at the boundary. In our case, this is beneficial, in that it reduces the effective damping ratio.

Chapter 4

Prototype Fabrication

4.1 Overview

A significant conclusion from the previous two design chapters, is that thin film processes can be used to produce good accelerometer designs. High sensitivity, stability, linearity, and broad bandwidth, can all be achieved. This chapter describes one method of fabricating such thin film accelerometers. These are made by a single plasma etch through a 5 um thick membrane. The membrane having been formed by wafer bonding and etch back to a boron etch stop. Therefore, the plasma etch defines the tethers and the proof mass at the same time, and they are all 5 um thick. This is shown in Figure 4-1.

Figure 4-2 shows the fabrication sequence, which is fully described in the next section. The mask design is discussed in Section 4.3. Scanning electron micrographs of completed structures are shown in the last section, 4.4.

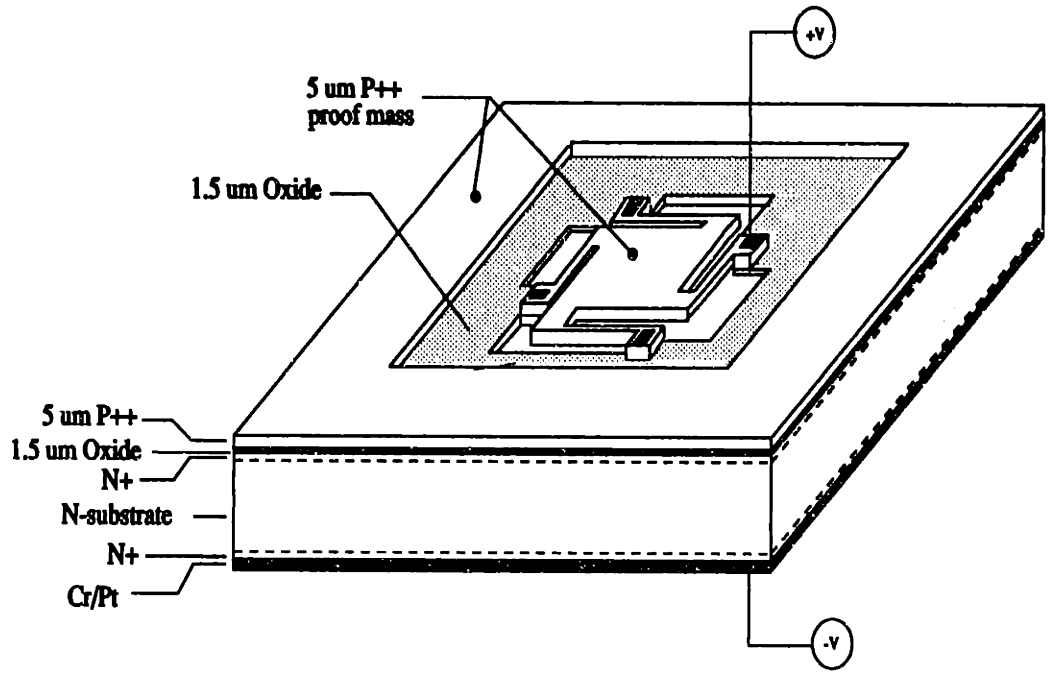

Figure 4-1: Concept for prototype accelerometers. Proof mass and tethers are plasma etched in a 5 um membrane made by wafer bonding and etchback.

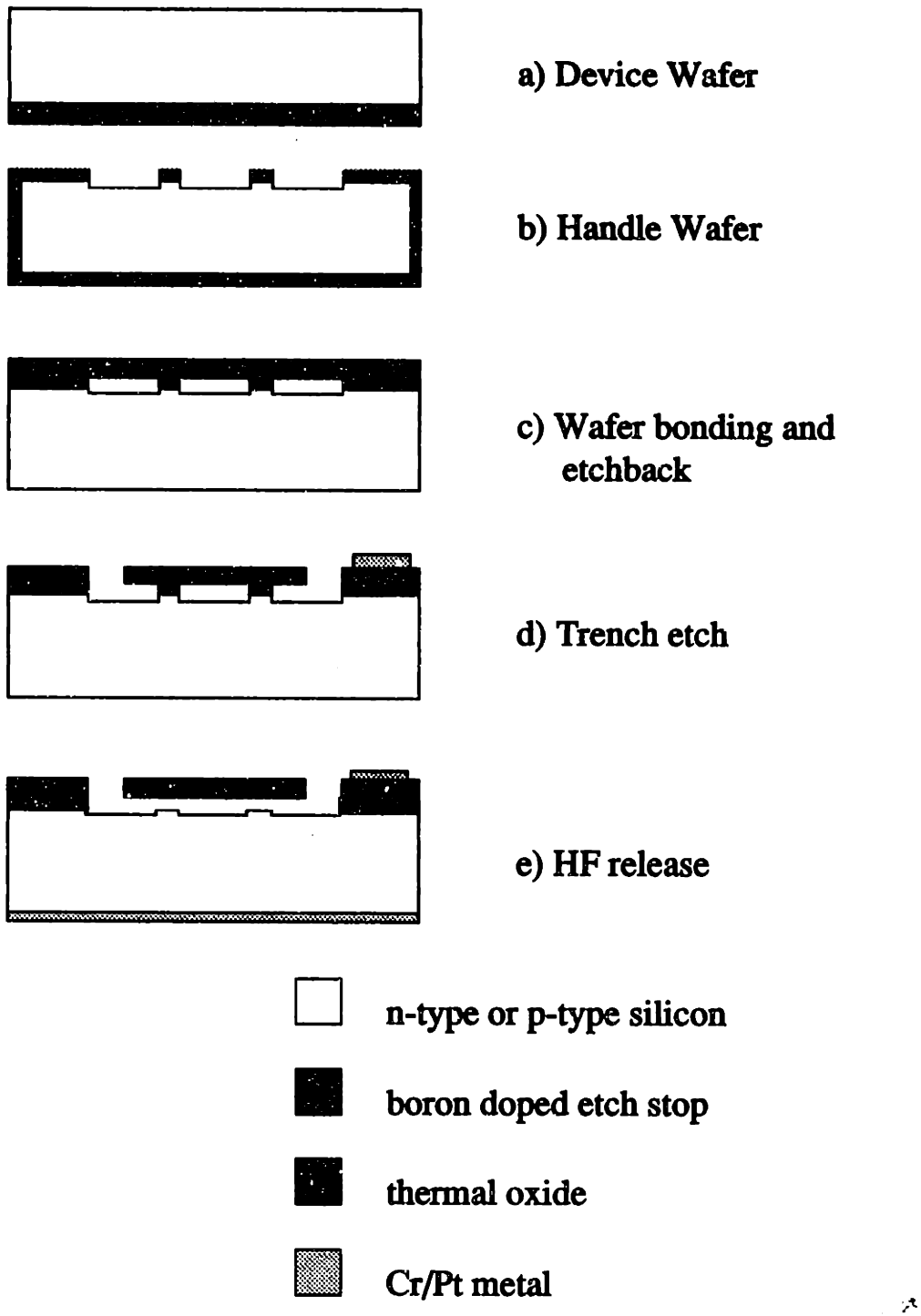

Figure 4-2: Fabrication sequence.

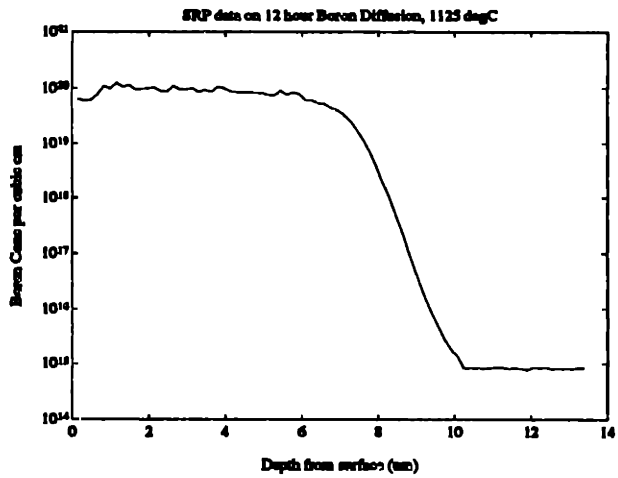

Figure 4-3: Boron concentration versus depth in device wafer. Data taken by spreading resistance technique.

4.2 Fabrication Sequence

4.2.1 Device Wafer

Referring to Figure 4-2 (a), on the device wafer we form a heavily doped boron etch-stop layer. This is done by an 8 hour, solid source boron diffusion, at 1125 $^{\circ}C$. After the diffusion, we remove the deposited boron-nitride glass using BOE. The resulting sheet resistivity is about .8 ohms/square. Figure 4-3 is a plot of the boron concentration versus depth, as measured by the spreading resistance method. Since anisotropic etchants (eg. KOH, CsOH) are stopped by boron concentrations greater than about $5 \cdot 10^{19}$ atoms/cm^3 [39], we would expect, from Figure 4-3, a final membrane thickness of about 6 um.

4.2.2 Handle Wafer

On the other wafer, the handle wafer, we grow 1.5 um of thermal oxide, and then etch openings in the oxide where we want accelerometers. This oxide sets the gap distance, h, between the proof mass and the handle wafer. It also electrically isolates the handle wafer from the tether attachment points. Notice in Figure 4-2 (b), that

after etching through the oxide, we continue to overetch into the silicon to form silicon stubs. These stubs have two functions. One is to support the proof mass, to assure that it survives further processing. The second function is to prevent stiction between the proof mass and the handle wafer during the HF release step, by reducing contact surface area between the two.

We used CF_4 plasma for the oxide etch, and SF_6 for the overetch into the silicon. The relative etch selectivity of thermal oxide to photoresist, in the CF_4 plasma (MTL recipe #20, etcher 2) was between 1.6:1 and 2.4:1. Endpoint detection works extremely well for the oxide etch, because we etch clear through the oxide to the silicon substrate. When processing a small number of wafers, an effective method is to watch the endpoint detector (channel #13 on etcher 2) until it takes a sharp drop down to about 75% of its initial value, allow 10 seconds additional time, then activate the manual endpoint to stop the etch. The SF_6 plasma (MTL recipe #12, etcher 1) etches silicon at a rate of 6590 $\AA$/min. We etch 9 sec to get a 1000 $\AA$ silicon stub. There is no endpoint detection possible for this etch, it is necessarily a timed etch. Since the time is very short, the amount of resist consumed is not of any real concern.

There are also two steps required before growing the handle wafer oxide. First, we have an outside vendor polish the backside of the wafer. This facilitates subsequent alignment steps where we use backside infrared illumination. Second, the wafer is doped with phosphorus to about 5.7 ohms/square. This allows for good ohmic contact when we do the metallization. The doping takes place on both sides of the wafer.

4.2.3 Wafer Bonding

We use high temperature wafer bonding to fuse the device wafer to the handle wafer. To do the bonding, we simply RCA clean both wafers, place them in contact in the same carrier in which they were cleaned, then firmly squeeze the pair together with teflon tweezers. This is followed by one hour in the furnace, at 1000 $^{\circ}C$, with nitrogen.

We were able to obtain nearly void-free bonds, as determined by optical infrared inspection, when the wafers did bond. However, we had difficulty getting the boron doped device wafers to bond to the handle wafers. This problem has been previously

observed by our group [40]. To date, we have not conclusively determined what causes this lack of bonding. One theory is that boron doping causes the wafer to warp, which in turn inhibits bonding. Another is that the weak Van der Waal force that provides the initial bond between the wafers, is somehow diminished by the high boron doping at the surface. A third is that the high boron concentration causes a microscale roughness on the wafer surface that prevents bonding.

This research does not attempt to determine why the bonding with heavily doped boron wafers is inconsistent. However, some empirical observations are worth mentioning. We doped three sets of device wafers, using an 8 hour, 1125 $^{\circ}C$, solid source diffusion. Of the three, all wafers from the first group bonded without difficulty, but none would bond from the second or from the third group. All three groups used the same diffusion recipe, and after each diffusion we stripped the glass with BOE and verified that the wafers de-weted. The surfaces were inspected under a microscope, using Nomarski interference to highlight surface imperfections. Wafers from all three runs looked similar under the Nomarski; they all exhibited a cross-hatched, 'linen', pattern. The boron-nitride solid sources were replaced after the second run, so the third run was with new sources. The sheet resistivities after doping were .80, .90, .70 ohms/square for the first, second, and third runs.

In attempting to bond the wafers, the difference between those that bonded and those that did not, was dramatic and obvious. When they did not bond, it was immediately noticed during the initial contact step. These wafers could easily be separated both before and after the high temperature anneal. On the other hand, boron doped wafers that did bond, appeared to do so with the same ease as blank wafers will normally bond. Also, boron doped wafers that would not bond with patterned handle wafers, also would not bond with un-patterned handle wafers, nor would they bond with blank wafers. All of the bonding runs contained control pairs (blank wafers) that bonded without difficulty.

4.2.4 Wafer Thinning

After bonding, we bulk-thin the wafers in KOH (potassium hydroxide) to remove most of the device wafer, and then do the final thinning, down to the boron etch stop, in CsOH (cesium hydroxide). Figure 4-2 (c) shows the wafers at this stage. The KOH solution is 20% by weight KOH, 80% by weight DI water, at 60 $°C$. This has a reported etch rate of 26.7 um/hr [39]. We do a timed etch, 17 hours, to end up with about 40 um of remaining device wafer.

The CsOH solution is 60% by weight CsOH, and 40% by weight water, at 60 $°C$. We let the CsOH etch until it stops on the boron, as indicated by the lack of reaction bubbles forming at the surface. The CsOH etch rate is about 8 um/hr, but it slows considerably as the etch stop is approached.

The handle wafer is protected from etching by the 1.5 um thermal oxide covering the backside and the edge. However, because the wafer edges are beveled, they do not bond together, and as a result, they are attacked by the etchants. This is shown in the photograph in Figure 4-4. When the edges get attacked, so do the patterned areas near the edge of the handle wafer, creating the holes shown in the photograph. To avoid these holes, which tend to weaken the wafer, it is a good idea not to extend the oxide pattern clear to the edge of the wafer.

4.2.5 Metal Liftoff

At this point we have 5 um membranes bonded over cavities on the handle wafer. Now we want to deposit metal contacts onto where the ends of the tethers will eventually be, as shown in Figure 4-2 (d). We use platinum over chromium because this holds up through our last process step, the HF release etch. We can not apply the metal at a later step, because after the devices are trench-etched, the surface features prevent good photolithography. We use a liftoff process to avoid having to do selective etch removal of the Cr/Pt metal, which is difficult. Also, using the liftoff process makes our photolithography mask clear field, in turn making alignment much easier than if the mask were a darkfield. This is especially important since we use backside infrared

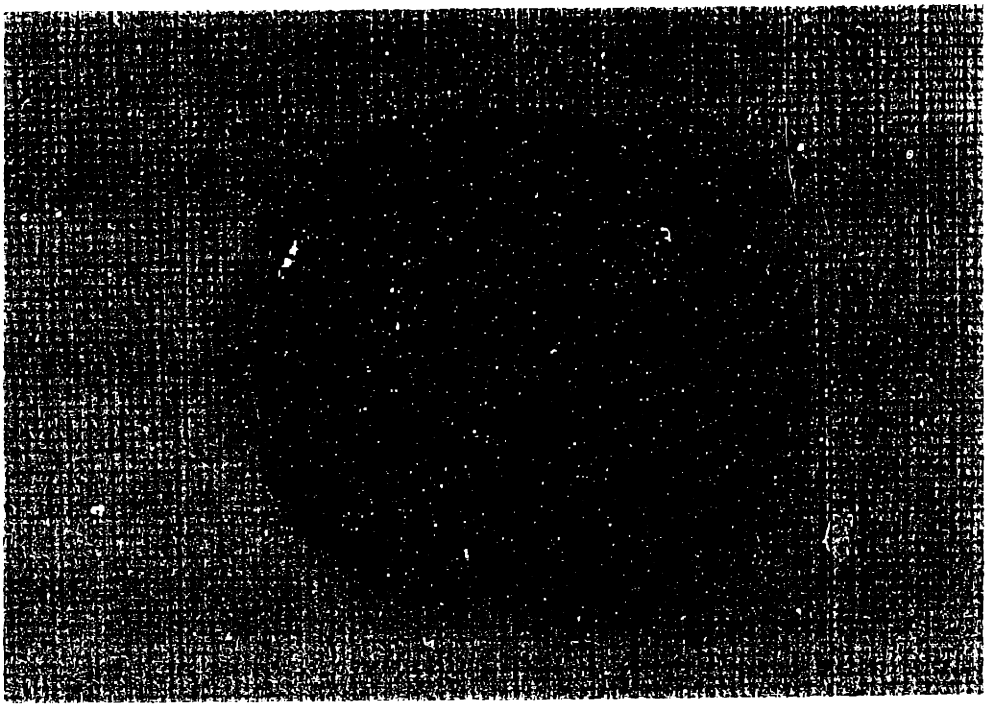

Figure 4-4: Boron etch stop layer after CsOH etch.

illumination for the alignment, which tends to blur the alignment features.

The liftoff process works extremely well, however, one difficulty is mentioned here. Since our contact areas are small, the amount of metal and resist lifted off is quite large. When the actual liftoff is done in acetone, it is hard to prevent small pieces of metal and resist from settling back onto the wafer, which are then very difficult to remove. To avoid this problem, we fill two beakers each with 500 ml of acetone, and a third beaker with 500 ml of methanol. With the wafer held in a single-wafer carrier, we immerse it for 10 seconds in the first beaker of acetone. This removes most of the resist and metal, and if the wafer surface is facing the bottom of the beaker, then most of the material will float to the bottom of the beaker instead of back onto the wafer. After 10 seconds, we then quickly transfer the wafer into the second acetone beaker. After all of the resist has floated off (about 10 minutes), we then quickly transfer the wafer into the methanol, letting it soak here for about 10 minutes. Finally, we remove the wafer and let it air dry.

It was not necessary to use ultrasonics with the acetone to get good liftoff. In fact, ultrasonic agitation destroyed most of our membranes when we did try it. An occasional membrane also broke out due to the vacuum in the electron beam chamber.

This is because the membranes are sealed at one atmosphere, so the differential pressure tends to blow them off of the handle wafer. The only structure that this happened to was a 1200x1200 um membrane, where the total area of the oxide stubs was only 1% of the membrane area. Membranes did not blow out that were 800x800 um squares.

4.2.6 Plasma Trench Etch

This step etches entirely through the membranes, completely forming the proof mass and the tethers. Figure 4-2 (d) shows the proof mass after the trench etch, it is still supported by the oxide stubs. (The tethers are not shown in the figure.)

We use an SF_6 plasma etch, masked with photoresist for the trench etch. The selectivity of silicon to resist with the SF_6 is 3.9:1 (MTL recipe #15, etcher 1). This number represents the slowest silicon etch rate (which occurs at the center of the wafer), relative to the fastest resist etch rate (at the edge of the wafer). Therefore, the thickness of resist needed to etch the membranes, assuming worst case that they are 6 um thick, is,

$$t_{pr} = \frac{6um}{3.9} = 1.5\ um$$

We use a 1.6 um resist mask for this trench etch.

The silicon etch rate depends on the total exposed silicon area. With our particular mask, the silicon etch rate is 2.5 um/min at the wafer edge, and 1.7 um/min at the center of the wafer.

4.2.7 Sensor Release

This final step releases the proof mass by etching out the oxide stubs, as shown in Figure 4-2 (e). But before doing this, we complete the metal contacts by coating the back of the wafer with Cr/Pt, then annealing the entire wafer at 500 $^{\circ}C$ for 30 minutes. Also, we scribe the wafer into individual die before doing the release step.

To release the proof masses, we do a 3 minute etch in 1:1 HF:DI water, followed by 10 minutes of dilution with DI, then 10 minutes dilution with methanol, finishing

with an air dry (no forced air). There is no quick way to determine whether this process is successful or not. Because of the overetch step into the silicon, there are raised stubs that look like oxide stubs, making it very difficult to determine when the oxide has been removed. Even under the SEM, without destroying the devices, we cannot say for sure that they are released.

4.3 Mask Design

This fabrication process requires only three photolithography masks, as shown in Figures 4-5 through 4-7. On each 1 cm die, we place ten different design variations, plus some film stress diagnostics. The die layout is shown in Figure 4-8. Each wafer has almost 60 die sites.

The first mask, Figure 4-5, defines the oxide pattern on the handle wafer. The dark areas are oxide. The oxide stubs on this mask cover about 10% of the proof mass surface area; on other devices, this number is 1%. Notice that there are also oxide stubs supporting the tethers.

The second mask defines the Cr/Pt contacts (Figure 4-6). Note that alignment of this mask would be quite difficult if it were not a clear-field mask as shown.

The third mask is for the trench etch. This particular accelerometer shown has an 800 um x 800 um proof mass, perforated by 10 um holes with 10 um webs. It is supported by long, folded tethers, giving it a sensitivity of 1 um displacement for 20g input acceleration.

Referring to Figure 4-8 for the die layout, we have three rows and four columns of accelerometers. These are arranged with some reason regarding the design variations. Accelerometers in the top row have the following features in common: 800x800x5 um proof mass, perforated by a 53x53 grid of 10x10 um holes with 5 um webs; and the proof mass is supported by oxide stubs covering 1% of the total proof mass area. The designs in the first row are each distinct in that the first from the left does not have any tethers (this is used to indicate success or failure of the proof mass release), the second uses straight tethers and has a 2200 Hz fundamental resonance (20g for 1 um

displacement), the third has an 1100 Hz resonance (5g for 1 um displacemment), and the last accelerometer uses folded tethers and has a 2200 Hz resonance.

In the second row, all of the proof masses are again 800x800x5 um. However, these proof masses are perforated by a 40x40 grid of 10x10 um square holes, separated by 5 um webs. Also, 10% of the proof mass is supported by oxide stubs. The difference between each accelerometer in row 2 is the same as in row 1; the first from the left has no tethers, the second is 2200 Hz, the third is 1100 Hz, and the last is 2200 Hz.

The sense capacitance for all of the devices in rows 1 and 2, is 1.5 pF between the proof and each electrode plate. This is assuming a 1.5 um gap dimension. The two accelerometers in row 3 have four times that capacitance, 6 pF for each electrode plate. These proof masses are 1200x1200 um, perforated with an 80x80 grid of 10 um square holes, separated by 10 um webs. The first accelerometer from the left in row 3 has a resonant frequency of 2200 Hz, and the second is 1100 Hz.

There are also two sets of structures for indicating residual stress in the boron doped membrane. At the center of the third row, are five beams of increasing lengths. These will buckle at film strains between 50 and 250 ppm compressive.

For tensile strains, we have designed the diagnostic structure shown in Figure 4-9. Assuming that the stiff frame shown is under tensile strain, then upon release, it will put the center beam, into compression. We make the stiff frame about 10 times greater in width than the center beam. These structures are located at the bottom left on the die. There are five of these, designed to buckle when the film strain is between 50 and 250 ppm tensile.

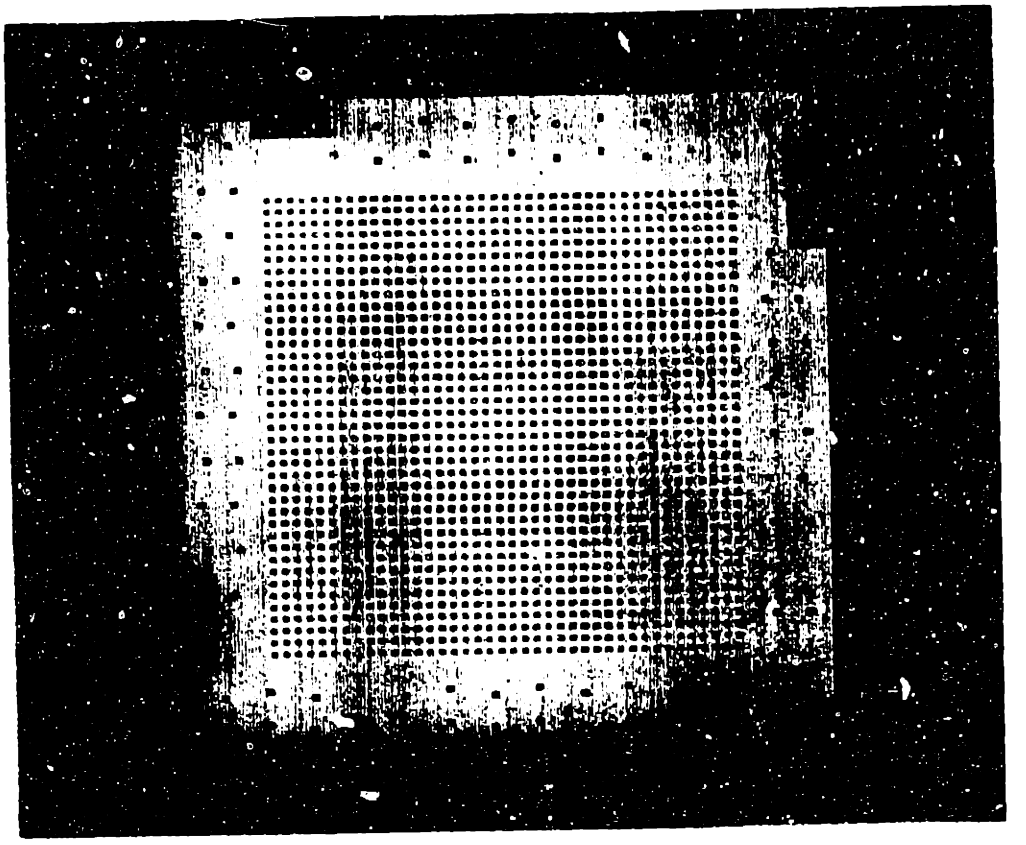

Figure 4-5: Mask # 1: oxide etch.

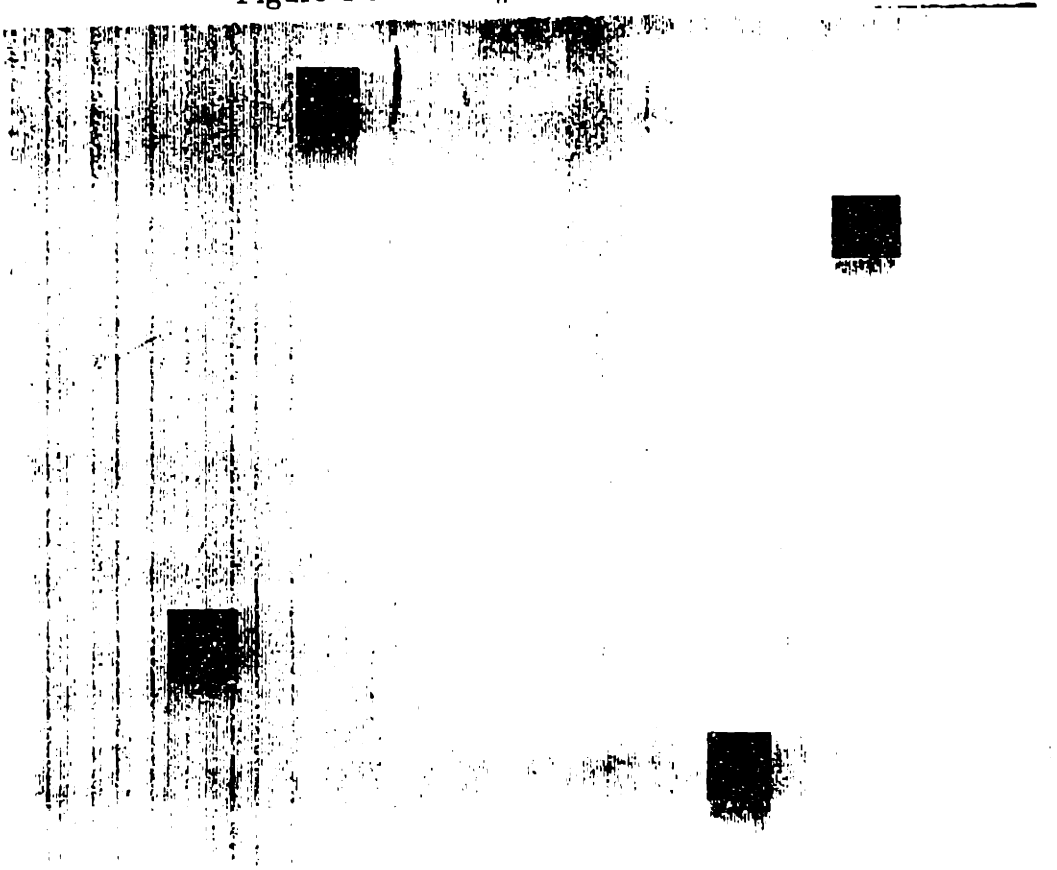

Figure 4-6: Mask # 2: metal contacts.

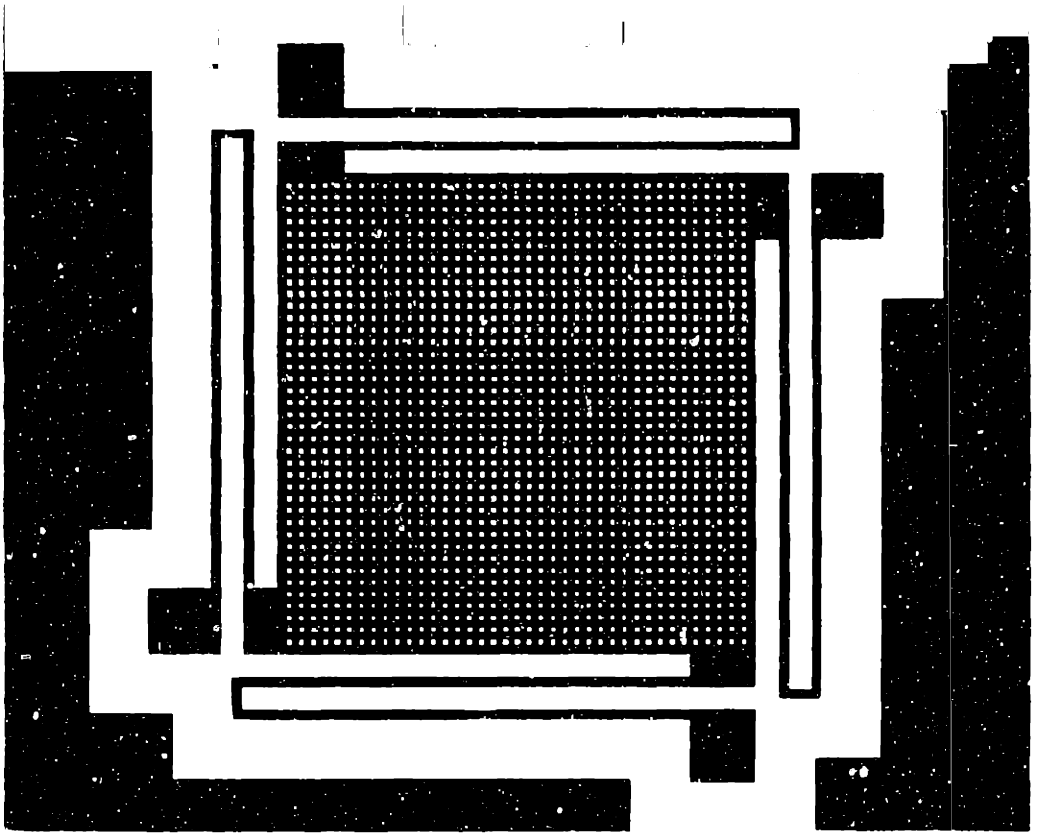

Figure 4-7: Mask # 3: trench etch.

4.4 SEM Photographs

The first four SEM photographs are of the accelerometer from row 2, column 1, of Figure 4-8. They were taken after the trench etch, but before the HF release.

The first two, Figures 4-10 and 4-11, clearly show the folded pinwheel tethers, the perforated proof mass, and the oxide stubs that are still supporting the proof mass.

The third photo, Figure 4-12, shows a tether and its attachment to the field oxide. The Cr/Pt contact is the light material on top of the tether.

The last photo, Figure 4-13, clearly shows an oxide stub supporting the folded tether. Under the oxide stub is the overetch step into the silicon. We can measure some dimensions from this photo, since we know it was taken at an angle of 60 degrees, and magnification of 4000.

- 1.5 um oxide thickness
- 5.2 um tether thickness
- 11.8 um tether width at bottom

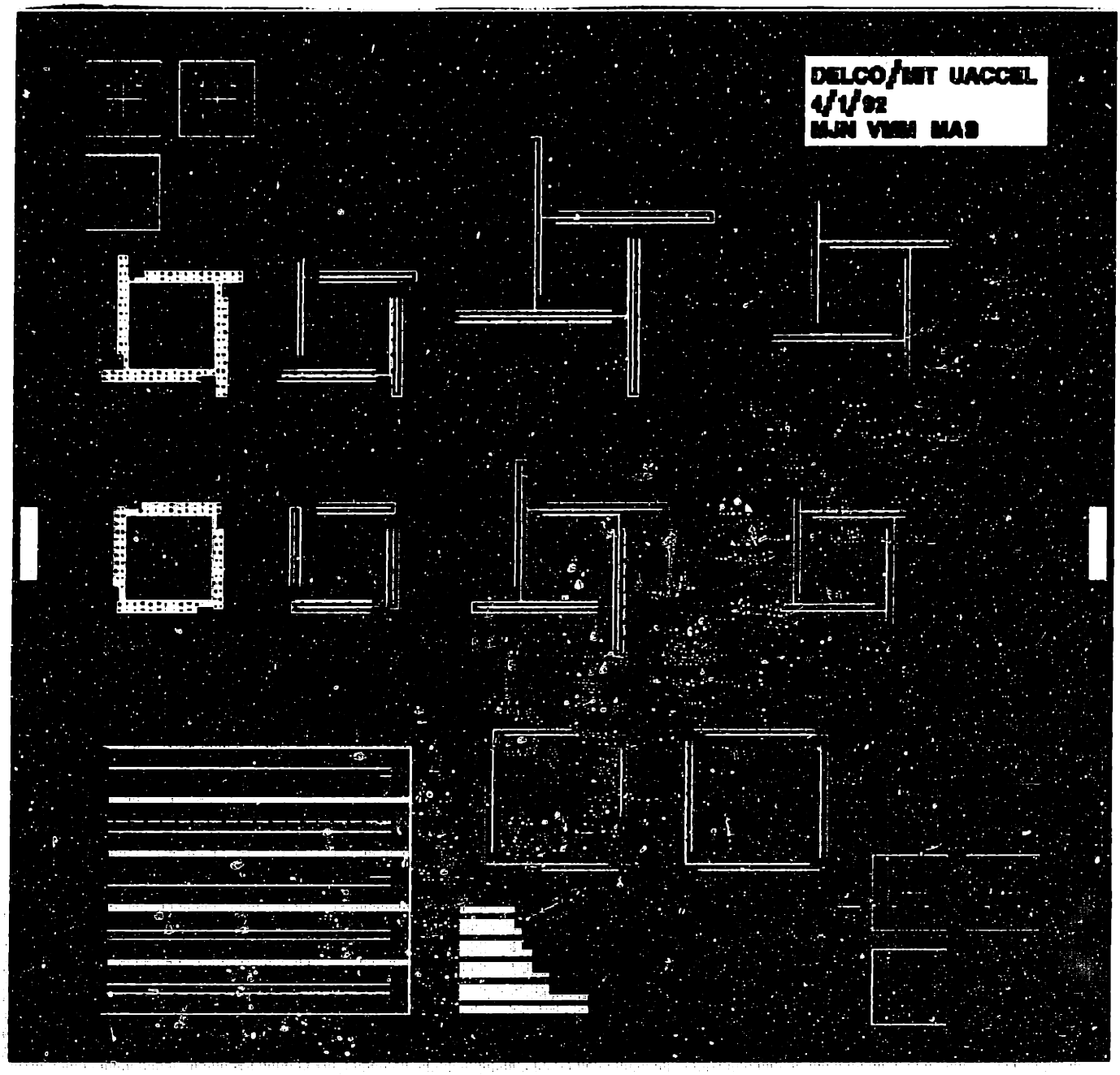

Figure 4-8: Die layout.

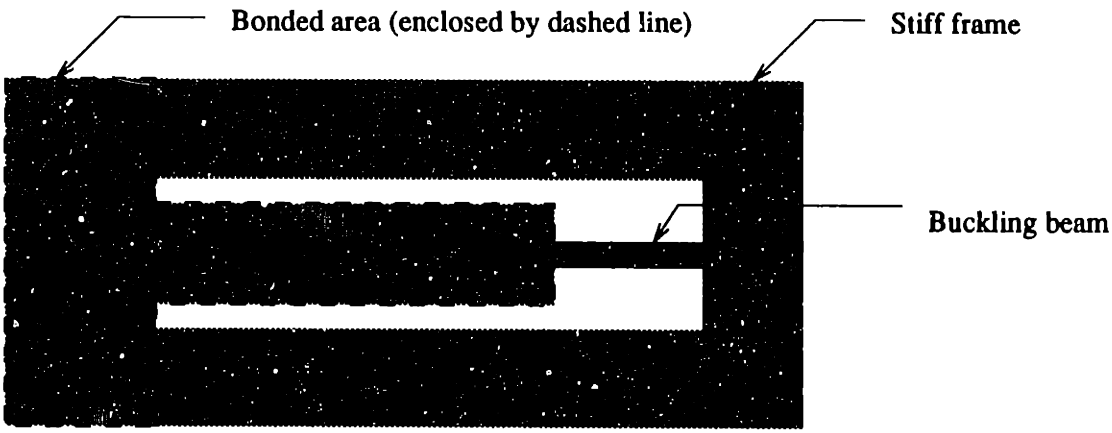

Figure 4-9: Diagnostic structure for indication of thin film tensile stress.

- 9.0 um tether width at top

Dektak measurements showed 1.43 um for the oxide thickness, and 5.03 um for the tether thickness. The tether design thickness was 5 um. The width measurements on the tethers, verify the anisotropic nature of the SF_6 etch; we undercut the tethers by $11.8 - 9.0 = 2.8$ um, for a 5.2 um deep etch. (We estimate the accuracy of measurements from photos at about $\pm .05$ um).

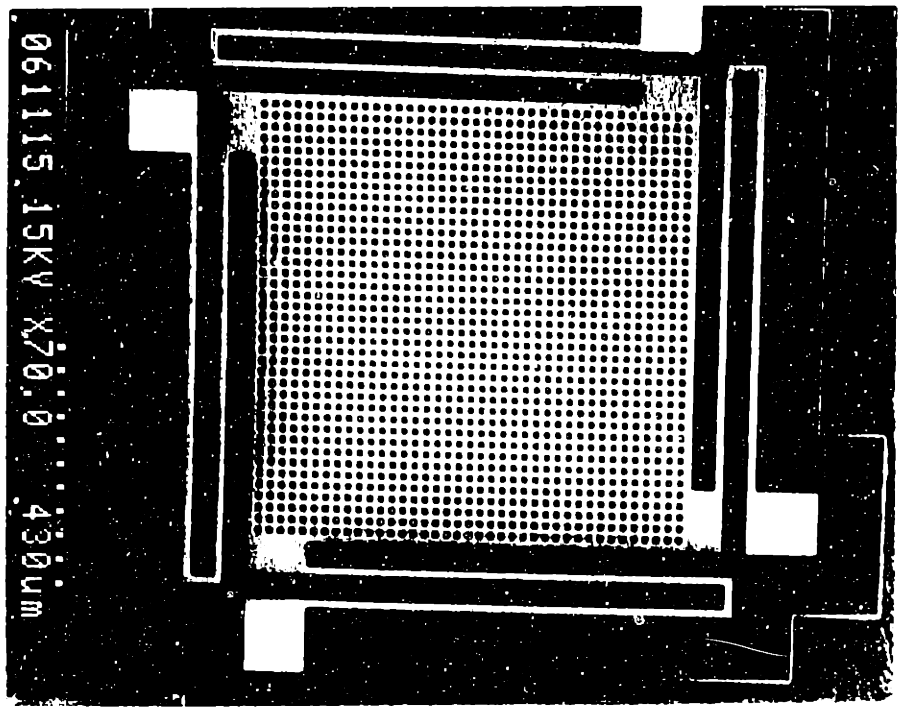

Figure 4-10: Top view of accelerometer structure. This shows the perforated proof mass supported by folded pinwheel tethers.

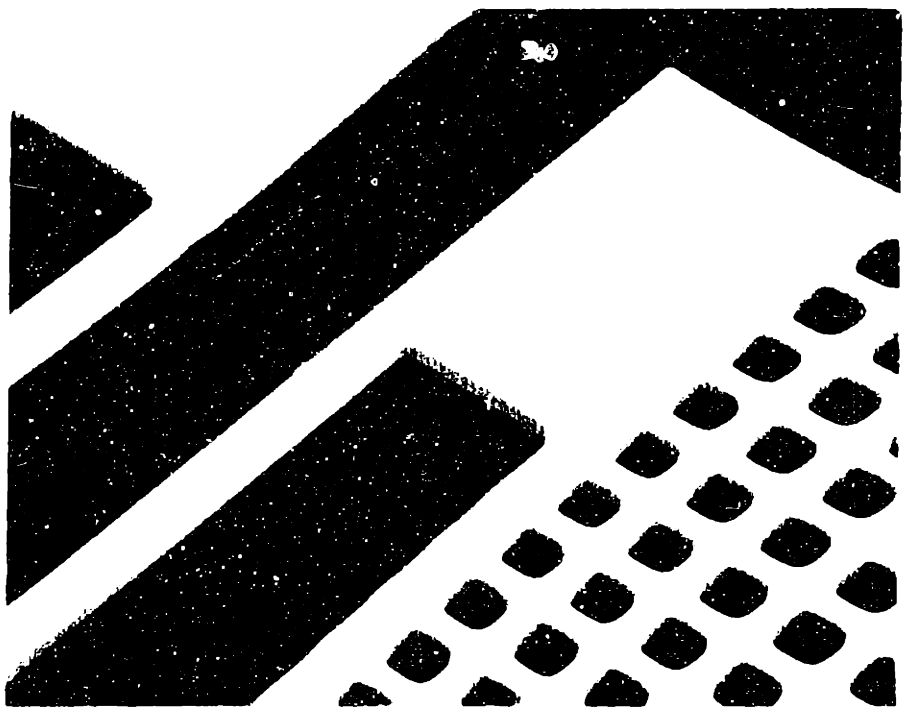

Figure 4-11: A closer view of the proof mass with perforations. Oxide support stubs visible under proof mass.

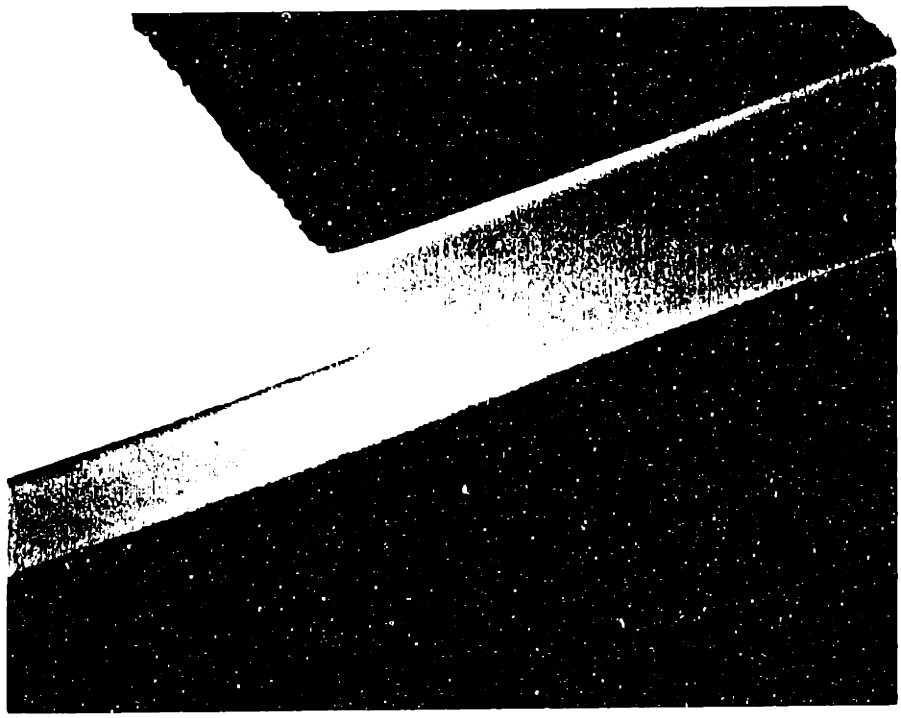

Figure 4-12: A tether and its attachment to the field oxide. The lighter area is a Cr/Pt contact.

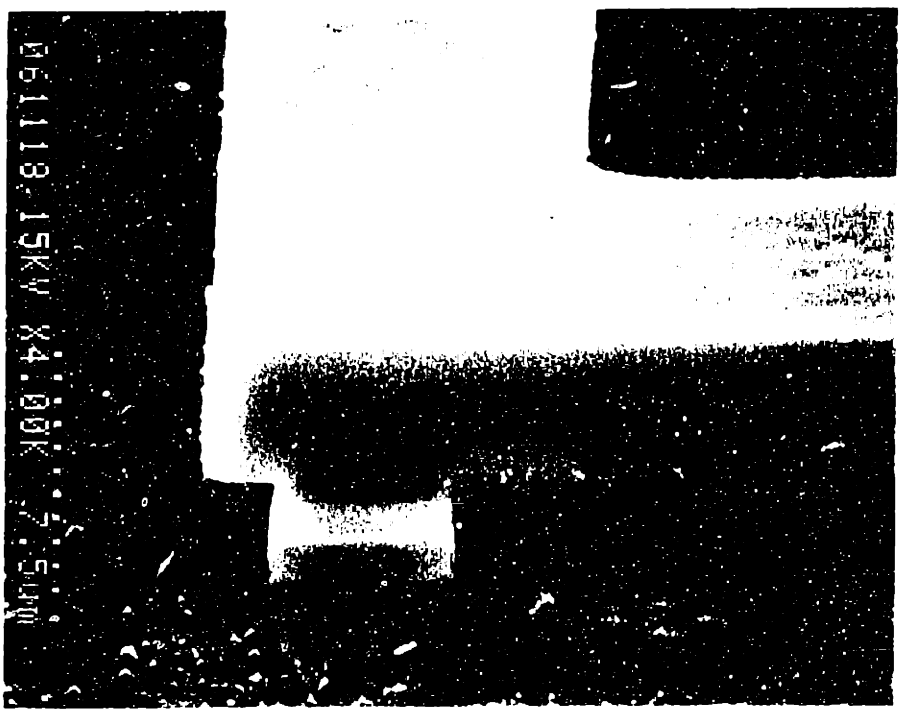

Figure 4-13: The corner of a folded tether. It is still supported by an oxide stub.

Chapter 5

Accelerometer Tests

Approximately eight of the accelerometers were packaged, wirebonded, and tested. All of these devices could be moved by probe tips, and exhibited remarkable strength in that the proof masses could be lifted at least 50 um without breaking the tethers or breaking the bond to the handle wafer. One device, #3, gave reasonable results when tested on our dynamic shaker, and #3 also showed pull-in behavior when a DC bias voltage was applied across the electrode plates. This section reports on these results and compares them to our theoretical predictions.

5.1 Packaging and Interconnects

The test samples that we worked with were the 1 cm x 1 cm die as shown in Figure 4-8. Each die has eight different accelerometers, plus the film stress diagnostic structures. We mounted these with epoxy into 1 in x 1 in ceramic packages. Probes were used to verify electrical isolation between the proof mass bonding pads and the handle wafer. If the devices passed the probe test, then we wirebonded them with .001 in. diameter aluminum wire in a wedgebonder. One wirebond was made from each device to a package lead, and another bond was made from the handle wafer to a package lead. The wire lengths were about 1 cm.

The accelerometers that we tested had a slightly different process sequence than that described in Section 4.2. The final release step with HF acid also removed the

Cr/Pt metal contacts. This happened because the 500 $\AA$ Cr layer was too thick, so that the HF was able to get under the Pt and quickly etch away the Cr. To salvage these devices, we removed all of the metal with aqua regia before doing the HF release. After the HF release, we evaporated 100 $\AA$ of aluminum over the entire die, and then sintered the aluminum at 470 $°C$. The aluminum coating was not enough to electrically short the devices to the handle wafer, but it was enough to allow ohmic contact to be made to the handle wafer. We had tried to make ohmic contact without the aluminum coat, directly to the silicon; and as expected, ohmic contact was made to the P+ doped devices, but not to the N+ doped handle wafer.

In addition to verifying electrical isolation, we used the probes to check that the proof masses were detached from the underlying oxide stubs. We could bring a probe down into contact with a proof mass, and then push the proof mass laterally about 20 um without breaking it. Also, we could work probes underneath the proof mass, and then pull the proof mass away from the handle wafer. In most cases this was a necessity in order to separate the proof mass from the handle wafer, since they were usually stuck together.

Wirebonding to the tether pads was difficult, but not impossible. One of these bonds is shown in the photograph in Figure 5-1. The difficult part is centering the bond on the pad, so that the bond does not extend over the pad and short the device to the handle wafer. The bonding pads are 80x80 um, which is intentionally small to minimize stray capacitance. Breaking of the tethers due to the bonding force was not a problem. We also tried using a ball bonder with .001 in gold wire, but the ball was too large for the pads.

5.2 Capacitance Measurements

5.2.1 Procedure

We verified that the sensing capacitance, which is the capacitance between the proof mass and the handle wafer, is close to our design value. To make the measurements,

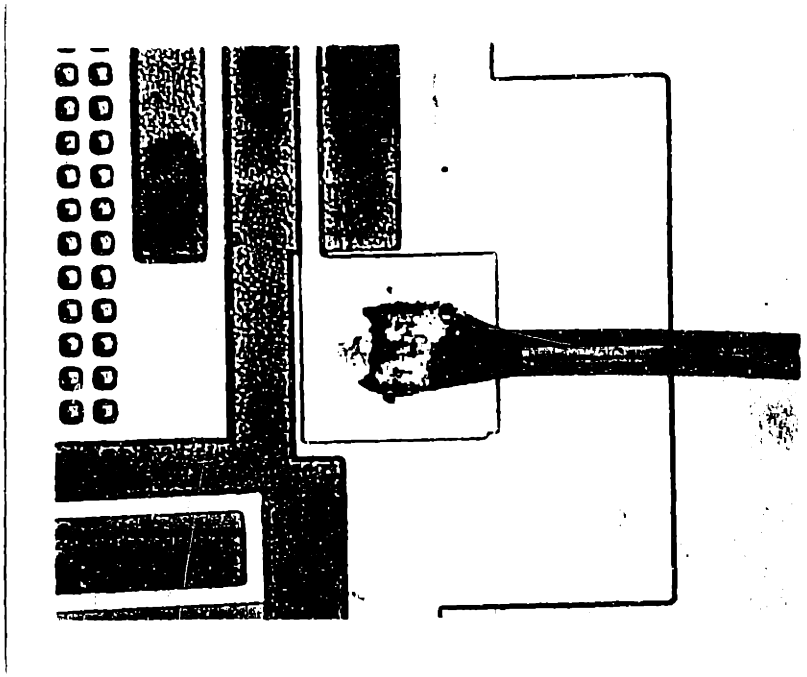

Figure 5-1: Photograph of aluminum wirebond to 80x80 um tether pad.

we used an HP 4280A capacitance meter. The HP 4280A uses a 1 MHz, 30 mV test signal, to measure capacitance with resolution down to 1 fF, and absolute accuracy of .1% of full scale range. The most sensitive range setting is 10 pF full scale. It can apply a bias voltage to make capacitance vs. voltage (C-V) measurements, and it can take capacitance vs. time (C-t) measurements at sampling speeds as fast as 10 ms per sample.

A schematic of the test setup is shown in Figure 5-2. The ceramic package containing the test die is taped to a 4 in x 2 in piece of circuit breadboard. Wires are soldered between the ceramic package and banana jacks installed in the breadboard. From the banana jacks we convert to BNC connectors and use about 3 ft. of shielded connector over to the HP 4280A.

We calibrated the device to remove stray capacitance from the shielded cables back into the HP 4280A. Therefore, our capacitance measurements represent the combined capacitance of the devices under test, the leads on the ceramic package, and the wirebonds from the ceramic package to the die.

5.2.2 Results

Device #3 had the following measured and design capacitance:

measured capacitance	:	3.5 pF
design capacitance	:	1.9 pF

5.2.3 Discussion

Two non-ideal factors are affecting the capacitance value that could explain why the measured value does not agree with the design value. The first of these is the stray capacitance. This is the capacitance between the leads on the ceramic package, and between the aluminum wires from the leads to the die. The stray capacitances are in parallel with the sense capacitance, thus they increase the measured value.

The second factor is any warping of the proof mass. This could be caused by nonuniform stresses through the thickness of the proof mass, as might be caused by the thin aluminum coating used for contacts, or by nonuniform boron doping. Warping can lead to either increased or decreased sense capacitance, depending on the direction of the bend.

5.3 Capacitance versus Bias Voltage

5.3.1 Procedure

By applying a DC bias voltage between the proof mass and the handle wafer, we can move the proof mass to simulate an input acceleration. The electrostatic force created by the bias voltage is reacted by the tethers, resulting in an equilibrium displacement. At some voltage, called the pull-in voltage, the electromechanical system becomes unstable; the electrostatic force overcomes the tether force, and the proof mass deflects until it contacts the handle wafer [41]. The test setup is the same as for the capacitance measurements, since the HP 4280A is capable of applying a DC bias voltage.

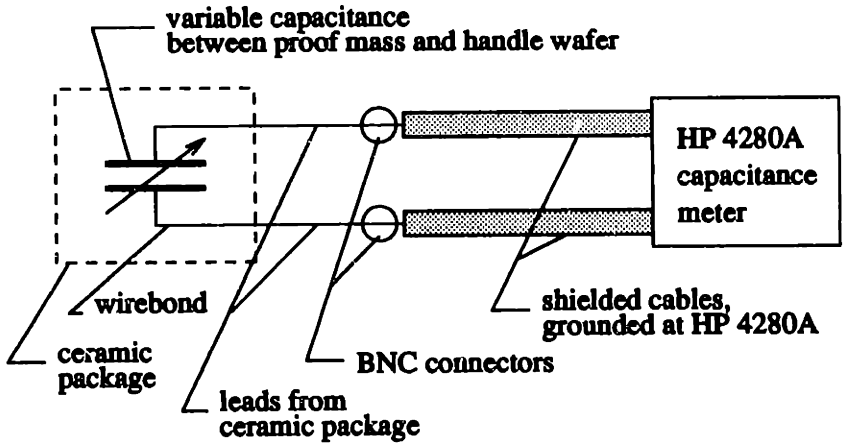

Figure 5-2: Schematic of test setup for capacitance measurements.

5.3.2 Results

Figure 5-3 shows the C-V data for accelerometer #3. The pull in voltage is apparent at about 11 V.

5.3.3 Discussion

The effect is symmetrical for either positive or negative voltages, as expected. However, 11 V for pull-in is substantially higher than the theoretical value. To calculate the theoretical pull-in voltage, we use the results from [41]. The pull-in voltage, V_p, for two parallel capacitor plates, is given by,

$$V_p = \sqrt{\frac{8}{27}\frac{h^3 k}{\epsilon_0 A}} \tag{5.1}$$

where the variables are,

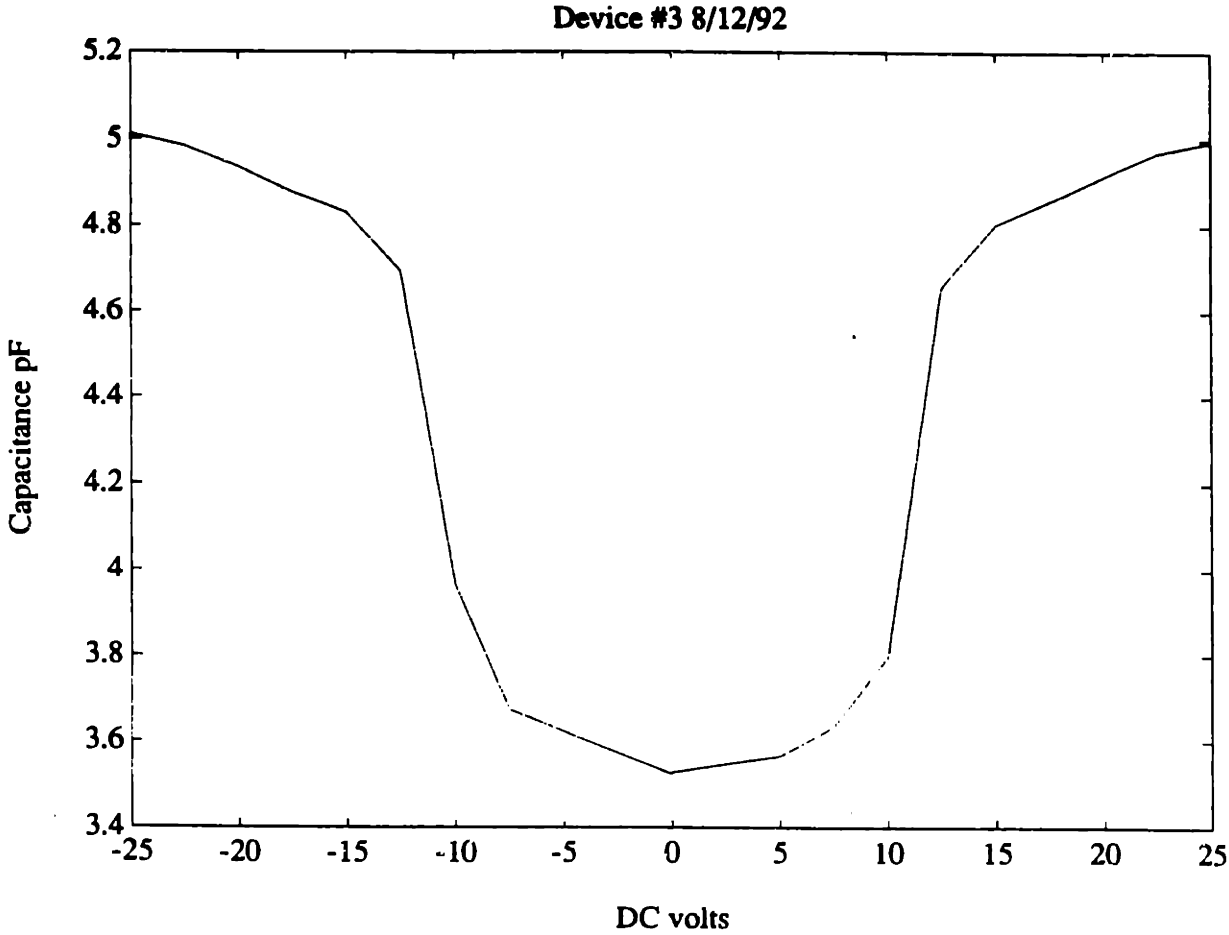

Figure 5-3: Capacitance vs. bias voltage. Indicating movement of the proof mass.

V_p = pull-in voltage between the proof mass and the handle wafer

k = tether spring constant

h = gap between proof mass and handle wafer

ϵ_0 = permittivity of air

A = capacitor plate area

The design values for accelerometer #3 are:

$$h = 1.5 \cdot 10^{-6} \text{ M}$$
$$k = 1.05 \text{ N/M}$$
$$A = .48 \cdot 10^{-6} M^2$$
$$\epsilon_0 = 8.85 \cdot 10^{-12} \text{ F/M}$$

Using these values in Equation 5.1,

$$V_p = .50V$$

Figure 5-3 shows pull-in at about 11 volts We suspect that the gap thickness must be substantially larger than 1.5 um to explain the difference between the measured and theoretical V_p. Also, we know that K is less than 1.05 N/M because of the lateral etching of the tethers. From Section 4.4 we know that the average tether width, because of lateral etching, is (9+11.8)/2=10.4 um instead of 11.8 um. This reduces the tether stiffness, k from 1.05 to,

$$k = (1.05N/M)\frac{10.4}{11.8} = .93N/M$$

Using the measured value of 11 volts for the pull-in, and k=.93 N/M, we calculate (by rearanging Equation 5.1 the apparent gap spacing to be,

$$h = V_p^{2/3}\left[\frac{27}{8}\frac{\epsilon_0 A}{k}\right]^{1/3}$$

$$h = 12um$$

5.4 Vibration Test

5.4.1 Procedure

We constructed a vibration test system (Figure 5-4) using a Ling Dynamics shaker, capable of 100 lb maximum vibrating force, at frequencies from DC to 7500 Hz. The maximum acceleration is 117g. The test accelerometer's output is calibrated against a Bruel and Kjaer 4383 reference accelerometer, also mounted on the vibrator. The 4383 has a calibration accuracy of $\pm 2\%$, transverse sensitivity of .6%, and the amplitude response deviates no more than 10% over the range from .1 Hz to 4 KHz.

We measured the change in capacitance of the test accelerometer using the HP 4280A C-V meter. By running this in C-t mode, we captured dynamic capacitance changes at a 100 Hz rate. Then, using fourier transform of a 256 point sample, we calculated the test accelerometer's magnitude response when excited by the shaker. Because of the high sampling rate in C-t mode, the HP 4280A can resolve only .05 pF changes when in C-t mode. This limits the minimum acceleration level detectable by our vibration test.

5.4.2 Results

We verified that stray capacitance was not a problem, even with the shaker turned on. This was determined by tests made on a device that had the proof mass stuck down to the handle wafer. Because the proof mass was stuck, the sensor contributed no changes to the capacitance, so any output could only be due to changes in stray capacitance or other test system noise. We found that the maximum capacitance change on the stuck accelerometer was less than the .05 pF minimum detectable capacitance.

Two examples of the FFT results are shown in Figure 5-5 and 5-6. On the y-axis is plotted the change in capacitance, and the x-axis is the FFT frequency. We see that in both cases the frequency of the accelerometer response matches the frequency of the input acceleration, which is 33 Hz in Figure 5-5, and 43 Hz in Figure 5-6.

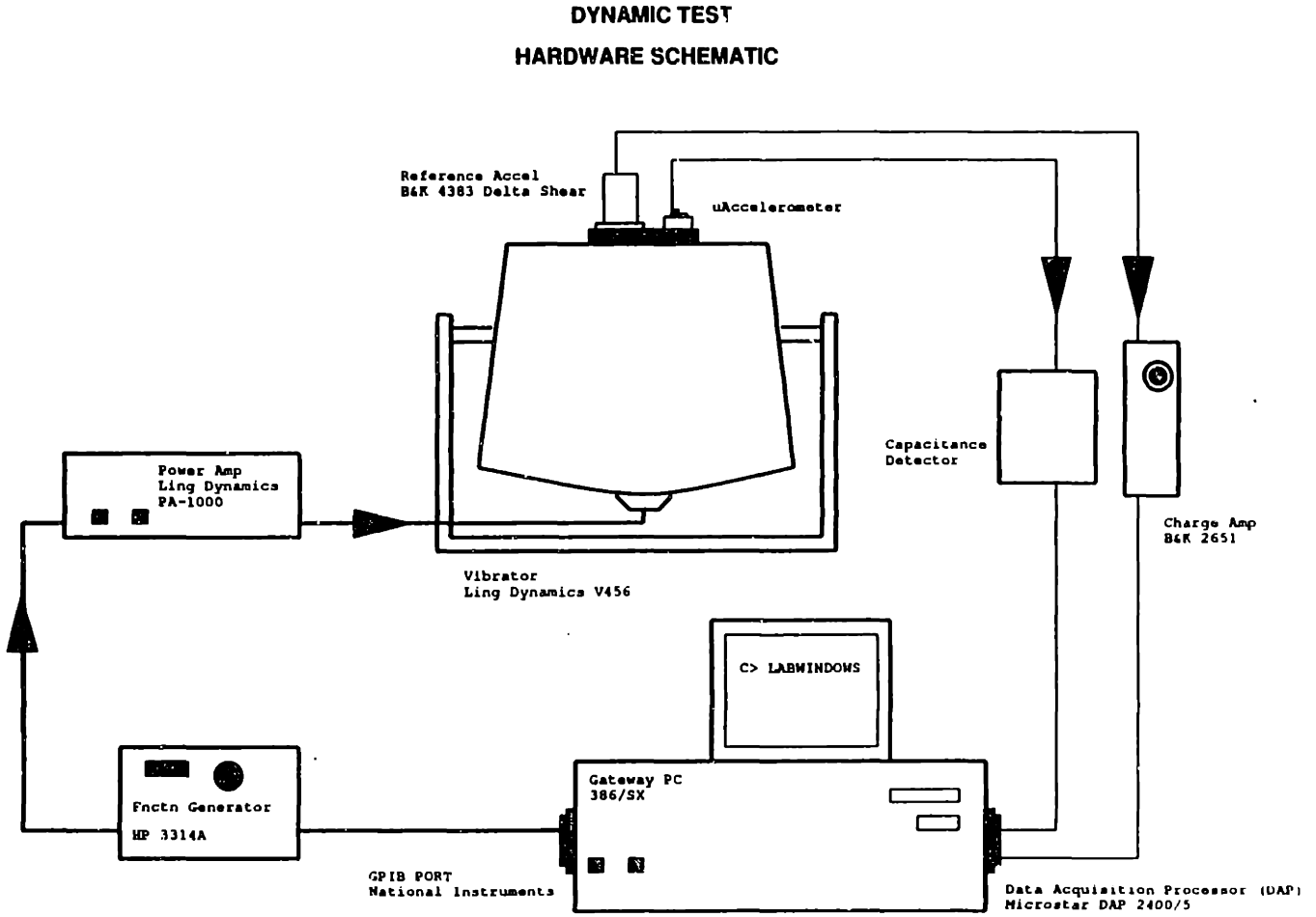

Figure 5-4: Vibration test system.

By taking the 256 point FFT at a number of different input acceleration magnitudes, while holding the frequency constant; and then plotting the peak magnitude from the FFT's, we obtained the results shown in Figure 5-7. This shows the change in capacitance of the accelerometer under test, as taken from the FFT, versus the reference input acceleration as indicated by the B&K reference accelerometer mounted on the shaker. We performed this test at two frequencies as shown; one at 33 Hz and another at 43 Hz.

5.4.3 Discussion

We can compare the measured sensitivity shown in Figure 5-7 to the theoretical sensitivity. The theoretical sensitivity is derived as follows.

From Equation 2.3, we know that

$$\delta = \frac{M}{k}a \tag{5.2}$$

where,

$$\begin{aligned} \delta &= \text{proof mass displacement} \\ M &= \text{proof mass} \\ k &= \text{tether stiffness} \\ a &= \text{input acceleration} \end{aligned}$$

If the gap dimension is h_1 when $a = 0$, and h_2 for $a \neq 0$, then

$$\delta = h_1 - h_2 \tag{5.3}$$

and if the sense capacitance is C_1 when $a = 0$, and C_2 for $a \neq 0$, then

$$C_2 = C_1 \frac{h_1}{h_2} \tag{5.4}$$

Combining these last three equations to solve for the change in capacitance, $\Delta C =$

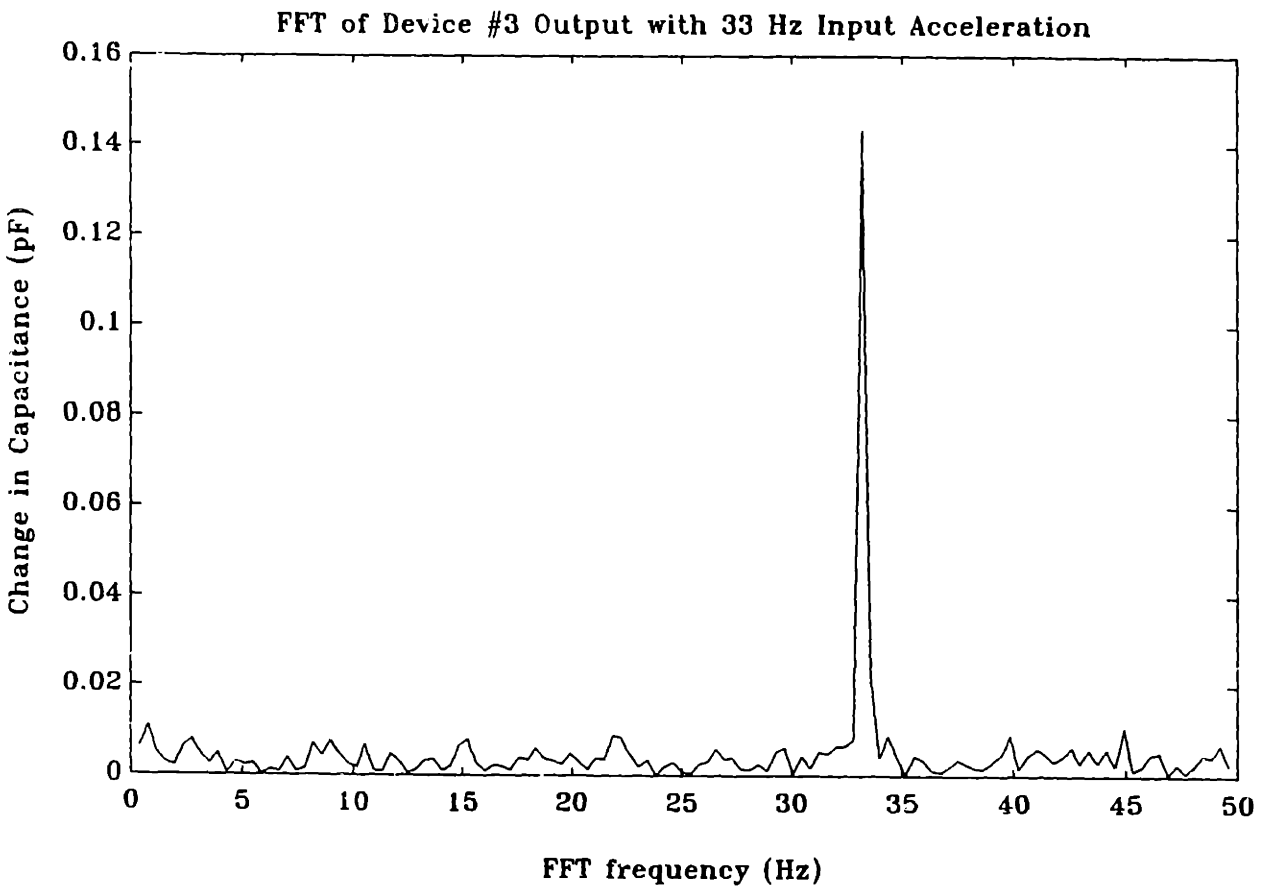

Figure 5-5: Response of the accelerometer to 33 Hz vibration input.

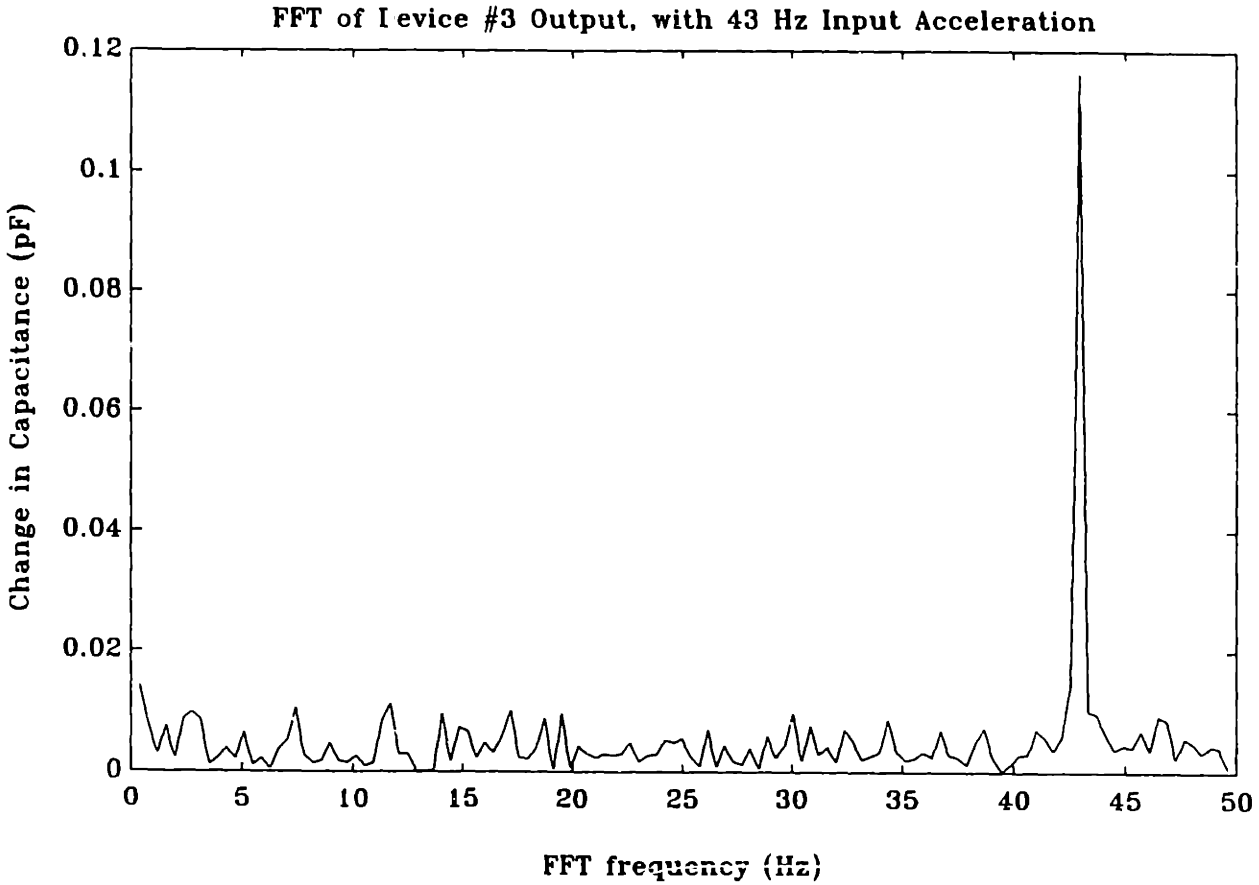

Figure 5-6: Response of the accelerometer to 43 Hz vibration input.

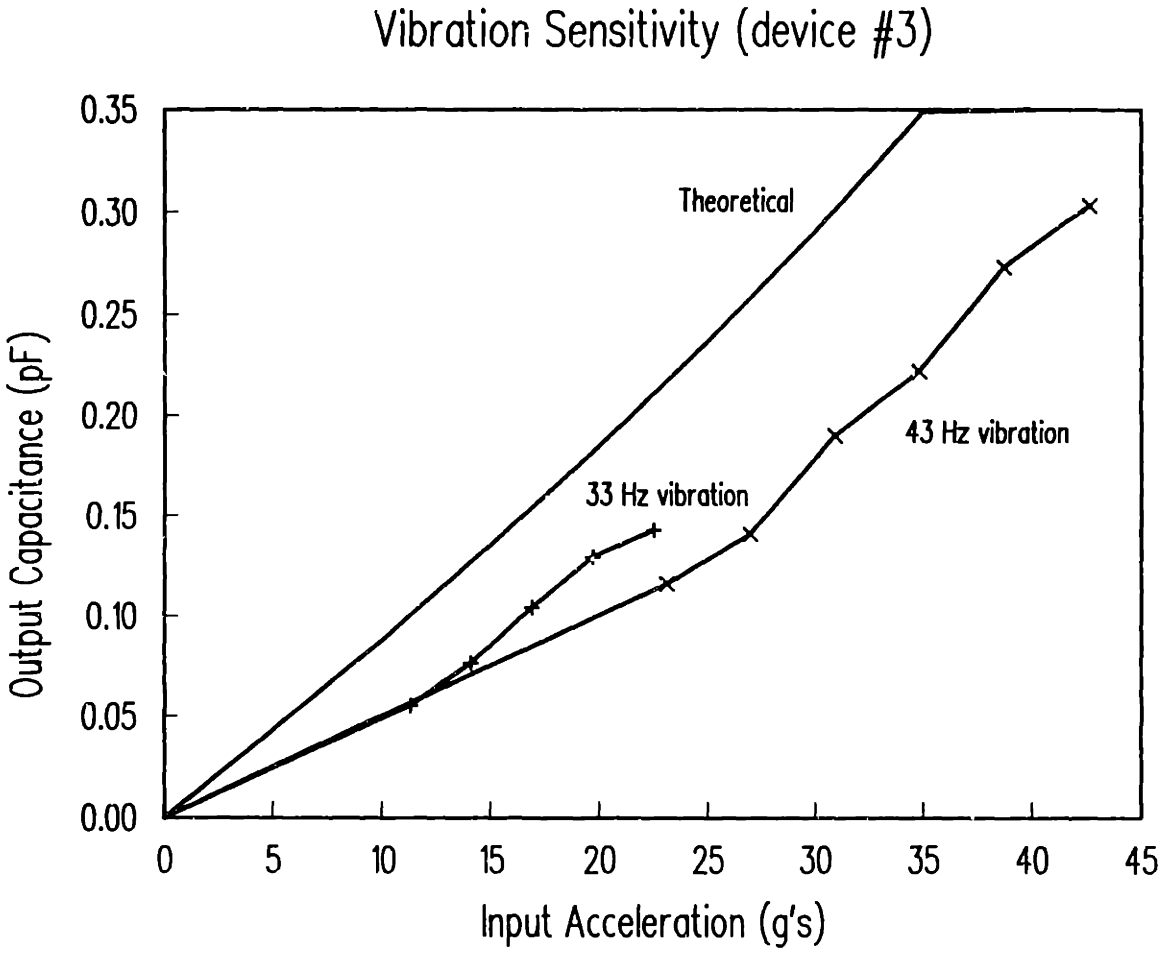

Figure 5-7: Accelerometer sensitivity. Measured and theoretical.

$C_2 - C_1$, for a given input acceleration, gives

$$\Delta C = C_1 \left[\frac{1}{1 - \frac{M}{k}\frac{a}{h_1}} - 1 \right] \tag{5.5}$$

From the C-V data in Section 5.3 we estimated that

$$h_1 = 12um$$

and

$$k = .93N/M$$

We also know that M is less than the design value, because of the lateral etching. We calculate this loss in mass as the total exposed perimeter of the proof mass (including damping holes), times the depth of the etch, 5 um, times one half of the lateral etch, 1.4 um, times the density. This gives

$$\Delta M = .5 \cdot 10^{-9} kg$$

which we subtract from the design value of $5.5 \cdot 10^{-9} kg$, to get

$$M = 5 \cdot 10^{-9} kg$$

With these values, and $g = 9.81$ M/s^2, and $C_1 = 1.92$ pF, we plot the dashed line shown in Figure 5-7. This shows reasonably close agreement with the measured data.

Measurements made on an optical microscope also indicated that the spacing between the proof mass and the handle wafer may be greater than 1.5 um. Using a z-axis micrometer we measured the position of the proof mass corners (top side) relative to the handle wafer. The results were: .0001, .0001 , .0002, and .0005 inches. Also, inspection of optical interference fringes on the proof mass indicated that it was not warped. Therefore, it is quite likely that the proof mass is tilted relative to the handle wafer.

Chapter 6

Conclusions

6.1 Design

A significant conclusion of our mechanical design work is that sensitive accelerometers can be made using thin film process, where the tethers and the proof mass are made in the same film. This is not obvious, because from Equation 2.4 we know that for high sensitivity we need a large proof mass relative to the tether stiffness. This would indicate that we want the proof mass to be thick relative to the tether thickness, which is not typically what we get from thin film processing. Nevertheless, using the pinwheel or folded pinwheel designs shown in this thesis, we can achieve good sensitivity, and without using excessive die space.

Additionally, we have found that the mechanical design is important with respect to the performance of the accelerometer. Errors due to mounting stresses, or from thermally induced stresses, are largely eliminated by designing the tethers to isolate the proof mass from these external stresses. Errors due to nonlinearity in the mechanical response of the sensor can also be eliminated by the tether design.

The issue of gas damping must be addressed for thin film designs. The combination of small gap between the proof mass and the support wafer, and the large proof mass area, leads to an exceptionally high damping ratio, which severely limits the dynamic bandwidth of the sensor. To avoid this, the sensor could be packaged in vacuum, but this adds to the cost and reduces the reliability. We have shown

that perforating the proof mass is an effective solution to the problem. By using peforations, the damping ratio can be designed to the ideal critical damping ratio, which gives maximum dynamic bandwidth. The tradeoff is that the sensor size must increase to makeup for the lost sense capacitance. However, the acceptable minimum sense capacitance is substantially lower when conditioning electronics are integrated on the same chip with the sensor. In this research, we required 1.5 pF capacitance, assuming off-chip circuitry. With on-chip circuitry, this requirement would reduce to about .2 pF. Using this new value, we scale the design shown in Figure 3-8, and find that the size of the sensor could be reduced to about 200 um x 200 um.

Some conclusions can be made regarding the use of finite element analysis for the design of these accelerometers. One use is for the verification of derived mechanical equations. When the finite element results agree with analytical closed-form equations, as we have shown them to do here, this gives the final assurance that no mistakes were made and that nothing was overlooked in the derivations. For other analyses, the FEA is practically essential. For example, calculating the damping pressure on the perforated proof mass, or nonlinear analysis of the proof mass response, or using the full anisotropic material properties of silicon.

6.2 Fabrication

The fabrication results are significant in that the process is quite simple (only three mask steps), yet it yielded working structures. The boron doped membrane, however, is not ideal for producing mechanical or electrical structures. The next step in the development of this process might be the use of an epitaxial layer instead of the boron doped layer. If this is successful, then circuits could be fabricated on the epitaxial layer and eventually integrated with the accelerometer.

6.3 Testing

We were able to show sensitivity to input accelerations using the electrodynamic shaker. This data shows sensitivity of the accelerometers out to 40 g peak sine input. Below 10 g we could not measure the output as it was below the .05 pF sensitivity of the capacitance meter when used for C-t measurements.

The sensitivity of the sensors was less than the design value. Both the shaker test and the capacitance versus bias voltage, show low sensitivity. We have suggested that this may be due to a larger than expected gap between the proof mass and the handle wafer. If we assume this, then the shaker data and the bias voltage data are shown to agree reasonably well. Also, optical measurements on the proof mass indicate that it is not parallel to the handle wafer, but that one end is raised substantially above the handle wafer.

Appendix A

Elastic Material Constants for Silicon

In silicon, the elastic constants relating stress to strain depend on the orientation of the stress and strain within the material. This anisotropic behavior is due directly to the differences in atomic spacing between the three different crystallographic directions [42]. Since silicon has a cubic crystal structure, the elastic constants are the same between two orthogonal directions, which helps to reduce the difficulty that anisotropy adds to mechanical calculations.

Two sets of elastic constants are presented and explained here. The first is the full elastic tensor per the theory of solid continuum mechanics. In practice, this is useful for input into finite element programs. A finite element program can use numerical integration during element formulation to fully account for the anisotropic material behavior. However, a simpler method can be used when the stresses act entirely along a single direction in the silicon. Then we can calculate a Young's modulus and a Poisson's ratio for that direction, and use these engineering constants for calculations with the structural beam, plate, or rod equations.

In solid continuum mechanics theory, the elastic tensor (C) relates the stresses to

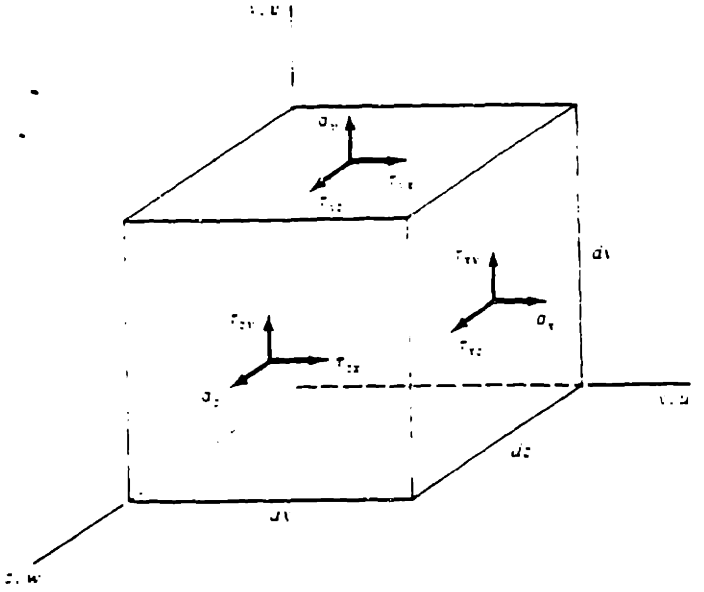

Figure A-1: Stresses on a differential solid element.

the strains in a linear manner according to Hook's law:

$$\begin{pmatrix} \sigma_x \\ \sigma_y \\ \sigma_z \\ \tau_{xy} \\ \tau_{yz} \\ \tau_{zx} \end{pmatrix} = (C) \begin{pmatrix} \epsilon_x \\ \epsilon_y \\ \epsilon_z \\ \gamma_{xy} \\ \gamma_{yz} \\ \gamma_{zx} \end{pmatrix} \tag{A.1}$$

where the stresses are shown in Figure A-1.

For an isotropic material there are only two independent constants in (C), they are Young's modulus E, and Poisson's ratio ν. In addition, for an isotropic material, (C) does not change when it is transformed to other directions.

For silicon, a cubic crystal structure, there are three independent constants, and the tensor will change when transformed to other directions, although it remains the same for orthogonol rotations [43].

For an isotropic material:

$$\begin{pmatrix} \sigma_x \\ \sigma_y \\ \sigma_z \\ \tau_{xy} \\ \tau_{yz} \\ \tau_{zx} \end{pmatrix} = \begin{pmatrix} c_{11} & c_{12} & c_{12} & 0 & 0 & 0 \\ c_{12} & c_{11} & c_{12} & 0 & 0 & 0 \\ c_{12} & c_{12} & c_{11} & 0 & 0 & 0 \\ 0 & 0 & 0 & c_{44} & 0 & 0 \\ 0 & 0 & 0 & 0 & c_{44} & 0 \\ 0 & 0 & 0 & 0 & 0 & c_{44} \end{pmatrix} \begin{pmatrix} \epsilon_x \\ \epsilon_y \\ \epsilon_z \\ \gamma_{xy} \\ \gamma_{yz} \\ \gamma_{zx} \end{pmatrix} \tag{A.2}$$

Or, in terms of E and ν, for an isotropic material:

$$\begin{pmatrix} \sigma_x \\ \sigma_y \\ \sigma_z \\ \tau_{xy} \\ \tau_{yz} \\ \tau_{zx} \end{pmatrix} = \frac{E}{(1+\nu)(1-\nu)} \begin{pmatrix} 1-\nu & \nu & \nu & 0 & 0 & 0 \\ \nu & 1-\nu & \nu & 0 & 0 & 0 \\ \nu & \nu & 1-\nu & 0 & 0 & 0 \\ 0 & 0 & 0 & \frac{1-2\nu}{2} & 0 & 0 \\ 0 & 0 & 0 & 0 & \frac{1-2\nu}{2} & 0 \\ 0 & 0 & 0 & 0 & 0 & \frac{1-2\nu}{2} \end{pmatrix} \begin{pmatrix} \epsilon_x \\ \epsilon_y \\ \epsilon_z \\ \gamma_{xy} \\ \gamma_{yz} \\ \gamma_{zx} \end{pmatrix} \tag{A.3}$$

For a cubic crystal material, with the reference axis oriented along a primary crystal axis:

$$\begin{pmatrix} \sigma_x \\ \sigma_y \\ \sigma_z \\ \tau_{xy} \\ \tau_{yz} \\ \tau_{zx} \end{pmatrix} = \begin{pmatrix} c_{11}^{1} & c_{12}^{2} & c_{12}^{4} & 0 & 0 & 0 \\ c_{12} & c_{11}^{3} & c_{12}^{5} & 0 & 0 & 0 \\ c_{12} & c_{12} & c_{11}^{6} & 0 & 0 & 0 \\ 0 & 0 & 0 & c_{44}^{10} & 0 & 0 \\ 0 & 0 & 0 & 0 & c_{44}^{15} & 0 \\ 0 & 0 & 0 & 0 & 0 & c_{44}^{21} \end{pmatrix} \begin{pmatrix} \epsilon_x \\ \epsilon_y \\ \epsilon_z \\ \gamma_{xy} \\ \gamma_{yz} \\ \gamma_{zx} \end{pmatrix} \tag{A.4}$$

which is exactly the same as Equation A.2 for an isotropic material, except that now there are three independent constants. (The superscripts indicate the order in which these constants are input into the ABAQUS finite element program.) For silicon, the constants are [44]:

$C_{11} = 1.6564 \cdot 10^{11}$ Pa

$C_{12} = .6394 \cdot 10^{11}$ Pa

$C_{44} = .7951 \cdot 10^{11}$ Pa

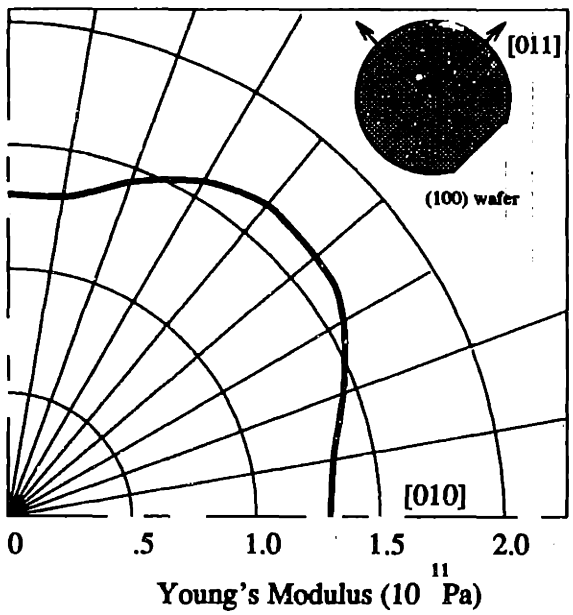

Figure A-2: Young's modulus as a function of direction in the (100) plane.

If the stresses act entirely in one direction, then the elastic constants can be reduced to a Young's modulus and a Poisson's ratio for that direction. If the direction of stress is i, then Young's modulus is defined as the stress over strain,

$$E_i \equiv \frac{\sigma_i}{\epsilon_i} \tag{A.5}$$

and Poisson's ratio relates the strain in another direction j, relative to the strain in the i direction,

$$\nu_{ij} \equiv \frac{\epsilon_j}{\epsilon_i} \tag{A.6}$$

The transformation of equation A.4 to angles other than the primary crystallographic angles, and the determination of E and ν has been done [45]. A plot of the results for E is shown in Figure A-2 for the (100) silicon plane.

Appendix B

Equations for Tether Mechanical Design

B.1 Equations for Straight Tether Designs

See Figure 2-3 for the definition of variables. Also note that the accuracy of these equations is verified by the comparison to finite element results, presented in Tables 2.1 through 2.3.

Input Axis:

$$\delta = \frac{Mg}{4}\frac{l^3}{Ebt^3} \tag{B.1}$$

$$f = \frac{1}{2\pi}\sqrt{\frac{g}{\delta}} \tag{B.2}$$

$$\sigma = \frac{Mg}{4}\frac{l}{2}\frac{t}{2}\frac{12}{bt^3} \tag{B.3}$$

Pendulous Axis:

$$\delta = \frac{Mg}{4}\frac{l}{btE} \tag{B.4}$$

$$f = \frac{1}{2\pi}\sqrt{\frac{g}{\delta}} \tag{B.5}$$

$$\sigma = \frac{Mg}{4}\frac{1}{bt} \tag{B.6}$$

Hinge Axis:

$$\delta = \frac{Mg}{4}\frac{l^3}{Etb^3} \tag{B.7}$$

$$f = \frac{1}{2\pi}\sqrt{\frac{g}{\delta}} \tag{B.8}$$

$$\sigma = \frac{Mg}{4}\frac{l}{2}\frac{b}{2}\frac{12}{tb^3} \tag{B.9}$$

δ = displacement for 1g acceleration along the input axis, pendulous axis, or hinge axis

f = undamped resonant frequency

M = proof mass

g = gravitational acceleration constant

l = tether length

t = tether thickness

E = modulus of elasticity

b = tether width

σ = maximum stress

B.2 Equations for Pinwheel Tether Designs

Refer to Figure 2-4 for definition of the variables.

Input Axis:

$$\delta = \frac{Mg}{4}\frac{l^3}{Ebt^3} \tag{B.10}$$

$$f = \frac{1}{2\pi}\sqrt{\frac{g}{\delta}} \tag{B.11}$$

$$\sigma = \frac{Mg}{4}\frac{l}{2}\frac{t}{2}\frac{12}{bt^3} \tag{B.12}$$

Pendulous Axis and Hinge Axis:

$$K_1 = \frac{btE}{l} \tag{B.13}$$

$$K_2 = Et(\frac{b}{l})^3 \tag{B.14}$$

$$\delta = \frac{Mg}{2K_1 + 2K_2} \tag{B.15}$$

$$f = \frac{1}{2\pi}\sqrt{\frac{g}{\delta}} \tag{B.16}$$

$$\sigma = \delta\left(K_2\frac{l}{2}\frac{b}{2}\frac{12}{tb^3} + K_1\frac{1}{bt}\right) \tag{B.17}$$

K_1 = axial spring constant of a single tether

K_2 = in-plane bending spring constant of a single tether

δ = displacement for 1g acceleration along the input axis, pendulous axis, or hinge axis

f = undamped resonant frequency

M = proof mass

g = gravitational acceleration constant

l = tether length

t = tether thickness

E = modulus of elasticity

b = tether width

σ = maximum stress

B.3 Equations for the Folded Pinwheel Designs

Refer to Figure 2-6 for definition of the variables.

Input Axis:

$$R \equiv \frac{EI_1}{GJ_2}\frac{s}{l} \tag{B.18}$$

$$\delta_1 = \frac{Mg}{2}\frac{l^3}{12EI_1}(4 - \frac{6}{2+R}) \tag{B.19}$$

$$\delta_2 = \frac{Mg}{2}\frac{s^2 l}{4GJ_1} \tag{B.20}$$

$$\delta_3 = \frac{Mg}{2}\frac{s^3}{24EI_2} \tag{B.21}$$

$$\delta = \delta_1 + \delta_2 + \delta_3 \tag{B.22}$$

$$f = \frac{1}{2\pi}\sqrt{\frac{g}{\delta}} \tag{B.23}$$

$$\sigma = \frac{Mg}{4} l \left(1 - \frac{1}{2+R}\right) \frac{\frac{t}{2}}{I_1} \tag{B.24}$$

Pendulous Axis and Hinge Axis:

$$C_1 = \frac{l^3}{12EI_1'}\left(2 + \frac{3}{\frac{l}{s}\frac{I_2'}{I_1'} + \frac{1}{2}}\right) \tag{B.25}$$

$$C_2 = \frac{s^3}{12EI_2'} + \frac{ls^2}{2EI_1'} + \frac{2l}{A_1E} \tag{B.26}$$

$$\delta = \frac{Mg}{\frac{2}{C_1} + \frac{2}{C_2}} \tag{B.27}$$

$$f = \frac{1}{2\pi}\sqrt{\frac{g}{\delta}} \tag{B.28}$$

$$\sigma = \frac{Mg}{4}\frac{b}{2}\frac{s}{I_1'} \tag{B.29}$$

δ = displacement for 1g acceleration along the input axis, pendulous axis, or hinge axis.

M = proof mass

g = gravitational acceleration constant

s = connecting tether length

l = main tether length

t = tether thickness (main and connecting tethers)

E = modulus of elasticity

G = shear modulus

b = main tether width

w = connecting tether width

σ = maximum stress

$I_1 = \frac{bt^3}{12}$

$I_1' = \frac{tb^3}{12}$

$J_1 = \beta_1 bt^3$

β_1 = torsion factor, main tether

$A_1 = bt$

$I_2 = \frac{wt^3}{12}$

$I_2' = \frac{tw^3}{12}$

$J_2 = \beta_2 wt^3$

β_2 = torsion factor, connecting tether

$A_2 = wt$

B.4 Derivation of Equations for Straight Tether Designs

In general, we will use the following derivation procedure:

1. Draw the free body diagram of the static forces and moments.

2. Write the equations of force and moment equilibrium.

3. Write the beam equations for the shear force , bending moment, angle of beam rotation, and displacement, as a function of position along the tether length.

4. Solve 2 and 3 to find the displacement.

Note that once we solve for the deflection per g, δ, it can be converted into an equivalent spring constant, k, acting at the center of mass,

$$k = \frac{Mg}{\delta} \tag{B.30}$$

Displacement for input axis accelerations (Equation B.1) :

The deflected shape, and the free body diagram are drawn in Figure B-1. In this figure, the circles with arrow heads represent bending moments, and the straight arrows represent forces. Static force equilibrium in the y-direction gives the value of the shear force, $v(x)$, acting on each tether,

$$v(x) = \frac{Mg}{4} \tag{B.31}$$

The bending moment along the beam length is,

$$\begin{aligned} m(x) &= -\int v(x) \cdot \delta x \\ &= -\tfrac{Mg}{4} x + C \end{aligned}$$

By symmetry, we know that $m(x = 0) = -m(x = l)$, therefore,

$$C = \frac{Mg}{8} l$$

$$m(x) = \frac{Mg}{4} \left(\frac{l}{2} - x \right) \tag{B.32}$$

Integrating the moment to get the angle of rotation,

$$\begin{aligned} \theta(x) &= \tfrac{1}{EI} \int m(x) \cdot \delta x \\ &= \tfrac{1}{EI} \int \tfrac{Mg}{4} (l/2 - x) \cdot \delta x \\ &= \tfrac{1}{EI} \tfrac{Mg}{4} \left(\tfrac{l}{2} x - \tfrac{x^2}{2} \right) + C \end{aligned}$$

and $C = 0$ because $\theta(x = 0) = 0$. Finally, integrate the angle to get the displacement,

$$\begin{aligned} y(x) &= \int \theta(x) \cdot \delta x \\ &= \frac{1}{EI}\frac{Mg}{4}\left(\frac{x^2}{4}l - \frac{x^3}{6}\right) + C \end{aligned}$$

and $C = 0$ because $y(x = 0) = 0$. Assuming that the tethers have rectangular cross-sections with thickness t and width b, we substitute $I = bt^3/12$ for the area moment of inertia. Then the deflection at $x = l$ gives Equation B.1,

$$y(x = l) = \frac{Mg}{4}\frac{l^3}{Ebt^3} \tag{B.33}$$

Maximum stress for input axis accelerations (Equation B.3) :
The maximum bending stress occurs at the two attachment points of the tethers, where the moment $m(x)$ is maximum. Using equation Equation B.32 for the moment along the beam,

$$m(x = 0) = \frac{Mg}{4}\frac{l}{2} \tag{B.34}$$

The maximum stress is the maximum moment times the distance from the beam neutral axis to the outermost beam fiber, which is one half the tether thickness; divided by the area moment of inertia, $I = bt^3/12$. Therefore,

$$\sigma = \frac{Mg}{4}\frac{l}{2}\frac{t}{2}\frac{12}{bt^3} \tag{B.35}$$

This bending stress is the only significant stress component; shear stress is negligible.

Displacement and stress for pendulous axis accelerations (Equations B.4, B.6) :
The free body diagram for this displacement is shown in Figure B-2. Acceleration along the pendulous axis loads the four tethers in pure axial tension and compression. Summation of forces in the x-direction gives the value of the axial force, p,

$$p = \frac{Mg}{4} \tag{B.36}$$

The stress is the force divided by the area of the tethers,

$$\sigma = \frac{Mg}{4}\frac{1}{bt} \tag{B.37}$$

From the definition of Young's modulus, the strain is the stress divided by the Young's modulus, and the total displacement, δ, of the tethers in the x-direction, is the strain times the tether length. Therefore,

$$\delta = \frac{Mg}{4}\frac{l}{btE} \tag{B.38}$$

Displacement and stress for hinge axis accelerations (Equations B.7, B.9) :
The tether deflections and the free body diagram are shown in Figure B-3. All four tethers bend with the same zero-rotation end condition as they do for input axis accelerations, except that now the deflection is in the plane of the proof mass instead of perpendicular to the plane as it is for input axis accelerations. Because of this, the derivations and the final equations are the same as for input accelerations, except that we replace tether thickness, t, with the width, b, and vice-versa.

B.5 Derivation of Equations for Pinwheel Tether Designs

Displacement and stress for input axis accelerations (Equations B.10, B.12) :
At least for linear analysis, the input axis deflection and stress for the pinwheel design are the same as for the straight tether design. All four tethers will deflect as beams with no rotation at the ends, and the maximum stress occurs at the attachment points. When nonlinearities are considered, however, we find that the straight tethers have a significant stress stiffening effect, which is covered in Section 2.6.

Displacement for hinge axis or pendulous axis accelerations (Equation B.15) :
For this derivation, we only need to draw the free body diagram and write the force equilibrium equations. Then we use the results from the previous derivations instead

of solving the beam equations again. Figure B-4 shows the deflected shape and the free body forces and moments. Notice that two of the tethers are in pure axial tension and compression, and the other two bend with no rotation at the ends. We already know the spring constants for both of these beams. For the the axial tension/compression tethers, we find the spring constant by substituting Equation B.4 into Equation B.30. We also have to divide by four since these equations assumed four tethers, and we want the spring constant for just one tether. Repeating Equation B.4,

$$\delta = \frac{Mg}{4}\frac{l}{btE}$$

and Equation B.30,

$$k = \frac{Mg}{\delta}$$

and making the substitution and multiplying by four gives,

$$K_1 = \frac{btE}{l} \tag{B.39}$$

We do the same procedure for the bending tethers. We use Equation B.7,

$$\delta = \frac{Mg}{4}\frac{l^3}{Etb^3}$$

and substitute four times this into equation B.30 to get,

$$K_2 = Et(\frac{b}{l})^3 \tag{B.40}$$

With these equivalent spring constants, we can do a force balance in the y-direction,

$$Mg = \delta\,(2K_1 + 2K_2)$$

and so this gives equation B.15, repeated here,

$$\delta = \frac{Mg}{2K_1 + 2K_2} \tag{B.41}$$

Maximum stress for hinge or pendulous axis accelerations (Equations B.17) : Again, we will use our previous results for this analysis. The maximum stress in the bending tethers occurs at the attachment points. It is equal to the maximum moment, m, times the maximum distance from the neutral axis of the tether to the outermost fiber, which in this case is half the tether width, $b/2$; divided by the area moment of inertia, $I = tb^3/12$,

$$\sigma = \frac{m\frac{b}{2}}{I} = \frac{6m}{tb^2}$$

In Section B.4 we already showed that for bending with zero rotation at the ends, the maximum moment is the shear force, v, times half of the tether length (Equation B.34),

$$m = v\frac{l}{2}$$

The shear force is given by the spring constant K_2 times the displacement,

$$v = K_2 \cdot \delta$$

Combining these last three equations gives the maximum bending stress,

$$\sigma = \delta K_2 \frac{l}{2}\frac{b}{2}\frac{12}{tb^3} \tag{B.42}$$

We also must consider the stress in the two tethers loaded in tension and compression. The axial force on these is given by the displacement, δ, time the axial spring constant,

$$p = \delta \cdot K_1$$

and the stress is the axial force divided by the tether area,

$$\sigma = \delta K_1 \frac{1}{bt} \tag{B.43}$$

The maximum stress is the larger of these two. Or, to be conservative, simply add the two together and use the sum as the maximum stress, as we have done in Equation B.17.

B.6 Derivation of Equations for Folded Pinwheel Tether Designs

These derivations become difficult because now each tether is made up of three straight beam segments, and the boundary conditions between the beam segments are not known beforehand. The fastest way to solve this problem is to set up the finite element equations in matrix form, and solve the matrix with a computer math program. This is better than using a finite element program because the design variables (eg. tether length, thickness, etc.) are parameters in the program, whereas a finite element model would have to be remeshed in order to change the design parameters. But here we do the derivation to arrive at the closed-form solutions.

Displacement for input axis accelerations (Equations B.19 through B.22) : Following the same procedure as before, we draw the free body forces acting on the tethers. A single folded tether, deflected along the input axis, is shown in Figure B-5. We do not show all four folded tethers in the figure, because it is just too difficult to draw. However, we know that each tether will deform in the same manner. We refer to the middle segment of the folded tether as the 'connecting tether', and the other two segments as 'main tethers'.

Figure B-5 shows the total displacement as being the sum of $\delta_1 + \delta_2 + \delta_3$. The first displacement, δ_1, is the bending deflection of the main tethers. This bending mode does not quite have zero-rotation end conditions, because torsion of the connecting tether allows for some rotation. The second displacement, δ_2, is due to the torsion of the main tether multiplied by the length of the connecting tether. The third displacement, δ_3 is the bending of the connecting tether. Notice that torsion in both the main and in the connecting tethers, effects the total displacement.

Figure B-5 shows the free body forces and moments. Double arrow notation is

used to indicate moments, as opposed to the circles used in the previous free body diagrams. Also, we use symmetry and only draw one half of the tether in the free body diagram. At the symmetric boundary, the bending moment and the beam rotation are zero (although there is still a rigid body rotation of the connecting tether that creates δ_2).

After drawing the free body diagram, the next step is to use the force and moment equilibrium equations. Summation of forces in the y-direction (out of the page) gives,

$$v = \frac{Mg}{4} \tag{B.44}$$

Summation of the bending moments on the connecting tether gives,

$$m_1 = v\frac{s}{2} = \frac{Mg}{4}\frac{s}{2} \tag{B.45}$$

And summation of the bending moments on the main tether gives,

$$m_3 = vl - m_2 = \frac{Mg}{4}l - m_2 \tag{B.46}$$

These last three equations allow us to solve directly for m_1 and for v, and then for δ_2 and δ_3. But to find m_2 and m_3 we will also have to use the beam equations. Before doing that, we will find δ_2 and δ_3. The δ_3 deflection is just bending with zero rotation at the ends, so we can use Equation B.1 with s as the length instead of l, and w as the width instead of b,

$$\delta_3 = \frac{Mg}{4}\frac{s^3}{Ewt^3}$$

and substitute $I_2 = wt^3/12$,

$$\delta_3 = \frac{Mg}{4}\frac{s^3}{12EI_2} \tag{B.47}$$

Next, we find δ_2. Deflection δ_2 is just the angle of twist due to the torque m_1 on the main tether, multiplied by the length of the connecting tether,

$$\begin{aligned} \delta_2 &= \frac{m_1}{GJ_1}ls \\ &= \frac{\frac{Mg}{4}\frac{s}{2}}{GJ_1}ls \end{aligned}$$

This gives us the expression for δ_2,

$$\delta_2 = \frac{Mg}{4}\frac{s^2}{2}\frac{l}{GJ_1} \tag{B.48}$$

Now we return to Equation B.46 to find δ_1. We introduce the beam equation in order to get another equation in m_2 and m_3. We write the beam equation in terms of x, the distance along the main tether, with $x = 0$ at the support, where the displacement and the rotation are both zero.

$$\begin{aligned}\theta(x) &= \tfrac{1}{EI_1}\int m(x)\cdot\delta x \\ &= \tfrac{1}{EI_1}\int\left(m_3 - \tfrac{Mg}{4}x\right)\cdot\delta x \\ &= \tfrac{1}{EI_1}\left(m_3 x - \tfrac{Mg}{4}\tfrac{x^2}{2}\right) + C\end{aligned}$$

and $C = 0$ because $\theta(x = 0) = 0$. Substitute Equation B.46 into the above to write it in terms of m_2 instead of m_3. This gives,

$$\theta(x) = \frac{1}{EI_1}\left[\frac{Mg}{4}\left(lx - \frac{x^2}{2}\right) - m_2 x\right]$$

At this point we can eliminate m_2, because we know that where the main tether attaches to the connecting tether, the bending rotation in the main tether equals the twist (rotation due to torque) in the connecting tether,

$$\theta(x = l) = \frac{m_2}{GJ_2}\frac{s}{2}$$

Solving for m_2 we get,

$$m_2 = \frac{Mg}{4}\frac{l}{2+R} \tag{B.49}$$

where R is defined in Section B.3. Then the beam equation for θ becomes,

$$\theta(x) = \frac{1}{EI_1}\left[\frac{Mg}{4}\left(lx - \frac{x^2}{2}\right) - \frac{Mg}{4}\frac{l}{2+R}x\right]$$

Integrate this one more time to get the deflection $y(x)$,

$$y(x) = \frac{Mg}{4EI_1}\left(\frac{x^2}{2}l - \frac{x^3}{6} - \frac{l}{2+R}\frac{x^2}{2}\right)$$

Evaluating this at $x = l$, and multiplying by two (because there are two main tethers) gives the deflection δ_1 that we want,

$$\delta_1 = \frac{Mg}{2}\frac{l^3}{12EI_1}(4 - \frac{6}{2+R}) \tag{B.50}$$

The factor R is important because it is the ratio of the main tether's bending stiffness to the connecting tether's torsional stiffness. As R goes to zero, the connecting tether does not allow the main tether to bend at the attachment point, and so Equation B.50 approaches that for a beam with zero rotations at the ends. As R goes to infinity, the main tether is allowed to deflect and becomes more like a fixed-free beam.

Maximum stress for input axis accelerations (Equations B.24) :
The maximum stress occurs in the main tether where it attaches to ground. The moment here is m_3. From Equations B.46 and B.49 we get,

$$m_3 = \frac{Mg}{4}l\left(1 - \frac{1}{2+R}\right)$$

Then the stress is just the moment times the distance from the neutral axis to the outermost beam fiber, which in this case is $t/2$; divided by the area moment of inertia, I_1. Therefore,

$$\sigma = \frac{Mg}{4}l\left(1 - \frac{1}{2+R}\right)\frac{\frac{t}{2}}{I_1} \tag{B.51}$$

Displacement for pendulous or hinge axis accelerations (Equation B.27) :
For pendulous or hinge axis accelerations, the tethers do not all deflect in the same manner. Refering to Figure B-6, two of the tethers have a 'soft' deflection mode, with equivalent spring constant of K_1. The other two tethers deform in their 'hard' direction, with an equivalent spring constant of K_2. We will find these two spring constants for the folded tether. Actually we will calculate the spring compliances, which are the inverse of the spring constants,

$$C_1 = \frac{1}{K_1}$$

$$C_2 = \frac{1}{K_2}$$

Once we have the spring constants, we will add them together as springs in parallel, so that the total proof mass deflection is given by Equation B.27,

$$\delta = \frac{Mg}{\frac{2}{C_1} + \frac{2}{C_2}}$$

This reduces the problem to that of finding C_1 and C_2. We will start with C_1, which is the compliance in the soft direction. Figure B-7 is the free body diagram of the forces and moments. The force, F, that the proof mass exerts on the tether, is an unknown, as well as the two moments, m_1 and m_2. The displacement unknowns are y_1, which is the displacement at the applied force; y_2, which is the y-displacment of the point where beam 1 attaches to beam 2; and θ_2, which is the rotation at the same attachment point. The unknown that we are primarily interested in is y_1. The three segments are also numbered in the figure (the numbers in the box). We will refer to these numbers in the derivation.

From a balance of moments on beam 1 we get,

$$m_1 - m_2 = F \cdot l \tag{B.52}$$

The beam equations for beam 1 give,

$$\begin{aligned} m(x) &= -\int v \cdot \delta x \\ &= Fx - m_1 \\ \theta(x) &= \tfrac{1}{EI_1} \int m(x) \cdot \delta x \end{aligned}$$

$$\theta(x) = \frac{1}{EI_1}\left(F\frac{x^2}{2} - m_1 x\right) \tag{B.53}$$

$$y(x) = \int \theta(x) \cdot \delta x$$

$$y(x) = \frac{1}{EI_1}\left(F\frac{x^3}{6} - m_1\frac{x^2}{2}\right) + y_1 \tag{B.54}$$

The equations for beam 2 are,

$$
\begin{aligned}
m(y) &= -\int v \cdot \delta y \\
&= m_2 \\
&= Fl - m_1 \\
\theta(y) &= \tfrac{1}{EI_2} \int m(y) \cdot \delta y \\
&= \tfrac{1}{EI_2} (Fly - m_1 y) + c
\end{aligned}
$$

Using the symmetry condition that $\theta(y = s/2) = 0$, gives the value for c, therefore,

$$\theta(y) = \frac{1}{EI_2} (Fl - m_1) \left(y - \frac{s}{2} \right) \tag{B.55}$$

By using the two θ equations above, Equations B.53 and B.55, we get two expressions for θ_2 in F and m_1. We combine these to eliminate θ_2, resulting in, an expression for m_1,

$$m_1 = \frac{Fl}{2} \left(1 + \frac{1}{\frac{2I}{s}\frac{I_2}{I_1} + 1} \right) \tag{B.56}$$

Next, write the beam equations for beam 3,

$$
\begin{aligned}
m(x) &= -\int v \cdot \delta x \\
&= -Fx + m_1 \\
\theta(x) &= \tfrac{1}{EI_1} \int m(x) \cdot \delta x \\
&= \tfrac{1}{EI_1} \left(-F\tfrac{x^2}{2} + m_1 x \right) \\
y(x) &= \int \theta(x) \cdot \delta x
\end{aligned}
$$

$$y(x) = \frac{1}{EI_1} \left(-F\frac{x^3}{6} + m_1 \frac{x^2}{2} \right) \tag{B.57}$$

The two equations for y, Equations B.57 and B.54, can both be evaluated at $x = l$ to give an expression for y_2, in terms of y_1 and m_1. We equate these two expressions to eliminate y_2. This assumes that the axial compression or extension of the connecting tether is neglible, which we have shown to be true in that the axial displacements are about 1000 times less than the bending displacements. When we equate these two expressions for y_2, and substitute in Equation B.56 to eliminate m_1, the result is,

$$y_1 = \frac{Fl^3}{12EI_1} \left(2 + \frac{3}{\frac{l}{s}\frac{I_2}{I_1} + \frac{1}{2}} \right)$$

This gives the compliance C_1, which is the displacment divided by the applied force,

$$C_1 = \frac{l^3}{12EI_1}\left(2 + \frac{3}{\frac{I}{s}\frac{I_2}{I_1} + \frac{1}{2}}\right) \tag{B.58}$$

Now, using the same procedure, we will find C_2. The free body diagram is shown in Figure B-8 on the left. There are three force/moment unknowns. The displacements are indicated on the right hand side of the figure. Any displacements not shown are zero. There are seven unknown displacements/rotations. We want to express the displacement x_1 in terms of the applied force, F, so we will need nine equations to do this. Our goal will be to set up the nine equations. The solution is obtained by performing elimination on the nine equations to express x_1 in terms of F. This is a fairly tedious, but straightforward, algebraic procedure.

A moment balance on beam 2 gives the first equation.

$$m_1 + m_2 = F \cdot s \tag{B.59}$$

Writing the beam equations to beam 1,

$$\begin{aligned} m(x) &= -\int v \cdot \delta x \\ &= m_1 \\ \theta(x) &= \tfrac{1}{EI_1}\int m(x) \cdot \delta x \\ &= \tfrac{1}{EI_1} m_1 x \end{aligned}$$

Applying the last equation at $x = l$ gives the second equation,

$$\theta_2 = \frac{1}{EI_1} m_1 l \tag{B.60}$$

Continuing with beam 1, integrate the rotation to get the displacement,

$$\begin{aligned} y(x) &= \int \theta(x) \cdot \delta x \\ &= \tfrac{1}{EI_1} m_1 \tfrac{x^2}{2} \end{aligned}$$

Applying this at $x = l$ gives the third equation,

$$y_2 = \frac{1}{EI_1} m_1 \frac{l^2}{2} \tag{B.61}$$

The fourth equation comes from beam 1 by taking the difference between x_2 and x_1 as the axial compression developed in beam 1,

$$x_2 - x_1 = \frac{Fl}{EA_1} \tag{B.62}$$

Writing the beam equations for beam 2,

$$\begin{aligned} m(y) &= -\int v \cdot \delta y \\ &= Fy - m_1 \\ \theta(y) &= \tfrac{1}{EI_2} \int m(y) \cdot \delta y \\ &= \tfrac{1}{EI_2} \left(F\tfrac{y^2}{2} - m_1 y \right) + \theta_2 \end{aligned}$$

Applying this equation at $y = s$ gives equation number five,

$$\theta_3 = \frac{1}{EI_2} \left(F\frac{s^2}{2} - m_1 s \right) + \theta_2 \tag{B.63}$$

Continuing to integrate on beam 2 gives,

$$\begin{aligned} x(y) &= -\int \theta(y) \cdot \delta y \\ &= -\tfrac{1}{EI_2} \left(F\tfrac{y^3}{6} - m_1\tfrac{y^2}{2} \right) - \theta_2 y + x_2 \end{aligned}$$

Applying this at $y = s$ gives the sixth equation,

$$x_3 = -\frac{1}{EI_2} \left(F\frac{s^3}{6} - m_1\frac{s^2}{2} \right) - \theta_2 s + x_2 x_3 = -m_1\frac{s^2}{2} - F\frac{s^3}{6} + x_2 \tag{B.64}$$

Writing the beam equations for beam 3,

$$\begin{aligned} m(x) &= -\int v \cdot \delta x \\ &= m_2 \\ \theta(x) &= \tfrac{1}{EI_1} \int m(x) \cdot \delta x \\ &= \tfrac{1}{EI_1} m_2 x \end{aligned}$$

Applying the last equation at $x = l$ gives equation number seven,

$$\theta_3 = \frac{1}{EI_1} m_2 l \tag{B.65}$$

Continuing with beam 3, integrate the rotation to get the displacement,

$$\begin{aligned} y(x) &= \int \theta(x) \cdot \delta x \\ &= \frac{1}{EI_1} m_2 \frac{x^2}{2} \end{aligned}$$

Applying this at $x = l$ gives equation number eight,

$$y_3 = \frac{1}{EI_1} m_2 \frac{l^2}{2} \tag{B.66}$$

And finally, we get the last equation, number nine, by considering the axial tension developed in beam 3 by displacement x_3,

$$x_3 = \frac{Fl}{EA_1} \tag{B.67}$$

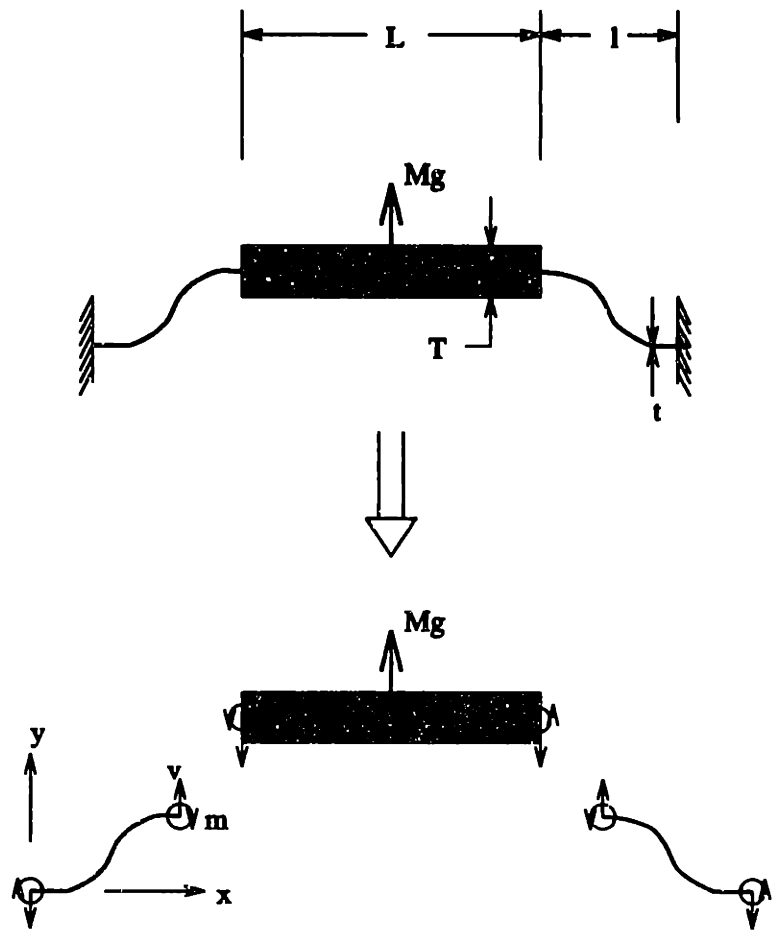

Figure B-1: Deflected shape and free body diagram of straight tether design subjected to input axis acceleration.

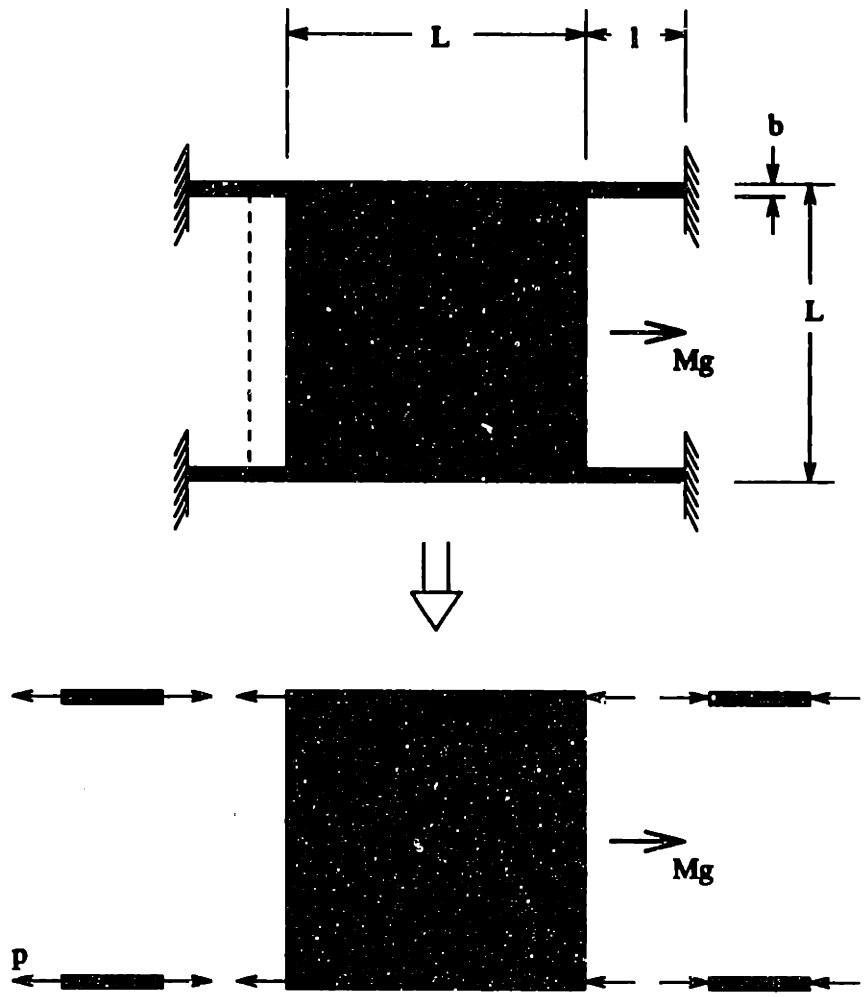

Figure B-2: Deflected shape and free body diagram of straight tether design subjected to pendulous axis acceleration.

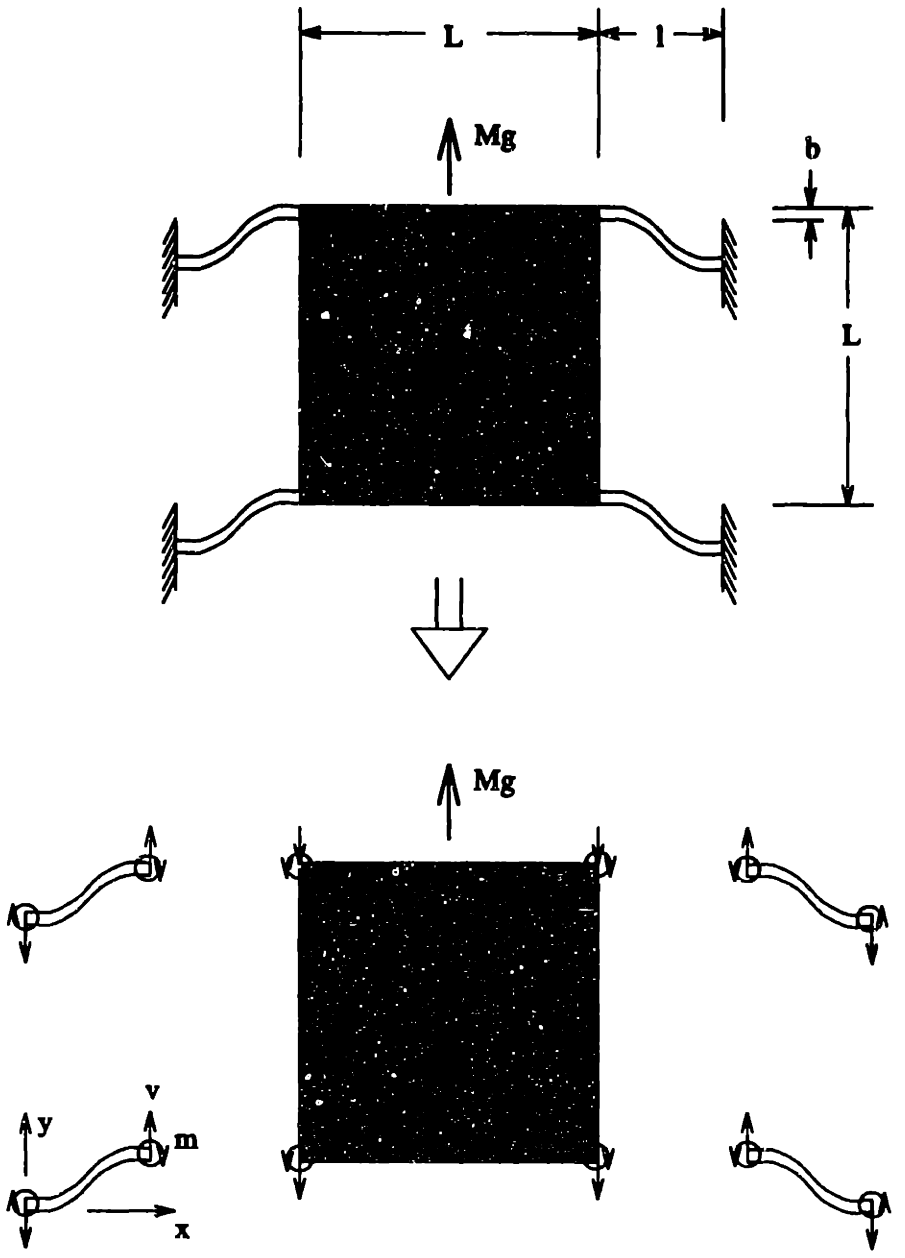

Figure B-3: Deflected shape and free body diagram of straight tether design subjected to hinge axis acceleration.

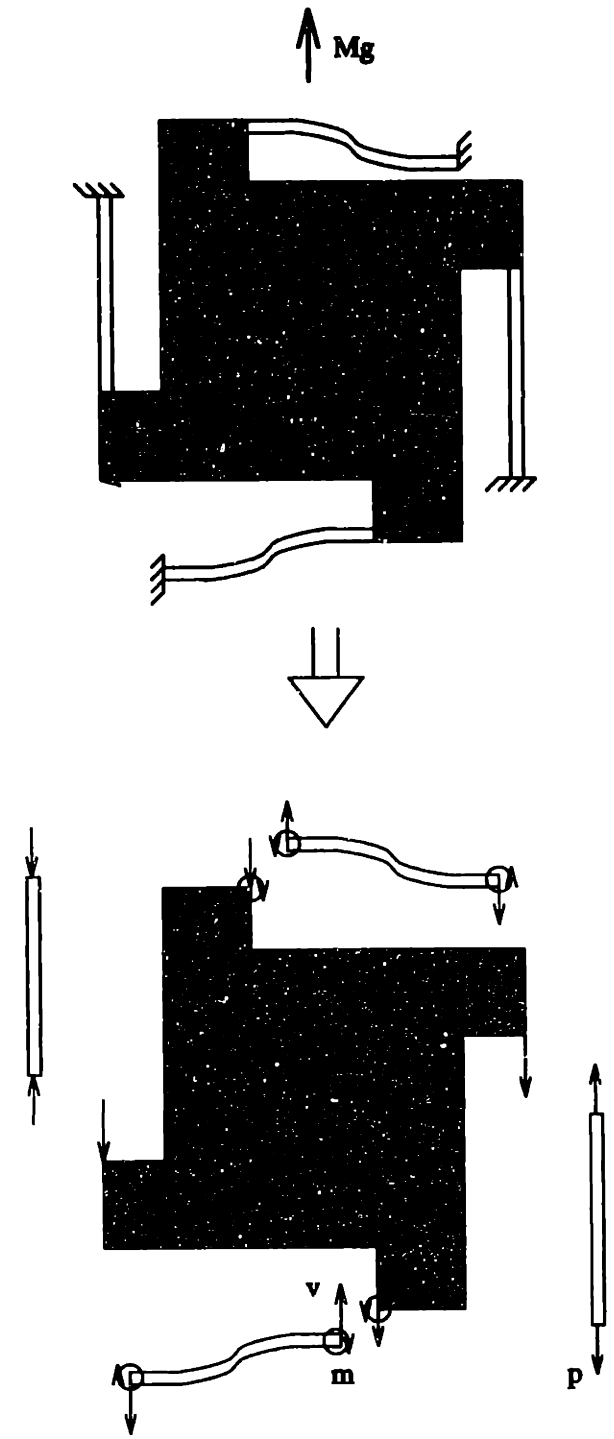

Figure B-4: Deflected shape and free body diagram of pinwheel tether design subjected to pendulous axis or hinge axis acceleration.

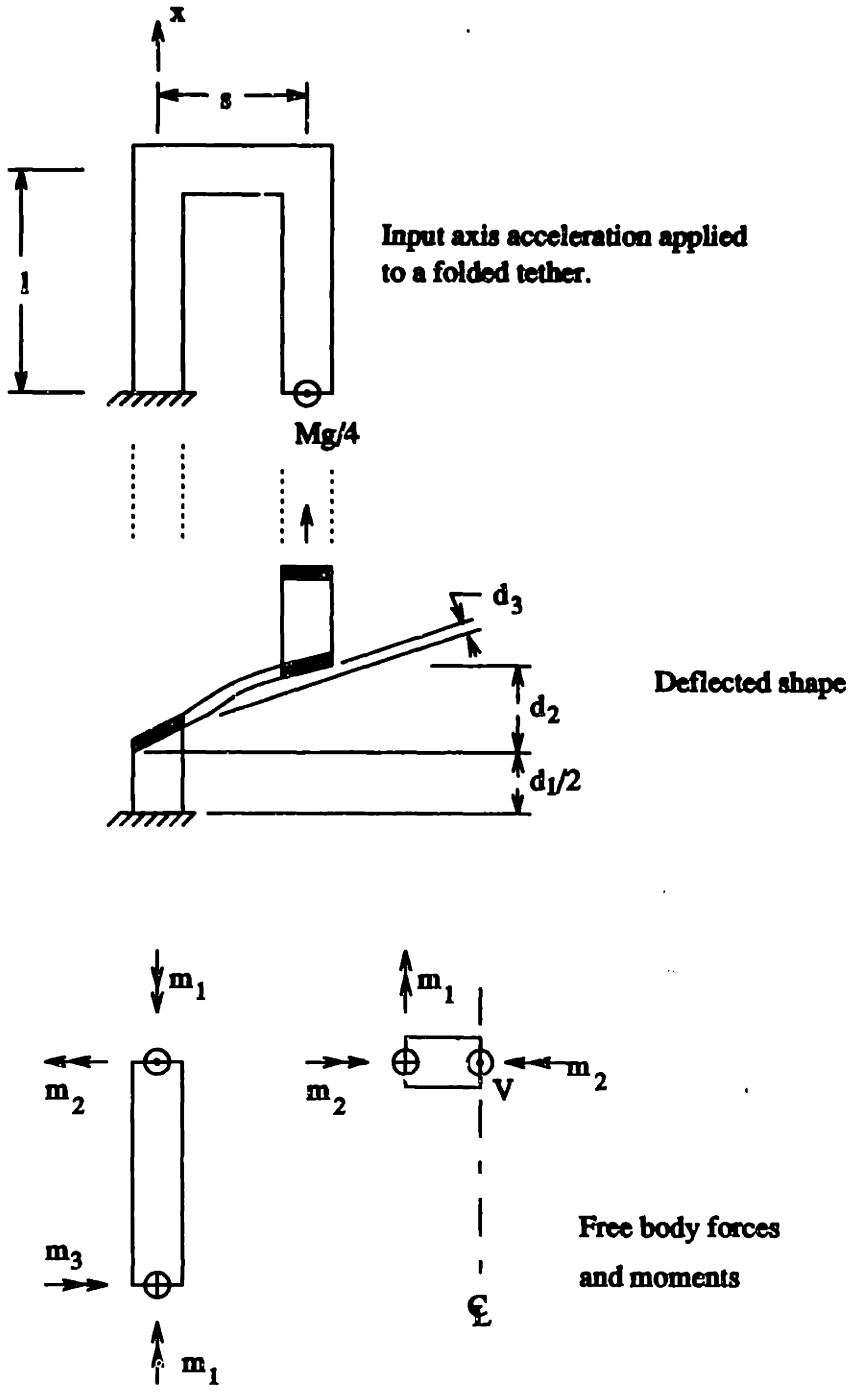

Figure B-5: Deflected shape and free body diagram of folded tether subjected to input axis acceleration.

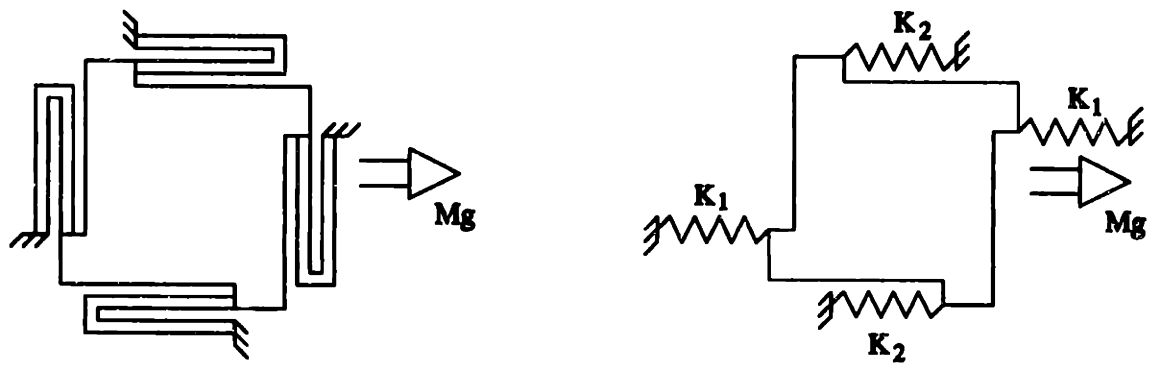

Figure B-6: Equivalent spring model of folded pinwheel design subjected to pendulous or hinge axis acceleration.

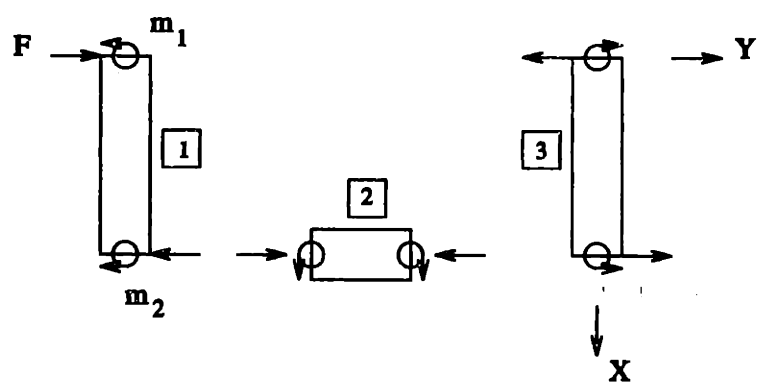

Figure B-7: Forces and moments acting on a folded tether subjected to pendulous or hinge axis acceleration.

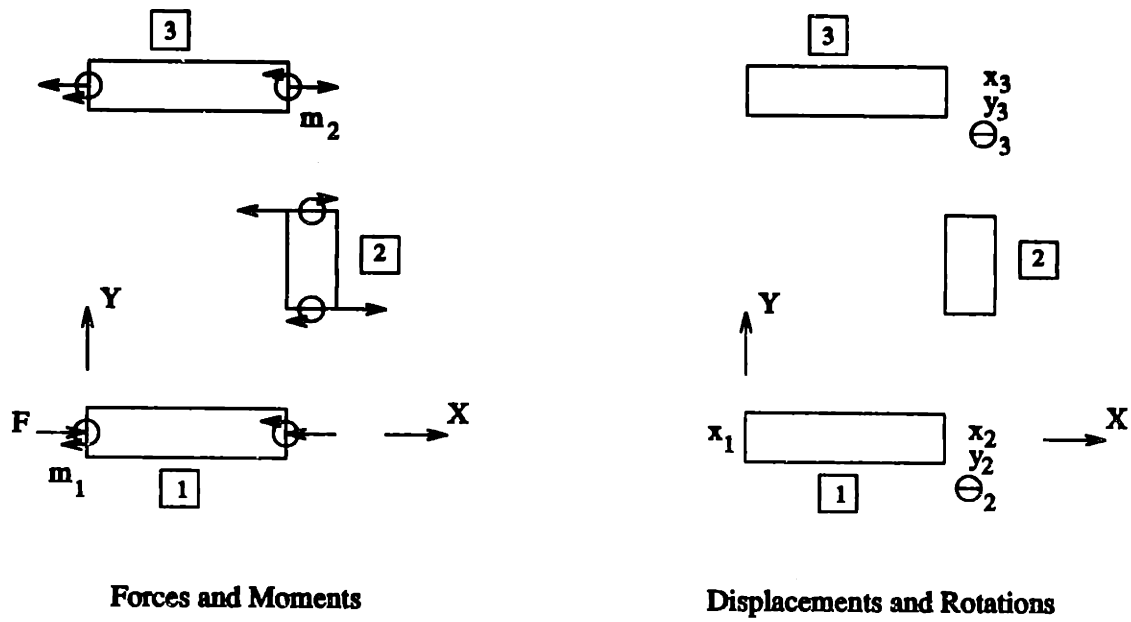

Figure B-8: Forces and moments acting on a folded tether subjected to pendulous or hinge axis acceleration.

Appendix C

Nonlinear Tether Mechanics

Here is the solution to the nonlinear response of the straight tether design. It is given as an iterative algorithm using Newton's Method. This solution gives the same answers as the finite element solution in Figure 2-10 for the straight tether design.

The mechanical model is shown in Figure C-1. We want to calculate Y, the total deflection, for a given force F. The nonlinear aspect of this problem is that the stiffness of the tether, and therefore the deflection Y, depends on the deflection Y. Therefore,

$$Y = \frac{F}{K(Y)} \tag{C.1}$$

Where K is the Y-dependent s-bending stiffness of the tether.

We need to know what the tether length S is for a given Y. First, from calculus, we have:

$$S = \int_{x=0}^{l} \sqrt{1 + \left(\frac{dy}{dx}\right)^2}\, dx \tag{C.2}$$

And from beam bending theory, ignoring axial loads, the shape (slope) of the tether is given by:

$$\frac{dy}{dx} = Y\frac{6x}{l^2}(1 - \frac{x}{l}) \tag{C.3}$$

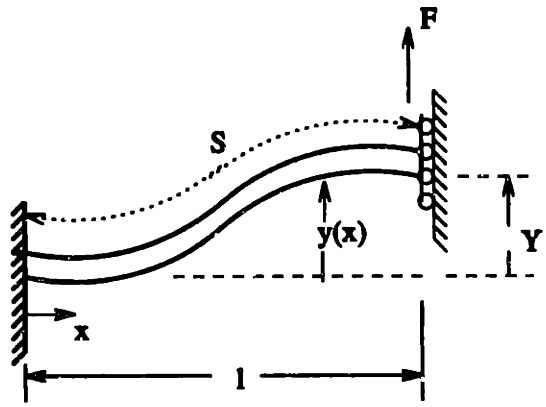

Figure C-1: Beam model for nonlinear analysis.

Combining these gives:

$$S(Y) = \int_{x=0}^{l} \sqrt{1 + \left[Y \frac{6x}{l^2} \left(1 - \frac{x}{l} \right) \right]^2} \, dx \tag{C.4}$$

We also need to know the tether's s-bending stiffness with an axial load $P(Y)$. This is given by [43]:

$$K(Y) = \frac{12EI}{l^3} + \frac{36}{30} \frac{P(Y)}{l} \tag{C.5}$$

And P(Y) is given by:

$$P(Y) = \frac{AE}{l} [S(Y) - l] \tag{C.6}$$

The solution algorithm is as follows:

1. Initialize: Y=0, ΔF=F, and calculate K from equation C.5 with P=0.
2. $\Delta Y = \frac{\Delta F}{K}$
3. $Y = Y + \Delta Y$
4. Calculate $S(Y)$ from equation C.4
5. Calculate $\Delta l = S - l$

6. Calculate $P(Y)$ from equation C.6

7. Calculate $K(Y)$ from equation C.5

8. Calculate $\Delta F = F - K \cdot Y$

9. Test if ΔF is less than some tolerance.

10. Loop to step 2, or exit if tolerance is met.

Appendix D

Reynolds' Equation for Gas Damping

D.1 Overview

Reynolds' equation provides a manageable formulation of the mechanics behind squeeze film gas damping. Section D.2 derives Reynolds' equation in cartesian coordinates, and Section D.3 derives it for cylindrical coordinates. Each of the derivation sections concludes with a summary of the assumptions that were made and the final differential equation. Solving Reynolds' equation gives the pressure distribution across the damping plates. Integrating the pressure over the entire plate area gives the damping force. And finally, the damping coefficient, B, is the total force divided by the relative velocity between the plates. Solutions for circular plates, and square plates, are given in Sections D.4 and D.5.

D.2 Derivation in Cartesian Coordinates

Figure D-1 and the following variable list, represent the squeeze film damping problem.

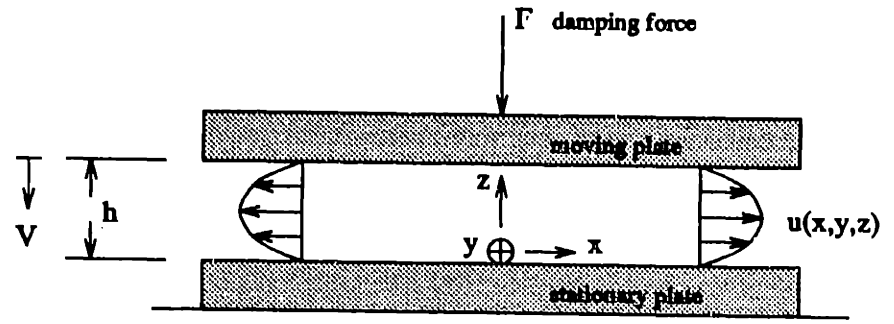

Figure D-1: Squeeze film damping.

x, y, z	=	cartesian coordinates
P	=	gas damping pressure
u, v, w	=	gas velocity in x, y, z directions
$\vec{U}$	=	vector notation for u, v, w
μ	=	viscosity
h	=	gap dimension between plates
V	=	relative velocity between plates, in z direction
F	=	gas damping force
ρ	=	gas density

We start with a fairly general form of the Navier-Stokes equations, and then simplify these to the 'creeping flow' form. This part follows exactly the derivation in [46].

Assuming Newtonian fluid, with constant viscosity, the Navier-Stokes equations are,

$$\rho \frac{\delta \vec{U}}{\delta t} + \rho \vec{U} \cdot \vec{\nabla} \vec{U} = -\vec{\nabla} P + \mu \vec{\nabla}^2 \vec{U} \tag{D.1}$$

Assuming incompressible flow, the continuity equation is,

$$\vec{\nabla} \cdot \vec{U} = 0 \tag{D.2}$$

The two terms on the left-hand side of Equation D.1 are the total time derivative of the velocity. The first term represents changes in the velocity with respect to time.

The second term is velocity changes with respect to spatial location. Both of these are inertia terms.

We get the creeping flow form of the Navier-Stokes equation by eliminating the inertia terms. This leaves only the viscous terms and the pressure. To justify this, we introduce the Strouhal number, Sr, and the Reynolds' number, Re.

$$Sr = \frac{VT}{L} \tag{D.3}$$

$$Re = \frac{\rho VL}{\mu} \tag{D.4}$$

$$\begin{aligned} V &= \text{characteristic velocity} \\ T &= \text{characteristic time} \\ L &= \text{characteristic length} \end{aligned}$$

Eliminating the $\frac{\delta \vec{U}}{\delta t}$ term is justified when,

$$\frac{Re}{Sr} \ll 1 \tag{D.5}$$

And the $\vec{U} \cdot \vec{\nabla}\vec{U}$ is elminated when,

$$Re \ll 1 \tag{D.6}$$

With these assumptions, the creeping flow equations and the continuity equation reduce to,

$$\frac{\delta P}{\delta x} = \mu \left(\frac{\delta^2 u}{\delta x^2} + \frac{\delta^2 u}{\delta y^2} + \frac{\delta^2 u}{\delta z^2} \right) \tag{D.7}$$

$$\frac{\delta P}{\delta y} = \mu \left(\frac{\delta^2 v}{\delta x^2} + \frac{\delta^2 v}{\delta y^2} + \frac{\delta^2 v}{\delta z^2} \right) \tag{D.8}$$

$$\frac{\delta P}{\delta z} = \mu \left(\frac{\delta^2 w}{\delta x^2} + \frac{\delta^2 w}{\delta y^2} + \frac{\delta^2 w}{\delta z^2} \right) \tag{D.9}$$

$$0 = \frac{\delta u}{\delta x} + \frac{\delta v}{\delta y} + \frac{\delta w}{\delta z} \tag{D.10}$$

Starting with the creeping flow equations, Reynolds then made additional assumptions about the velocity field in squeeze film dampers. This results in considerable simplification. We go from a set of partial differential equations, to a single partial differential equation with pressure as the unknown. Reynolds assumed w to be a linear function of z only, and independent of x and y. Also, he assumed that the variations of u and v are insignificant in the x and y directions, in comparison to the variations in the z direction. With these assumptions, Equations D.7 through D.10 become,

$$\frac{\delta P}{\delta x} = \mu \frac{\delta^2 u}{\delta z^2} \tag{D.11}$$

$$\frac{\delta P}{\delta y} = \mu \frac{\delta^2 v}{\delta z^2} \tag{D.12}$$

$$\frac{\delta P}{\delta z} = 0 \tag{D.13}$$

$$0 = \frac{\delta u}{\delta x} + \frac{\delta v}{\delta y} + \frac{dw}{dz} \tag{D.14}$$

For boundary conditions, we have $u = 0$ and $v = 0$ at the plate surfaces. This is the 'no-slip' boundary condition.Also, $w = -V$ at $z = h$, and $w = 0$ at $z = 0$. At the edges of the plates, P equals the external pressure, which we will take as zero.

Because of the assumption that w is a linear function of z only, we get Equation D.13, which says that the pressure is constant through the thickness of the film. Therefore, since the pressure is not a function of z, we can directly integrate Equations D.11 and D.12, from $z = 0$ to $z = h$, and use the no-slip boundary conditions, to determine the velocities u and v.

$$u = \frac{1}{2\mu} \frac{\delta P}{\delta x} z(z - h) \tag{D.15}$$

$$v = \frac{1}{2\mu} \frac{\delta P}{\delta y} z(z - h) \tag{D.16}$$

Next, substituting the derivative of Equation D.15 with respect to x, and the derivative of Equation D.16 with respect to y, into the continuity equation, D.14,

$$\frac{dw}{dz} = -\frac{1}{2\mu}(z-h)z\left(\frac{\delta^2 P}{\delta x^2} + \frac{\delta^2 P}{\delta y^2}\right) \tag{D.17}$$

Integrating both sides from $z = 0$ to h,

$$-V = -\frac{1}{2\mu}\left(\frac{h^3}{3} - \frac{h^3}{2}\right)\left(\frac{\delta^2 P}{\delta x^2} + \frac{\delta^2 P}{\delta y^2}\right) \tag{D.18}$$

This reduces to Reynolds' equation for gas damping,

$$\frac{\delta^2 P}{\delta x^2} + \frac{\delta^2 P}{\delta y^2} = \frac{-12\mu V}{h^3} \tag{D.19}$$

with the following assumptions,

- Newtonian fluid (fluid shear force $\propto$ viscosity times the velocity).
- Constant viscosity.
- $\frac{Re}{S_r} \ll 1$
- $Re \ll 1$
- Mach Number $\ll 1$ (incompressible flow).

The above get us through to the creeping flow form of the Navier-Stokes equations. To this we add,

- w, the fluid velocity in the z direction, is a linear function of z only, and independent of x and y. (Note that this is the same as assuming constant pressure across the film thickness.)
- u and v velocity variations are only significant in the z direction, and can be ignored in the x and y directions.
- $P = 0$ at the plate edge boundaries.

- $u = v = 0$ at the plate surface boundaries.
- $w = -V$ at the moving plate surface boundary.
- $w = 0$ at the stationary plate surface boundary.

D.3 Derivation in Cylindrical Coordinates

The derivation in cylindrical coordinates is nearly the same as for cartesian coordinates. Figure D-2 show squeeze film damping between two circular plates.

r = radial coordinate
z = axial coordinate
θ = angle coordinate
P = gas damping pressure
u, v, w = gas velocity in r, z, θ directions
$\vec{U}$ = vector notation for u, v, w
μ = viscosity
h = gap dimension between plates
V = relative velocity between plates, in z direction
F = gas damping force
ρ = gas density

We make the same assumptions as in Section D.2 to arrive at the creeping flow equations. Expressed in cylindrical coordinates, these are,

$$\frac{\delta P}{\delta r} = \mu \left[\frac{\delta}{\delta r} \left(\frac{1}{r} \frac{\delta}{\delta r} (ru) \right) + \frac{1}{r^2} \frac{\delta^2 u}{\delta \theta^2} - \frac{2}{r^2} \frac{\delta w}{\delta \theta} + \frac{\delta^2 u}{\delta z^2} \right] \tag{D.20}$$

$$\frac{\delta P}{\delta z} = \mu \left[\frac{1}{r} \frac{\delta}{\delta r} (r \frac{\delta v}{\delta r}) + \frac{1}{r^2} \frac{\delta^2 v}{\delta \theta^2} + \frac{\delta^2 v}{\delta z^2} \right] \tag{D.21}$$

$$\frac{\delta P}{\delta \theta} = r\mu \left[\frac{\delta}{\delta r} \left(\frac{1}{r} \frac{\delta}{\delta r} (rw) \right) + \frac{1}{r^2} \frac{\delta^2 w}{\delta \theta^2} + \frac{2}{r^2} \frac{\delta u}{\delta \theta} + \frac{\delta^2 w}{\delta z^2} \right] \tag{D.22}$$

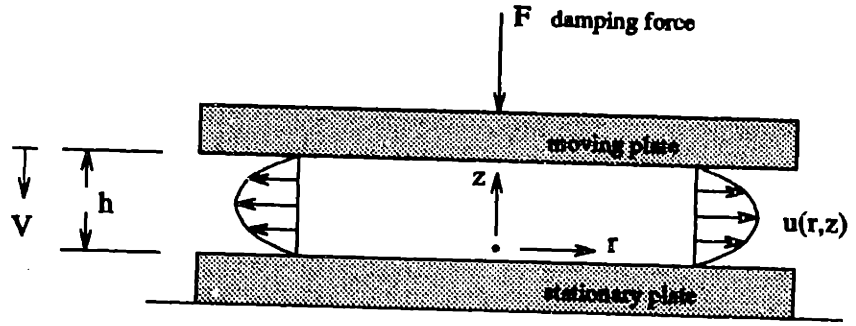

Figure D-2: Squeeze film damping between two circular plates.

$$0 = \frac{1}{r}\frac{\delta}{\delta r}(ru) + \frac{\delta v}{\delta z} + \frac{1}{r}\frac{\delta w}{\delta \theta} \tag{D.23}$$

Next, we make the assumptions regarding the flow field. Assuming axial symmetry, then the angular flow velocity, w, is zero, and all $\frac{\delta}{\delta\theta}$ terms equal zero. We also assume that the z-directed velocity, v, is a linear function of z only, just as we did for the cartesian derivation. This last assumption implies that the pressure is constant through the film thickness. With these assumptions, Equations D.20 through D.23 become,

$$\frac{dP}{dr} = \mu\frac{\delta^2 u}{\delta z^2} \tag{D.24}$$

$$\frac{\delta P}{\delta z} = 0 \tag{D.25}$$

$$0 = \frac{1}{r}\frac{\delta}{\delta r}(ru) + \frac{dv}{dz} \tag{D.26}$$

For boundary conditions, we have $u = 0$ at both of the plate surfaces, $w = -V$ at the moving plate surface, and $w = 0$ at the stationary plate surface. At the edges of the plates, P equals the external pressure, which we take to be zero.

Now integrate Equation D.24 with respect to z, realizing that P is not a function

of z. This gives the u velocity profile.

$$u = \frac{1}{2\mu}\frac{dP}{dr}(z-h)z \tag{D.27}$$

We assumed that v is a function of z only, with boundary conditions of $v = -V$ at $z = h$, and $v = 0$ at $z = 0$. Therefore,

$$v = \frac{-V}{h}z \tag{D.28}$$

Substituting Equation D.27, and the derivative of Equation D.28 with respect to z, into the continuity equation, D.26,

$$0 = \frac{1}{r}\frac{d}{dr}\left[\frac{r}{2\mu}\frac{dP}{dr}(z-h)z\right] - \frac{V}{h} \tag{D.29}$$

Integrating from $z = 0$ to h,

$$0 = \frac{-h^3}{12\mu}\frac{1}{r}\frac{d}{dr}\left(r\frac{dP}{dr}\right) - V \tag{D.30}$$

This gives Reynolds' equation for squeeze film damping, in cylindrical coordinates,

$$\frac{1}{r}\frac{d}{dr}\left(r\frac{dP}{dr}\right) = \frac{-12\mu V}{h^3} \tag{D.31}$$

with the following assumptions,

- Newtonian fluid (fluid shear force $\propto$ viscosity times the velocity).
- Constant viscosity.
- $\frac{Re}{Sr} \ll 1$
- $Re \ll 1$
- Mach Number $\ll 1$ (incompressible flow).

The above get us through to the creeping flow form of the Navier-Stokes equations. To this we add,

- Axiai symmetry, so that the angular flow velocity, w, is zero, and all $\frac{\delta}{\delta\theta}$ terms equal zero.
- v, the fluid velocity in the z direction, is a linear function of z only, and independent of r and θ.
- $P = 0$ at the plate edge boundaries.
- $u = 0$ at the plate surface boundaries.
- $v = -V$ at the moving plate surface boundary.
- $v = 0$ at the stationary plate surface boundary.

D.4 Solution for Circular Plates

Equation D.31 is an ordinary linear differential equation. We get the solution for the pressure by separating variables and integrating twice, and then applying the boundary condition that $P = 0$ at $r = R$.

$$\int d\left(r\frac{dP}{dr}\right) = \int \frac{-12\mu V}{h^3} r dr$$

$$r\frac{dP}{dr} = \frac{-12\mu V}{h^3}\frac{r^2}{2} + C_1$$

$$\int dP = \int \frac{-12\mu V}{h^3}\left(\frac{r}{2} + \frac{C_1}{r}\right) dr$$

$$P(r) = \frac{-12\mu V}{h^3}\left(\frac{r^2}{4} + C_1 \ln r + C_2\right)$$

We know that C_1 must be zero because the pressure is defined at r=0, but $\ln r$ is not. By using the boundary condition, $P = 0$ at $r = R$, we find that $C_2 = -R^2$. Therefore, the pressure solution is,

$$P(r) = \frac{3\mu V}{h^3}\left(R^2 - r^2\right) \tag{D.32}$$

Next, integrate the pressure over the plate area to find the total damping force, F_d.

$$\int_{area} P(r)dA = \int_{r=0}^{R} \frac{3\mu V}{h^3}\left(R^2 - r^2\right) 2\pi r dr \tag{D.33}$$

$$F_d = \frac{3\pi\mu V R^4}{2h^3} \tag{D.34}$$

Finally, the damping coefficient, B, is defined as the damping force over the velocity.

$$B = \frac{F_d}{V} = \frac{3\pi\mu R^4}{2h^3} \tag{D.35}$$

D.5 Solution for Square Plates

This solution is taken from [47].

$$B = \frac{-\mu L^4}{h^3}\left[1 - \frac{192}{\pi^5}\sum_{n=1}^{n=\infty}\frac{tanh\frac{n\pi}{2}}{n^5}\right] \quad = .4217\frac{\mu L^4}{h^3} \tag{D.36}$$

L = plate length

h = gap dimension

μ = gas viscosity

Appendix E

Process Traveler

PROCESS TRAVELER Revision 2

6/4/92

3/24/92 new

uACCELEROMETER FAB PROCESS

LOT # _____

LOT OWNER: Mitch Novack

10

STEP #	STEP DESCRIPTION	STATUS
------	----------	------

HANDLE WAFER:

Starting Material: n–type <100> .5–2 ohm–cm double–side polish

[ICL]

1 RCA Number wafers _____ 20

Opset start _____

Opset finish _____

2	Phosphorous dep/drive–in dphos8.set (925 degC POCL3 87 min)	Number wafers _____ Opset start _____ Opset finish _____
3	Wet etch phosphorous glass BOE	Number wafers _____ Opset start _____ Opset finish _____
4	Measure Sheet Rho (5.7 ohms/sq)	Number wafers _____ Opset start _____ Opset finish _____
5	Thermal Oxide 1.4 um (rca, recipe 245, 9hrs:38min)	Number wafers _____ Opset start _____ Opset finish _____
6	Nanospec Oxide Thickness	Number wafers _____ Opset start _____ Opset finish _____
7	Pattern Oxide 1.35 um pos. resist rcp: spin wash 200 degC, 45 min dehydrate 3.5 sec deposit at 10 rpm 2.0 sec spread at 10 rpm 45 sec spin at 3000 rpm 90 degC, 30 min prebake 2.7 sec exposure 40 sec develop 120 degC hardbake	Number wafers _____ Opset start _____ Opset finish _____
8	Dry Etch Oxide etcher–2 rcp#20 to manual endpoint etcher–1 rcp#12 17 sec, no overetch	Number wafers _____ Opset start _____ Opset finish _____

9	Strip resist 3:1 H2SO4:H2O2	Number wafers _____ Opset start _____ Opset finish _____	60
10	Inspect for resist under mercury lamp	Number wafers _____ Opset start _____ Opset finish _____	

DEVICE WAFER: 70

starting material: p–prime, 10–20 ohm–cm, <100>

11	RCA	Number wafers _____ Opset start _____ Opset finish _____	
12	Solid source boron dope Recipe #380, tube B3 (8 hrs, 1125 degC)	Number wafers _____ Opset start _____ Opset finish _____	80
13	Strip boron glass in BOE verify de–wetts	Number wafers _____ Opset start _____ Opset finish _____	
14	Measure sheet resistivity less than 1 ohm/square	Number wafers _____ Opset start _____ Opset finish _____	

DEVICE WAFER and HANDLE WAFER: 90

[TRL]

15	Bond Wafer Pairs rca, contact, anneal 1100degC, 70min, N2	Number wafers _____ Opset start _____ Opset finish _____	

[RGL]

16 Bulk Etch Device Wafer
20% KOH,60 degC,18hrs
(27 um/hr etch rate)

Number wafers _____
Opset start _____
Opset finish _____

17 Finish (stop) Etch
60% CsOH, 60degC
(8 um/hr etch rate)

Number wafers _____
Opset start _____
Opset finish _____

18 BOE strip oxide
10 min

Number wafers _____
Opset start _____
Opset finish _____

[RGL/TRL]

19 Post KOH Clean

Number wafers _____
Opset start _____
Opset finish _____

(5th floor):

Rinse vigorously in DI Water. 10min.
N2–Blow dry.

(TRL) Acid–hood:

Piranha etch (3:1 H2SO4:H2O2). 5 minutes.
Rinse 3 times in Dump–to–Resistivity tank.

(TRL) Acid–hood:

–Dip in 50:1HF for 10 seconds.
(make sure wafers dewet; this removes 50A of contaminated oxide).
–Rinse 3 times in Dump–to–Resistivity tank.
–Photo–wet stn: Spin–Dry cycle. Monitor resistivity to better than 9.0M–Ohm–cm.

(TRL) RCA station:

−RCA clean

−monitor resistivity at the spin−dry cycle

with a 160sec. rinse.

[ICL]

20	Measure sheet resistivity	Number wafers _____	140
	should be <1ohm/square	Opset start _____	
		Opset finish _____	

[TRL]

21	Pattern for liftoff prcss (device side)	Number wafers _____	
	HMDS	Opset start _____	
	1.4 um AZ5214E (4KRPM, 30 sec)	Opset finish _____	
	90 degC prebake, 30min		
	3 sec exposure, 11 mwatts/cm2		150
	120 degC, 90 sec, directly on hot plate		
	90 sec flood exposure		
	80 sec develop, AZ422MIF		

22	E−beam dep	Number wafers _____	
	100 A Cr	Opset start _____	
	5000 A Pt	Opset finish _____	

23	Wet strip (liftoff)	Number wafers _____	
	10 sec in 500 ml acetone	Opset start _____	160
	10 min in 500 ml acetone	Opset finish _____	
	10 min in 500 ml methanol		

24	Spin Resist and Pattern Trench Etch	Number wafers _____	
	1.6um thick:	Opset start _____	
	200 degC, 30 min dehydrate	Opset finish _____	
	6 sec deposit at 70 rpm		

4 sec spread at 200 rpm

40 sec spin at 2000 rpm

4.6 sec exposure

60 sec develop

[ICL]

25 Plasma Etch 5um P+ layer

etcher−1 rcp#15, 3minutes

Si:PR selectivity = 3.9 minimum

= 5.0 average

Number wafers _____

Opset start _____

Opset finish _____

26 Ash resist

Number wafers _____

Opset start _____

Opset finish _____

[TRL]

27 E−beam dep backside of wafer

100 A Cr

5000 A Pt

Number wafers _____

Opset start _____

Opset finish _____

28 Sinter metal

500 degC, 30 min, N2

Number wafers _____

Opset start _____

Opset finish _____

29 Scribe wafer into die

Number wafers _____

Opset start _____

Opset finish _____

30 HF release devices

Number wafers _____

Opset start _____

Opset finish _____

Bibliography

[1] Frank Goodenough. Airbags boom when ic accelerometer sees 50g. *Electronic Design*, 8 August 1991.

[2] Roylance and Angell. A batch-fabricated silicon accelerometer. *IEEE Transactions on Electron Devices*, ED-26 no.12, December 1979.

[3] Frobenius et al. Microminiature ganged threshold accelerometers compatible with integrated circuit technology. *IEEE Transactions on Electron Devices*, ED-19 no. 1, January 1972.

[4] Sherman, Tsang, Core, and Quinn. A low cost monolithic accelerometer. In *proceedings, Symposium on VLSI Circuits*, pages 34–35. IEEE, 1992.

[5] Ristic, Gutteridge, Dunn, Mietus, and Bennett. Surface micromachined polysilicon accelerometer. In *proceedings, Solid State Sensors and Actuators Workshop, Hilton Head Island*, pages 118–121. IEEE, 1992.

[6] Barth, Pourahmadi, Mayer, Poydock, and Petersen. A monolithic silicon accelerometer with integral air damping and overrange protection. In *proceedings, Solid State Sensors and Actuators Workshop, Hilton Head Island*, pages 35–38. IEEE, 1988.

[7] Pourahmadi, Christel, and Petersen. Silicon accelerometer with new thermal self-test mechanism. In *proceedings, Solid State Sensors and Actuators Workshop, Hilton Head Island*, pages 122–125. IEEE, 1992.

[8] Bruin, Allen, and Terry. Second-order effects in self-testable accelerometers. In *proceedings, Solid State Sensors and Actuators Workshop, Hilton Head Island*, pages 149–152. IEEE, 1990.

[9] Allen, Terry, and Bruin. Self-testable accelerometer systems. In *proceedings, Micro Electro Mechanical Systems*, pages 113–115. IEEE, 1989.

[10] Allen, Terry, and Bruin. Accelerometer systems with built-in testing. In *proceedings, International Conference Solid State Sensors and Actuators*, pages 381–386. IEEE, 1989.

[11] Stephen Terry. A miniature silicon accelerometer with built-in damping. In *proceedings, Solid State Sensors and Actuators Workshop, Hilton Head Island*, pages 114–116. IEEE, 1988.

[12] James T. Suminto. A simple, high performance piezoresistive accelerometer. In *proceedings, International Conference Solid State Sensors and Actuators*, pages 104–107. IEEE, 1991.

[13] Link, Suminto, and Young. A rugged, high-performance piezoresistive accelerometer. *Sensors*, October 1991.

[14] Kloeck et al. Motion investigation of electrostatic servo-accelerometers by means of transparent ito fixed electrodes. In *proceedings, International Conference Solid State Sensors and Actuators*, pages 108–111. IEEE, 1991.

[15] Suzuki et al. Semiconductor capacitance-type accelerometer with pwm electrostatic servo technique. In *proceedings, International Conference Solid State Sensors and Actuators*, pages 316–319. IEEE, 1989.

[16] Tsuchitani et al. Study of the behavior of a pwm electrostatic servo accelerometer. In *proceedings, The 10th Sensor Symposium, Tokyo*, pages 45–48. Institute of Electrical Engineers of Japan, 1991.

[17] John C. Cole. A new sense element technology for accelerometer subsystems. In *proceedings, International Conference Solid State Sensors and Actuators*, pages 93–96. IEEE, 1991.

[18] Rudolf, Jornod, Bergqvist, and Leuthold. Precision accelerometers with ug resolution. In *proceedings, International Conference Solid State Sensors and Actuators*, pages 297–302. IEEE, 1989.

[19] Henrion, Disanza, Ip, Terry, and Jerman. Wide dynamic range direct digital accelerometer. In *proceedings, Solid State Sensors and Actuators Workshop, Hilton Head Island*, pages 153–157. IEEE, 1990.

[20] Peeters, Vergote, Puers, and Sansen. A highly symmetrical capacitive microaccelerometer with single degree-of-freedom response. In *proceedings, International Conference Solid State Sensors and Actuators*, pages 97–100. IEEE, 1991.

[21] Seidel et al. Capacitive silicon accelerometer with highly symmetrical design. In *proceedings, International Conference Solid State Sensors and Actuators*, pages 312–315. IEEE, 1989.

[22] Kourepenis, Petrovich, and Weinberg. Low cost quartz resonant accelerometer for aircraft inertial navigation. In *proceedings, International Conference Solid State Sensors and Actuators*, pages 551–553. IEEE, 1991.

[23] Boxenhorn and Greiff. Monolithic silicon accelerometer. In *proceedings, International Conference Solid State Sensors and Actuators*, pages 273–277. IEEE, 1989.

[24] Yamada and Tanigawa. A novel silicon accelerometer with a surrounding mass structure. In *proceedings, International Conference Solid State Sensors and Actuators*, pages 308–311. IEEE, 1989.

[25] Satchell and Greenwood. A thermally-excited silicon accelerometer. *Sensors and Actuators*, pages 241–245, May 1989.

[26] Chang, Putty, Hicks, Li, and Howe. Resonant-bridge two-axis microaccelerometer. In *proceedings, International Conference Solid State Sensors and Actuators*, pages 342–345. IEEE, 1989.

[27] Yun, Howe, and Gray. Surface micromachined, digitally force-balanced accelerometer with integrated cmos detection circuitry. In *proceedings, Solid State Sensors and Actuators Workshop, Hilton Head Island*, pages 126–131. IEEE, 1992.

[28] Ura and Esashi. Differential capacitance silicon accelerometer. In *proceedings, The 10th Sensor Symposium, Tokyo*, pages 41–44. Institute of Electrical Engineers of Japan, 1991.

[29] V.H. Aske. An integrated silicon accelerometer. *Scientific Honeyweller*, Fall 1987.

[30] PATRAN. A commercially available finite element modeler and post-processor, available from PDA Engineering.

[31] ABAQUS. A commercially available finite element software package, available from Hibbitt, Karlsson, and Sorensen, Inc.

[32] Kurt E. Petersen. Silicon as a mechanical material. In *Proceedings of the IEEE*, pages 420–457. IEEE, 1982.

[33] Maseeh and Senturia. Plastic deformation of highly doped silicon. *Sensor and Acuator*, A21-23:861–865, 1990.

[34] S. Wolf and R.N. Tauber. *Silicon Processing for the VLSI Era, Volume I.* Lattice Press, 1986.

[35] Bathe. *Finite Element Procedures in Engineering.* Prentice-Hall, 1982.

[36] Shearer, Murphy, and Richardson. *Introduction to System Dynamics.* Addison-Wesley, 1971.

[37] James B. Starr. Squeeze film damping in solid state accelerometers. In *proceedings, Solid State Sensors and Actuators Workshop*, pages 44–47. IEEE, 1990.

[38] Errol B. Arkilic and Kenneth S. Breuer. Gaseous flow in small channels. submitted to Physics of Fluids, A, 1992.

[39] H. Seidel, L. Csepregi, A. Heuberger, and H. Baugartel. Anisotropic etching of crystalline silicon in alkaline solutions. *Journal of the Electrochemical Society*, 137(11), November 1990.

[40] Aleksa D. Nikolich. Microfabricated resonant strain gauges. Master's thesis, Massachusettes Institute of Technology, September 1991.

[41] Mark Paul Lubratt. A voltage-tunable microfabricated accelerometer. Master's thesis, Massachusettes Institute of Technology, October 1991.

[42] George E. Dieter. *Mechanical Metallurgy.* McGraw-Hill, 1976.

[43] William Jr. Weaver and Paul R. Johnston. *Finite Elements for Structural Engineers.* Prentice-Hall, Inc, 1984.

[44] Rudolf A. Buser. *Theoretical and Experimental Investigations on Silicon Single Crystal Resonant Structures.* PhD thesis, University of Neuchatel, Switzerland.

[45] J.J. Wortman and R.A. Evans. Young's modulus, shear modulus, and poisson's ratio in silicon and germanium. *Journal of Applied Physics*, 36(1), January 1965.

[46] Morton M. Denn. *Design of Fluid Bearings.* Macmillan.

[47] Archibald. Load capacity and time relations for squeeze films. *Transactions of the American Society of Mechanical Engineers*, 78, 1956.